

Diss. ETH No. 13449

Physical Ecosystem Determinants in High Mountain Lakes The Jöri Lakes, Switzerland

A dissertation submitted to the
SWISS FEDERAL INSTITUTE OF TECHNOLOGY (ETH)
ZÜRICH

for the degree of
DOCTOR OF NATURAL SCIENCES

presented by
MATTHIAS GABATHULER
Dipl. Natw. ETH
born 23 January 1971
citizen of Wartau (SG)

accepted on the recommendation of
Prof. Dr. A. Waldvogel, examiner
Dr. K. Hanselmann, co-examiner

1999

Contents

| | |
|--------------------------------------------------------------------|------------------|
| Contents | i |
| Abstract | v |
| Kurzfassung | vii |
| <i>1 Introduction</i> | <i>1</i> |
| <i>2 Morphology of the Jöri catchment and its lakes</i> | <i>5</i> |
| 2.1 Introduction | 5 |
| 2.2 Catchment description | 5 |
| 2.3 Description of the largest lakes and their surroundings | 8 |
| 2.3.1 Lake III | 9 |
| 2.3.2 Other lakes in the Jöri catchment | 11 |
| <i>3 Meteorological variability</i> | <i>13</i> |
| 3.1 Introduction | 13 |
| 3.2 Jöri automatic weather station | 13 |
| 3.3 Measurements at AWSs outside the Jöri catchment | 14 |
| 3.4 Air temperature | 15 |
| 3.4.1 Measurement errors and correction | 15 |
| 3.4.2 Regional heterogeneity of air temperature | 18 |
| 3.4.3 Conclusions | 22 |
| 3.5 Humidity | 22 |
| 3.5.1 Measurement errors | 22 |
| 3.5.2 Regional heterogeneity of humidity | 23 |
| 3.5.3 Conclusions | 24 |
| 3.6 Wind speed and direction | 24 |
| 3.6.1 Measurement errors and problems | 25 |
| 3.6.2 Regional heterogeneity of wind speed and direction | 25 |
| 3.6.3 Conclusions | 29 |
| 3.7 Global Radiation | 29 |
| 3.7.1 Measurement errors | 29 |
| 3.7.2 Regional heterogeneity of global radiation | 30 |
| 3.7.3 Calculation of global radiation | 32 |

| | |
|---------------------------------------------------------------------------|------------------|
| 3.7.4 Conclusions | 36 |
| 3.8 Incoming longwave radiation | 36 |
| 3.8.1 Measurement errors and problems | 37 |
| 3.8.2 An improved method for calculating incoming longwave radiation | 38 |
| 3.8.3 Results | 40 |
| 3.8.4 Limitations of the new model | 43 |
| 3.9 Precipitation | 43 |
| 3.9.1 Measurement errors and problems | 43 |
| 3.9.2 Comparison of precipitation data from different AWSs | 44 |
| 3.9.3 Conclusions | 46 |
| 3.10 General climatology of the Jöri AWS | 46 |
| <i>4 Effects of suspended erosion particles in lakes</i> | <i>48</i> |
| 4.1 Introduction | 48 |
| 4.2 The Jöri glacier | 48 |
| 4.2.1 Glacier melt | 49 |
| 4.2.2 Flow path of the glacier meltwater | 51 |
| 4.3 Turbidity, albedo and color of Lake III | 51 |
| 4.3.1 Measuring turbidity and albedo in Lake III | 51 |
| 4.3.2 Color of glacial lakes | 53 |
| 4.3.3 Attenuation coefficients | 54 |
| 4.3.4 Albedo values | 56 |
| 4.3.5 Euphotic zone | 58 |
| 4.4 Interpretation of suspended particle concentration variability | 59 |
| 4.4.1 Suspended erosion particles in other lakes | 60 |
| 4.5 Conclusions | 61 |
| <i>5 Energy budget of a high mountain lake</i> | <i>62</i> |
| 5.1 Introduction | 62 |
| 5.2 Energy budget components | 62 |
| 5.2.1 Shortwave radiation | 63 |
| 5.2.2 Longwave radiation | 63 |
| 5.2.3 Latent and sensible heat flux | 64 |
| 5.2.4 Precipitation heat flux | 66 |
| 5.2.5 Throughflow heat flux | 67 |
| 5.2.6 Sediment heat flux | 68 |

| | |
|-------------------------------------------------------------------------------|------------|
| 5.3 Heat content and heat flux calculations for Lake III | 68 |
| 5.3.1 Thermistor data from Lake III | 69 |
| 5.3.2 Lake III heat content | 70 |
| 5.3.3 Lake III heat flux calculation | 72 |
| 5.3.4 Possible errors in heat flux calculations | 77 |
| 5.3.5 Estimating the magnitude of neglected heat fluxes | 78 |
| 5.4 Temperature profile analysis of Jöri Lake III | 81 |
| 5.4.1 Introduction | 81 |
| 5.4.2 Case studies | 82 |
| 5.4.3 Comparison of stratification between years | 84 |
| 5.4.4 Winter lake temperature | 86 |
| 5.4.5 Effects of throughflow during the summer | 88 |
| 5.5 Heterogeneity of lake surface water temperature | 89 |
| 5.5.1 Introduction | 89 |
| 5.5.2 Measurement methods | 90 |
| 5.5.3 Lake surface water temperature data and interpretation | 90 |
| 5.5.4 A model for lake surface water temperature calculations | 97 |
| 5.5.5 Application of the model | 98 |
| 5.5.6 Results of the lake surface water temperature calculations | 100 |
| 5.6 Conclusions on heterogeneous water temperature | 102 |
| 6 Ice cover processes | 104 |
| 6.1 Introduction | 104 |
| 6.2 Ice build-up and development | 104 |
| 6.2.1 Observations of ice cover on the Jöri Lakes | 105 |
| 6.2.2 Ice-models and their limitations | 107 |
| 6.3 Ice decay | 110 |
| 6.3.1 Observation and interpretation of ice cover decay in the Jöri catchment | 111 |
| 6.3.2 Calculation of the break-up date | 114 |
| 6.4 Conclusions | 118 |
| 7 Conclusions and outlook | 120 |
| 7.1 Conclusions | 120 |
| 7.2 Outlook | 122 |
| Appendix | 124 |

| | |
|-----------------------------------------|------------|
| Technical specifications of instruments | 124 |
| Data from other institutes | 125 |
| Meteorological data from the Jöri AWS | 126 |
| Abbreviations | 132 |
| <i>Bibliography</i> | <i>134</i> |
| <i>Acknowledgements</i> | <i>140</i> |
| <i>Curriculum Vitae</i> | <i>142</i> |

Abstract

From 1996 through 1999, physical, chemical and biological processes in several mountain lakes in eastern Switzerland (the Jöri Lakes) were investigated. The emphasis was on the physical ecosystem determinants in mountain lakes and their catchment.

Meteorological data recorded at several different automatic weather stations in and around the Jöri catchment were compared. This comparison showed that air temperature, relative humidity and global radiation can be approximated well at locations for which no meteorological data were available. For wind speed and precipitation, however, such approximations are much more difficult. Since precipitation and wind speed are of importance for the calculation of the energy budget of a mountain lake, it is necessary to measure these variables at the lake in question directly. Precipitation is usually considered to be insignificant for lake energy budget calculations, but it was proven in this study that this is not the case for mountain lakes.

Longwave radiation measurements or estimates thereof are needed for lake modeling and for a wide range of other ecological and geophysical research applications. For this reason, a model was developed to predict longwave radiation based on air temperature, relative humidity and global radiation. This new model described the data set better than existing models based on cloud cover instead of global radiation.

Even if the most common meteorological variables are measured at a lake, there are still errors in the calculation of the energy budget. Firstly, sediment and throughflow heat fluxes are not dependent on meteorological variables and would have to be measured separately in order to calculate their magnitude and then contribution to the energy budget. These heat fluxes were not measured in Jöri Lake III, and it was shown in this study that the errors in the energy flux calculations were mostly due to this omission. Secondly, the horizontal distribution of meteorological variables on a lake is not homogeneous; wind speeds tend to be smaller near the shore and global radiation is shaded by horizon obstruction at times.

Despite these limitations, surface water temperature calculations proved to be accurate in several lakes. The lakes where the calculations were most accurate were shallow lakes with little cold water inflow and lakes with high wind forcing. Using a model which incorporated equilibrium temperature, the surface water temperatures in these lakes could be calculated without the use of meteorological data recorded directly at the sites. This offers new perspectives for the study of remote mountain lakes, where water temperatures can possibly be calculated without measurements having to be made directly at the lakes. The basis for these calculations was laid when finding that the heterogeneity of water temperatures in the different lakes within a small catchment can

be attributed to catchment characteristics, lake depth, turbidity and wind speed. Other meteorological and morphological factors are similar for all lakes in a small catchment and have only little effect on the heterogeneity of lake water temperature.

The lakes where errors in calculated surface water temperature were largest included those with glacier meltwater inflow. These lakes were of a lighter color due to the high particle concentrations. Particle concentrations represent relevant living conditions for organisms in lakes since they absorb and scatter global radiation. In lakes with particle-rich glacier meltwater, the euphotic depth can be at 4 m and below, whereas in clear lakes the euphotic depth is frequently greater than the maximum depth of the lake. Albedo was found to correlate well with the attenuation coefficient in Lake III. In lakes with suspended erosion particles the albedo can exceed 0.2. Neglecting such high values would lead to large errors in energy budget calculations.

Most important for the attenuation of global radiation is the winter ice cover, which is usually present for about 9 months of the year at the Jöri Lakes. Since a lake can become ice-covered partially or even completely within a few hours, the usefulness of 0- and 1-dimensional models to predict the freeze-up date of mountain lakes is limited. A degree-day model for ice-decay, adjusted for maximum seasonal snow height, was developed and calibrated for Jöri Lake III. Previous models assumed equal ice thickness for all years, but data from the Jöri lakes implied that this is not true for high mountain lakes. The new model yielded good results with a standard deviation of only 2 days. Data from the past 40 years indicate a tendency towards earlier break-up dates since 1988. This was attributed to higher air temperatures in the months May and June as derived from long-term measurements at Weissfluhjoch AWS. The cause of this warming trend is not clear.

Kurzfassung

Von 1996 bis 1999 wurden physikalische, chemische und biologische Prozesse in Bergseen von Graubünden (die Jöriseen) intensiv untersucht. Der Schwerpunkt der Untersuchungen lag bei den physikalischen Ökosystemdeterminanten in diesen Bergseen und in deren Einzugsgebiet.

Vergleiche zwischen meteorologischen Messwerten von mehreren Wetterstationen im Einzugsgebiet der Jöriseen und in deren Umgebung zeigten, dass Lufttemperatur, relative Feuchtigkeit und Globalstrahlung gut für Punkte angenähert werden können, an welchen diese Messungen nicht durchgeführt wurden. Für Windgeschwindigkeit und Niederschlag sind Annäherungen für Punkte ohne Messwerte äusserst schwierig. Da der Niederschlag und insbesondere die Windgeschwindigkeit wichtig für die Berechnung des Energiebudgets von Bergseen sind, ist es eine Voraussetzung, dass diese Werte direkt bei einem untersuchten See gemessen werden. In Berechnungen des Energiebudgets wird Niederschlag normalerweise nicht berücksichtigt. In dieser Untersuchung wurde aber gezeigt, dass Niederschlag in Bergseen einen nicht zu vernachlässigenden Einfluss hat.

Messungen oder Abschätzungen von langwelliger Strahlung sind nicht nur für Seemodelle wichtig, sondern für eine grosse Anzahl von Forschungsrichtungen. Aus diesem Grund wurde ein Modell zur Berechnung von langwelliger Strahlung auf Grund von Lufttemperatur, relativer Luftfeuchtigkeit und Globalstrahlung entwickelt. Das neue Modell liefert gleich gute oder bessere Resultate als bisherige Modelle für den vorhandenen Datensatz.

Die Berechnungen des Energiebudgets zeigten, dass auch dann noch relativ grosse Fehler entstehen, wenn die meteorologischen Messwerte unmittelbar beim untersuchten See gemessen werden. Erstens sind Energieflüsse von Durchfluss und Sediment nicht abhängig von meteorologischen Grössen. Um ihre Grösse zu bestimmen, müssen sie separat gemessen werden. Bei Jörisee III wurden diese Wärme flüsse nicht gemessen und es zeigte sich in dieser Untersuchung, dass die Fehler der Energieflussberechnungen zu einem grossen Teil durch diese vernachlässigten Wärme flüsse hervorgerufen wurden. Zweitens sind einige meteorologische Grössen nicht homogen über den See verteilt. Die Windgeschwindigkeit ist in der Nähe des Ufers eher tiefer und hohe Berge können den See teilweise abschatten.

Trotz diesen Einschränkungen kann die Oberflächentemperatur verschiedener Seen ziemlich genau berechnet werden. Die Genauigkeit ist am grössten bei flachen Seen, welche einen geringen Zufluss an kaltem Schmelzwasser haben oder bei Seen, bei welchen die Windgeschwindigkeit überdurchschnittlich hoch ist. Mit Hilfe eines Modells konnte die Oberflächentemperatur dieser verschiedenen Seen im Jörigebiet

berechnet werden, ohne dass meteorologische Messungen an diesen Seen gemacht wurden. Dies eröffnet neue Perspektiven für die Forschung von Hochgebirgsseen, wo die Wassertemperatur nun möglicherweise berechnet werden kann, ohne dass Messungen am See selber erhoben werden. Die Basis für diese Berechnungen wurde gelegt durch die Tatsache, dass die heterogenen Seewassertemperaturen im Einzugsgebiet der Jöriseen auf die Form des Einzugsgebiets, die Tiefe der Seen, die Trübung und die Windgeschwindigkeit zurückgeführt werden können. Die anderen meteorologischen und morphologischen Einflussgrößen sind vergleichsweise homogen in einem Einzugsgebiet und haben deshalb nur kleine Auswirkungen auf die Heterogenität der Seewassertemperaturen.

Die Fehler bei der Berechnung der Oberflächentemperaturen waren bei jenen Seen am höchsten, welche Schmelzwasser vom Gletscher erhalten. Auf Grund ihres grösseren Partikelinhalts erscheinen diese Seen heller. Die Auswirkungen der grösseren Partikelkonzentration sind gross für die Organismen in den Seen, da die Partikel sehr wichtig sind für die Absorption und Streuung der Globalstrahlung. In Seen mit Gletscherschmelzwasser ist die photische Zone teilweise weniger als 4 m dick, während sie in klaren Bergseen die maximale Tiefe der Seen meistens übertrifft. In Seen mit hoher Partikelkonzentration korreliert das Albedo mit dem Lichtabschwächungskoeffizienten. In solchen Seen kann das Albedo Werte von über 0.2 erreichen. Dieser Effekt muss in Energiebudgetberechnungen berücksichtigt werden, wenn keine grossen Fehler entstehen sollen.

Die Eisbedeckung der Seen im Winter ist wichtiger für die Abschwächung der Globalstrahlung als die Partikel, währt das Eis doch durchschnittlich 9 Monate pro Jahr auf den Jöriseen. Der Zeitpunkt des Zufrierens ist äusserst schwierig zu bestimmen, wenn nur meteorologische Messwerte und Modelle benützt werden. Da ein See innerhalb weniger Stunden teilweise oder vollständig zufrieren kann, ist die Anwendung von 0- oder 1-dimensionalen Modellen limitiert. Ein Grad-Tag-Modell, angepasst an die maximale saisonale Schneehöhe, wurde entwickelt und kalibriert für Jörisee III. In älteren Modellen wird für jedes Jahr dieselbe Eisdicke angenommen. Daten von Jörisee III zeigten, dass dies in Hochgebirgsseen nicht angenommen werden kann. Das neue Modell sagt die Eisschmelze mit einer Standardabweichung von 2 Tagen voraus. Die Daten der letzten 40 Jahren lassen auf eine stetige Verfrühung der Eisschmelze schliessen, insbesondere seit 1988. Dies konnte auf eine erhöhte Lufttemperatur auf Weissfluhjoch in den Monaten Mai und Juni zurückgeführt werden. Der Grund dieses Erwärmungstrends konnte allerdings nicht eruiert werden.

1 Introduction

High mountain lakes - Lakes in high mountain regions are interesting and important ecosystems because they are situated at the very top of the water cycle and usually experience no direct anthropogenic pollution (Wathne et al., 1995). Interest in these systems has been spurred by the recent discussions about global warming trends, since high mountain lakes are considered to be highly sensitive indicators of global changes (Sommaruga-Wögrath et al., 1997; Skjelkvale and Wright, 1998). Within framework of this project it was of interest to know how organisms react and adapt to the harsh and highly variable living conditions prevailing in aquatic mountain habitats. In order to identify possible ecosystem changes in high mountain lakes, the essential ecosystem determinants needed to be described and their possible variations evaluated. In the present study, several physical ecosystem determinants are described and some are integrated into a model. Emphasis was placed on temperature variations in mountain lakes and the global radiation distribution in particle-rich glacial lakes.

The MOLAR project - The research carried out at the Jöri site was part of the European project MOLAR (**M**ountain **L**ake **R**esearch). The lakes studied in the Jöri catchment are located within an area of 3 km². It was the goal of MOLAR to measure the dynamic reaction of remote high mountain and arctic lakes to changes in nutrient and pollutant concentrations and to model possible future changes based on these measurements. Over 20 laboratories in 14 European countries participated in the project. Research at the Jöri site was carried out by several different institutes and universities.

Meteorology - Since water temperature is one of the essential ecological determinants of lakes, an important question was whether the Jöri Lakes exhibit similar water temperature variations, and, if not, what determines temperature differences. The geographic location of a high mountain lake may play an important role in the seasonal temperature development (Livingstone et al. 1999). Generally, the most important factor for lake temperature differences is the heterogeneous distribution of meteorological variables. Based on measurements made at a station placed in the center of the catchment and at automatic weather stations nearby, an evaluation was made of whether meteorological conditions can be approximated with sufficient accuracy to allow their use in lake temperature modeling.

Longwave radiation - Measurements of longwave radiation still tend to be quite expensive and difficult. For this reason, researchers in various scientific fields often rely on parameterizations (Aubinet, 1994). Accurate longwave radiation data are important for energy budget calculations of the earth's surface (Olyphant, 1986). An existing model for the calculation of longwave radiation from screen level measurements was

modified for high mountain environments. The input parameters of the model are air temperature, relative humidity and global radiation. It was evaluated whether this model yielded better results than previously described parameterizations (e.g. Idso and Jackson, 1969; Konzelmann et al., 1994).

Lake energy budgets - For lowland lakes it is generally accepted that heat fluxes from sediments, throughflow and precipitation are insignificant for energy budget calculations (Marti and Imboden, 1986; Livingstone and Imboden, 1989; Hondzo and Stefan, 1993). Several investigations (Livingstone et al., 1999; Bengtsson and Svensson, 1996; Kuhn, 1977) indicate that this is not true for small high mountain lakes. One question is whether there are heat flux components in mountain lakes which are not important in lowland lakes. The data gathered for the Jöri lakes allowed us to calculate the effects of those heat flux components which are normally neglected in studies of lowland lakes.

Heterogeneity of water temperature - Water temperatures in a small catchment are not the same in all lakes, even if the meteorological forcing is similar. The main factors affecting this heterogeneity were evaluated. Lake surface temperature was also calculated for any given lake in the catchment, including those for which no measurements at the lake shore were available. The results were then compared to measured lake temperatures and explanations for any discrepancies found were sought.

Suspended erosion particles - A glacier still covers a significant portion of the Jöri catchment. The concentration of inorganic particles is usually high in glacial lakes, due to the suspended "rock flour" originating from mechanical rock erosion in the glacier bed (Koenings and Edmundson, 1991; Brown and Walsh, 1992). The particle concentration in glacial lakes dominates light absorption and scattering (Stefan et al., 1983). Information on the radiation properties at a certain depth in a lake is of importance for the definition of the living conditions of the biota. It is therefore crucial to know the particle distribution in a glacial lake if one intends to define the light field accurately. Frequently measured turbidity profiles in one particle-rich Jöri lake provided enough information to describe the light distribution in that lake.

Ice cover processes - The most dramatic physical event which influences lake ecology is the build-up of an ice cover in fall or winter. An ice cover with an overlying snow cover virtually decouples the lake water from atmospheric processes (Gray and Male, 1981). The biological activity is reduced to chemotrophic processes below the ice sheet. The duration of the ice-cover is important for lake oxygenation, phytoplankton production, species compositions and abundance (Livingstone, 1997). It is thus important to know the duration of the open-water period and the ice cover period. The most obvious procedure, apart from visually observing the ice processes, is to create energy budget models which can predict the freeze-over and break-up dates of lakes

(Heron and Woo, 1994; Fang et al., 1996). However, the ice-processes in lakes and especially those in high mountains are extremely heterogeneous (Gray and Male, 1981), and do not allow the ice cover duration to be predicted precisely. The major limitations of these models are discussed in chapter 6 and a simple alternative method for predicting the ice cover decay will be introduced. This method was developed using visual observations and meteorological measurements from a station outside the catchment.

Outlook - Up to now, expensive and time-consuming investigations have had to be carried out in order to define the physical ecosystem determinants of high mountain lakes. The goal of this study was to define the essential characteristics of the lakes and the main meteorological forcing variables. With the new knowledge, the processes in other lakes can be evaluated roughly without extensive measurement campaigns and the suitability of a lake for new research questions can be determined more rapidly and more easily.

Seite Leer /
Blank leaf

2 Morphology of the Jöri catchment and its lakes

2.1 Introduction

Among other factors, the size and form of a catchment are important in determining the physical ecosystem determinants in a lake. Aside from precipitation, the catchment size also determines the amount of water flowing into the lake. The skyline of the lake which can be responsible for shading the lake from global radiation, is partly determined by the slopes in the catchment. Slopes, expositions and altitudes in the catchment are factors influencing the snow cover distribution, which is important in connection with meltwater production. With a digital elevation model, the skyline as well as the slopes and expositions of all points in the Jöri catchment could be calculated. This formed the basis of the global radiation calculations described in chapter 3.7. The calculated catchment areas helped to give an estimate of the water exchange rates of the lakes, which may be an important factor for their energy budgets (see chapter 5.3).

2.2 Catchment description

The Jöri catchment is situated close to the Flüela pass east of Davos, Switzerland at 46° 46'N and 9° 58'E. Its 3.05 km² area covers altitudes from 2489 m to 3030 m a.s.l. and it corresponds to the catchment of the lowest lying Lake I. There are about 20 lakes within the basin, 13 of which have an area greater than 1000 m². Each of the lakes is identified by a Roman numeral which was originally assigned by Kreis (1920) (and by Summa (1998) for the lakes which were recently exposed by the retreating glacier ice). The whole basin was initially formed by a glacier that is retreating, but still covers an area of about 0.3 km². All lakes with a Roman numeral above XIII were still under the glacier ice at the time when Kreis did his research. According to old topographic maps, Lakes XII and XIII emerged from the glacier ice in the early 20th century.

The overall exposition of the basin is towards east and north due to the existence of high mountains to the west and the south. More than 60 % of the catchment faces towards directions between northwest and east. A small ridge at the northern end of the catchment makes the plateau between Lakes I and VII look like an east-west oriented valley. Several small plateaux with lakes of different sizes exist between the lowest and highest points of the catchment. The surroundings consist mostly of large rocks and some clay-filled flood plains with only sparse vegetation. Only about 10 % of the catchment is covered with soil and vegetation, 90 % can be considered to be bare rock, apart from the glacier and the lakes, which together account for about 15% of the total catchment area. An overview of the catchment is given in Figure 2.1.

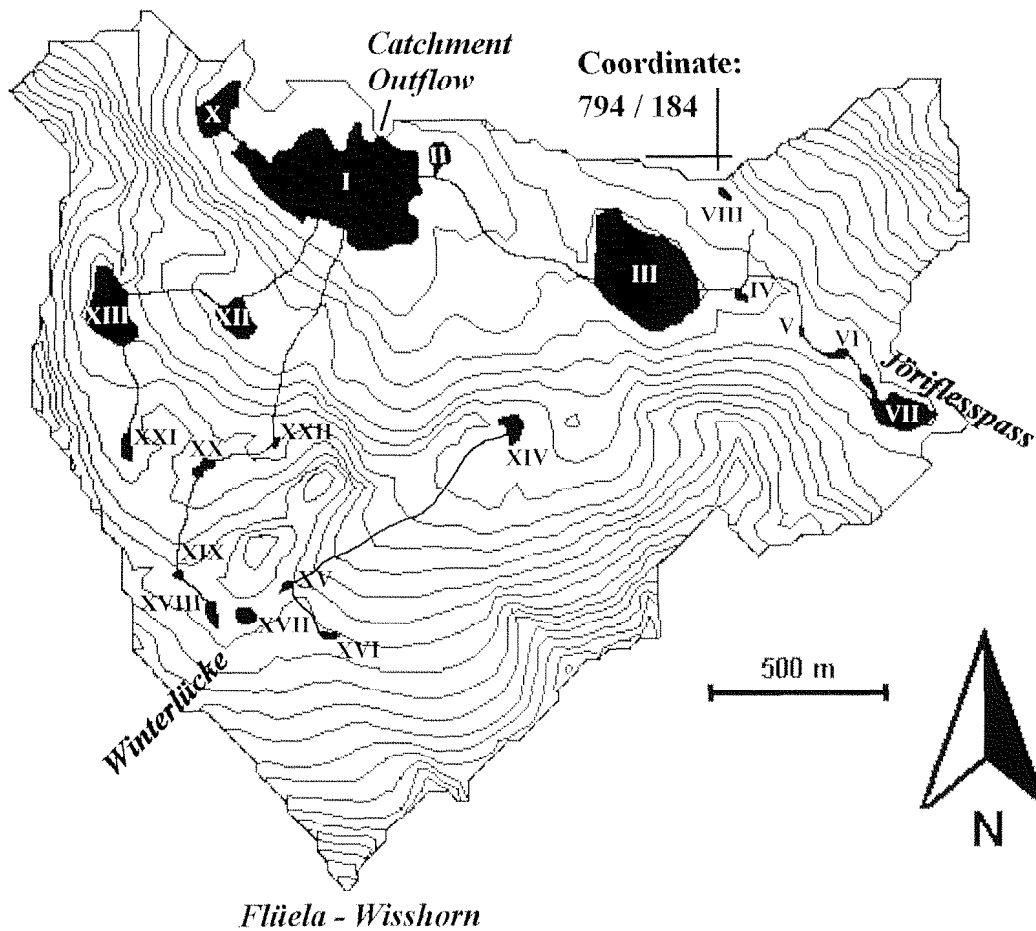


Figure 2.1: Contour map of the Jöri catchment including the lakes and major streams. The contour interval is 20 m, with the lowest contour being 2500 m around Lake I. The southernmost point (close to Flüela - Wisshorn) is the highest, with an altitude of 3030 m. In the upper right-hand corner a reference point for the Swiss Coordinate System is given (795 / 184). The figure is based on the digital elevation model DHM25, reproduced with the authorization of the Swiss Federal Office of Topography (BA4699).

For the exact morphological description of the Jöri catchment, a digital elevation model (DEM) with a resolution of 25 m was provided by the Swiss Federal Office of Topography. In a first step the 4903 grid points situated inside the Jöri catchment were determined. This was done using the topographic map. At places where the catchment delineation could not be determined from the map, the points in question were determined in the field. For all grid points within the catchment, the slope and the exposition were calculated. In Figure 2.2a+b the distributions of altitude and slopes within the catchment are displayed. The grid points are distributed more or less homogeneously between 2475 m and 2750 m a.s.l. Only about 15 % of the grid points are located in the upper half of the catchment (i.e., >2750 m a.s.l.). The slope distribution indicates that the catchment is generally rather steep, with the largest group

of grid points lying on slopes with an inclination of between 20 and 22°. The local maximum at an inclination of 0° is due to the many lakes in the catchment. The steepest slopes at grid resolution are 58°. The exposition distribution in Figure 2.3 clearly shows that most of the grid points face in directions from northwest to northeast and therefore receive little global radiation. Only 17.3 % of the grid points face towards southerly directions (southerly 180°). Of all the grid points, 293 were disregarded because they did not have an exposition due to the slope being 0°.

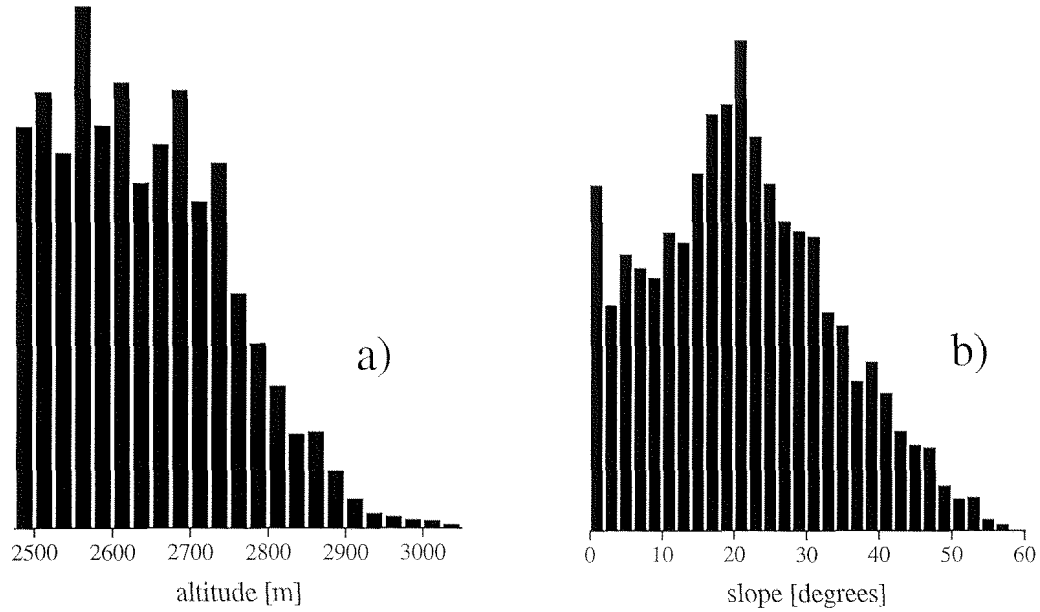


Figure 2.2: a) Histogram of altitude distribution of the Jöri catchment, group size is 25 m. b) Histogram of slope distribution of the Jöri catchment, group size 2°. The length of the bars correspond to the number of values in a given interval.

In order to be able to calculate the distribution of global radiation over the catchment area, the skyline was calculated at each grid point within the catchment. The angular resolution of the calculated skylines was 2°. The horizon between these points was linearly interpolated. The algorithm used to calculate the skylines was taken from Dozier and Frew (1990). Since the DEM was only available for an area of 3 km by 3 km, skylines outside this area were not included. This only leads to small errors in global radiation calculations because the horizon obstruction beyond the 9 km² area is mostly towards the north, where the sun is below the horizon at all times.

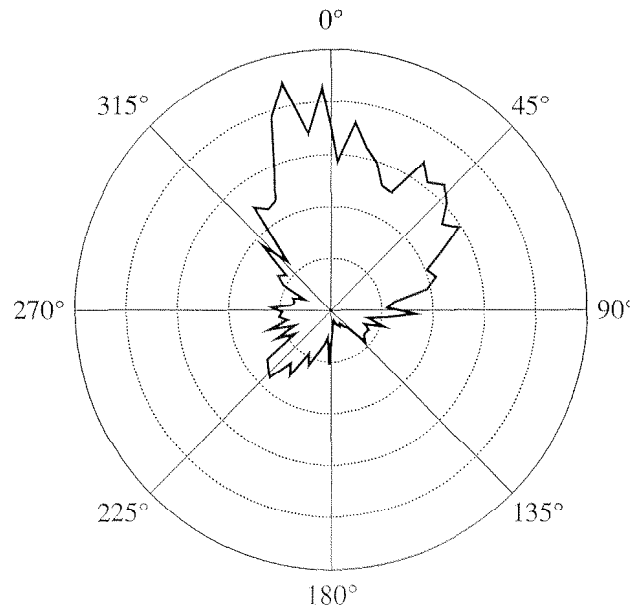


Figure 2.3: Polar graph of the exposition distribution of the Jöri catchment. Class size is 5°. An exposition of 0° corresponds to grid points facing north, an exposition of 90° to points facing east.

2.3 Description of the largest lakes and their surroundings

The lakes in the Jöri catchment are very diverse with respect to their morphological properties. In Table 2.1 these properties are presented for most of these lakes. The Roman numerals missing in the table belong to lakes which either are not inside the catchment or were too small to be represented in the digital elevation model. The altitude and the area of the lakes were determined using the digital elevation model. For all lakes with a volume larger than 7500 m³ the catchment was evaluated separately. The catchments mostly consist of loose rocks deposited by the glacier. Defining the catchment delineation was sometimes difficult due to subsurface flow paths. Lake depth was either measured during this study period (Lakes III, XIII and XIV) or taken from Kreis (1920). Lake volume was calculated exactly only for Lake III using a bathymetric map (see chapter 2.3.1). For the calculation of the volumes of the other lakes, similar bathymetries as for Lake III were assumed.

| Lake numeral | altitude a.s.l. [m] | Lake Area [m ²] | Maximum lake depth [m] | Approximate lake volume [m ³] | lake catch- ment area [ha] |
|--------------|---------------------------|--------------------------------|------------------------------|-------------------------------------------------|----------------------------------|
| I | 2489 | 93,700 | 10.4 | 370,000 | 305 |
| II | 2493 | 5,500 | 1.2 | 3,000 | n.a. |
| III | 2519 | 54,300 | 21.8 | 600,000 | 125 |
| IV | 2530 | 810 | 0.8 | 300 | n.a. |
| VI | 2550 | 1,400 | 1.3 | 700 | n.a. |
| VII | 2557 | 11,700 | 8.6 | 40,000 | 16.5 |
| VIII | 2550 | 700 | 0.7 | 200 | n.a. |
| X | 2493 | 9,800 | 6.8 | 25,000 | 16 |
| XII | 2571 | 7,200 | 4 | 15,000 | 35 |
| XIII | 2639 | 15,400 | 10 | 80,000 | 22.5 |
| XIV | 2610 | 4,400 | 4 | 7,500 | 62 |
| XV | 2730 | < 500 | n.a. | n.a. | n.a. |
| XVI | 2740 | < 1000 | n.a. | n.a. | n.a. |
| XVII | 2750 | 2,300 | n.a. | n.a. | n.a. |
| XVIII | 2730 | 2,400 | n.a. | n.a. | n.a. |
| XIX | 2725 | 410 | n.a. | n.a. | n.a. |
| XX | 2670 | 1,700 | n.a. | n.a. | n.a. |
| XXI | 2670 | 1,700 | n.a. | n.a. | n.a. |
| XXII | 2650 | 570 | n.a. | n.a. | n.a. |

Table 2.1: Morphological characteristics of most lakes in the catchment. Lake volumes were calculated assuming bathymetries similar to Lake III, adjusted for maximum depth. Lake IX is outside the catchment, Lake XI is too small to be on the map. (n. a. = data not available)

2.3.1 Lake III

Most of the research in the Jöri catchment focussed on Lake III, for which a bathymetric map was created. The data needed to create the map were collected during two days at the end of July 1997. At about 400 different points on the lake the depth was measured with a weight attached to a rope. The exact locations of these points were measured with a high resolution differential GPS provided by the Geodetic Institute of the ETH. The measured points were interpolated to a grid with 10 m spacing. The bathymetric map of Lake III is displayed in Figure 2.4. The outermost line represents the shoreline of the lake. The deepest point is situated close to the steep mountain slopes southeast of the lake. Close to the shore the lake bottom drops rapidly to depths around

5 m, below which depth there is a flatter section throughout most of the lake until 7 m or 8 m depth. Below 8 m the lake depth increases with gradually decreasing slopes until the maximum depth is reached at 21.8 m.

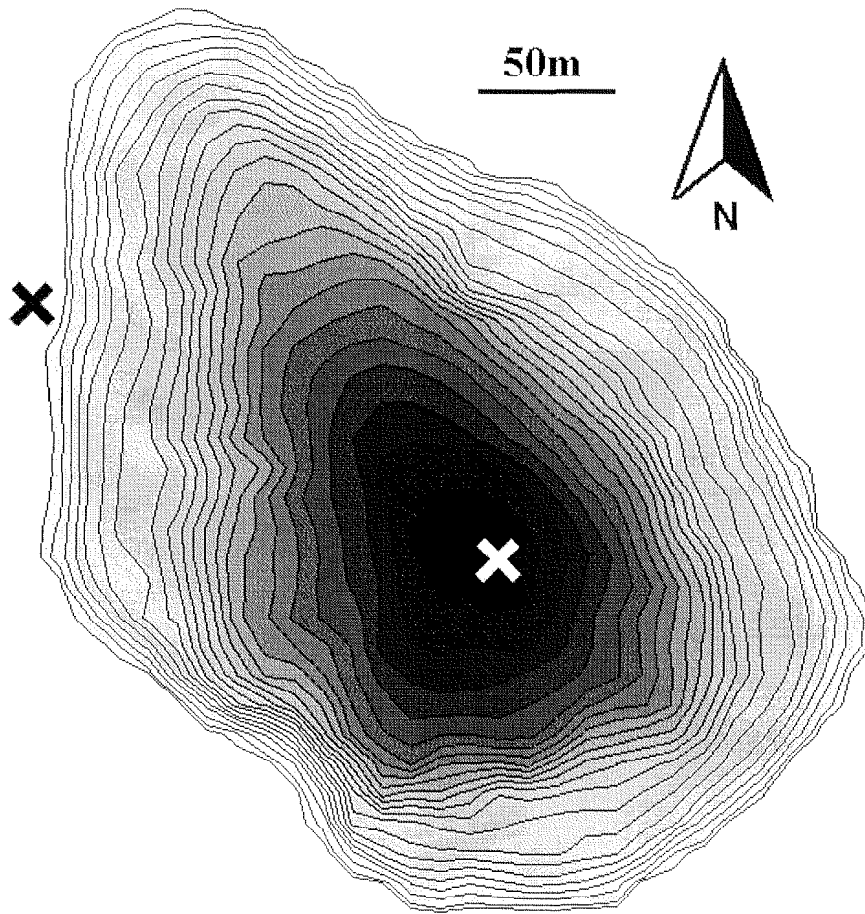


Figure 2.4: Bathymetric map of Lake III. The outermost line is the shoreline, line spacing is 1 m and the black area corresponds to depths below 21 m. A maximum depth of 21.8 m was measured at the white cross (Swiss Coordinates 793900 / 183700). The black cross indicates where the Jöri automatic weather station was situated.

Lake III has one major surface inflow coming from Lakes VII and VIII. As will be shown later (chapter 4) there is also a subsurface inflow which brings turbid glacial water from Lake XIV into Lake III. Towards the west, Lake III is dammed by an ancient moraine, which is covered by vegetation. However, it seems that the moraine does not dam the lake perfectly, since the lake level decreases as less water enters towards the end of the open-water season. The lowest level of Lake III is about 2.5 m below its highest level. During the observation period between 1996 and 1998, the lake level started to drop dramatically between 10 and 20 September, due to the lack of snow melting or rainfall. This is not necessarily always the case, in 1999 for example, heavy rainfalls towards the end of September caused Lake III to remain at a level less than 50 cm below the maximum until the beginning of October.

The skyline of a lake can be important for its radiation budget, most importantly for the solar radiation. Figure 2.5 shows that horizon obstruction at Lake III does not play a major role in the summer months. In fact, the lowest obstruction can be expected sometime in early October, due to a pass in the east at 90° . In the winter, however, almost all direct sunlight is blocked by the surrounding terrain. Because Lake III is frozen at that time there is virtually no effect on its energy budget.

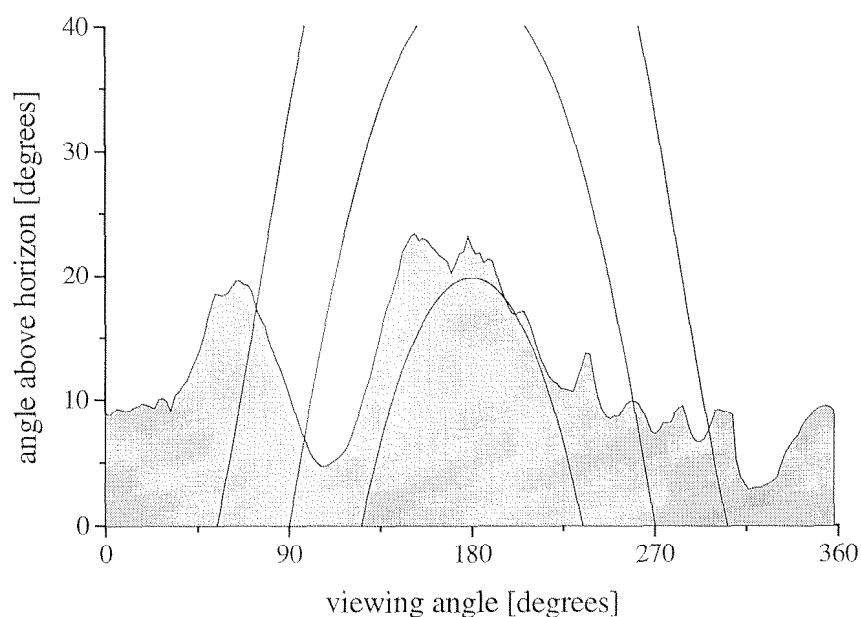


Figure 2.5: Skyline of Lake III (middle of lake). The lines represent the diurnal development of the sun elevation on 21 June (outermost line), 21 September and 21 December (innermost line).

2.3.2 Other lakes in the Jöri catchment

Because most of the research was carried out at Lake III, only a short description of the other lakes with volumes above 10000 m^3 will be given here. These include Lakes I, VII, X, XII and XIII and will be referred to as "large" lakes from here on. Many lakes in the catchment are connected in a cascade-like system, the most striking being the stream flow from Lake VII to Lake I, which flows through all lakes with numerals between I and VII. Water from Lakes X and XII flows directly into Lake I, while Lake XIII water first flows into Lake XII (see Figure 2.1). All the water from the Jöri catchment flows into Lake I eventually, making Jöri Lake I catchment equal to the total Jöri catchment.

The skyline was determined for the middle of all large lakes. Although the distance between two large lakes can be up to 2 km within the Jöri catchment, the horizon obstruction is quite similar at all lakes. Towards the east, the skylines are at 10° or below; towards the south, they are between 10° and 20° and towards the west, 20°

and higher. Lakes X and XIII experience skylines of more than 30° towards the west. During the open-water period, only shading from the west is therefore likely to be of any importance. Towards the east, the skylines are generally low and towards the south sun elevations are high enough to exceed all skylines. The higher skylines at Lakes X and XIII cause the sun to be shaded earlier in the day by the mountains. The mean global radiation input into these lakes is therefore smaller.

The bottom of most lakes consists of dark rocks and sediment. This causes the lakes to appear mostly black from above, even if they are not very deep. Only the lakes with glacial meltwater input (I, II, III, XIV, XV, XVI, XVIII, XIX, XX) are usually of a lighter color, due to high particle concentrations (see chapter 4.3.2).

3 Meteorological variability

3.1 Introduction

When working on a single research site it is of importance to establish one's own meteorological station, collect the data needed, and analyze the data in a format optimal to one's tasks. However, many ecological and also physical questions are now being addressed over large areas, from catchments and other small research areas to global scales that require meteorological data on virtually continuous spatial scales, precluding individual data gathering efforts (Running et al., 1987). Automatic weather stations (henceforth AWS) are usually scarce in mountain environments. Due to the harsh weather conditions prevailing at mountain sites with frequent snowfall and strong winds, the stations have to be looked after more frequently than in the lowlands. The accessibility of mountain stations is often limited, making it difficult to obtain accurate data sets.

Measurements from mountain-top stations are not generally suitable for calculating the energy budgets of lakes located in valleys between mountains. We carried out measurements at the Jöri lake sites and found that certain meteorological variables differed substantially from those measured at mountain stations nearby. The reason for these differences were investigated and their magnitudes determined. We also evaluated how well the meteorological values measured at the mountain top AWSs represent the conditions in the entire lake catchment.

3.2 Jöri automatic weather station

At the start of the project at the Jöri lakes, on 14 July 1996 an AWS was installed at the western shore of Lake III (Figure 2.4). In the following, this station will be referred to as "Jöri AWS". The meteorological measurements were recorded at 10-minute intervals during the open-water period and at hourly intervals during the rest of the year. The variables measured included air temperature, relative humidity, wind speed and direction, global radiation, longwave radiation and precipitation. Technical specifications of the sensors are given in the appendix. These variables, except for precipitation, were recorded throughout the project until September 1999. Precipitation was only measured during the open-water periods. The energy for the instruments was supplied by four solar panels. This limited energy supply did not allow for heating or ventilating instruments, which caused some errors that will be discussed specifically for each sensor. We experienced only a few periods of complete data loss, due either to logger malfunction or to energy shortage. Energy loss was observed when snow covered

the solar panels or when the batteries were emptied due to heavy laboratory activity. Figure 3.1 shows the data availability for the project period 1996 to 1999.

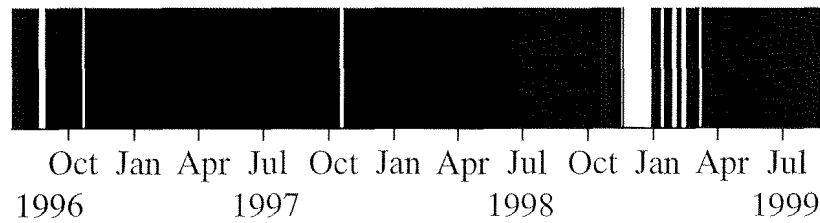


Figure 3.1: Availability of meteorological data at the Jöri AWS. White bars indicate a complete data loss.

For reasons of comparison two additional AWSs were installed during the summer of 1997 at the shores of Lakes VII and X, both at a distance of about 1 km from the AWS at Lake III. Except for longwave radiation, the same parameters were recorded as at the central Jöri AWS at Lake III. The measuring period was from 10 June through 20 October 1997. Except for the aspirated air temperature sensors, the sensors and gauges were neither ventilated nor heated.

3.3 Measurements at AWSs outside the Jöri catchment

| Institute | AWS Station name | Distance from Jöri AWS [km] | Altitude [m] | station location |
|-----------|------------------|-----------------------------|--------------|----------------------------------|
| WSL | Stillberg | 8.3 | 2090 | valley side, facing northeast |
| SLF | Gatschiefer | 8.0 | 2310 | valley side plain, facing west |
| UNIZH | Jöri Lake III | 0.0 | 2520 | valley bottom |
| SLF | St. Jaggem | 18.0 | 2542 | mountain ridge at side of valley |
| SMI | Weissfluhjoch | 14.4 | 2693 | mountain top |
| SLF | Piz Müra | 17.4 | 3160 | mountain top |

Table 3.1: Automatic weather stations close to the Jöri catchment, at altitudes above 2000 m. Exact data sources are given in the appendix. Institute abbreviations are explained in the text.

The data of the Jöri AWS were complemented with observations of weather stations from the Swiss Meteorological Institute (SMI), the Swiss Federal Institute for Snow and Avalanche Research (SLF) and the Swiss Federal Institute for Forest, Snow and Landscape Research (WSL). Table 3.1 shows the data provided and the distances of the stations from the Jöri AWS. The dense network of weather stations around the Jöri site provided good information for the calculation of temperature lapse rates, for

characterizing the regional meteorology and climate and for plausibility considerations of the measurements at Jöri.

Data from Weissfluhjoch were available from an electronic database covering the period 1959 to 1999. The systematic differences in meteorological values between Weissfluhjoch and Jöri could be corrected reliably, so that the Weissfluhjoch database provided an excellent estimate of the climatic conditions at the Jöri AWS. Additional global and longwave radiation data were provided by the World Radiation Center in Davos for the AWSs Weissfluhjoch, SLF Research Field and Payerne. The research field of the SLF is located 600 m southeast of Weissfluhjoch, at an altitude of 2540 m. Payerne is about 200 km from the Jöri catchment, at an altitude of 490 m.

3.4 Air temperature

Air temperature is mainly affected by radiative energy from the sun and the atmosphere as well as by air mass advection induced by global circulation. Within the troposphere the air temperature usually decreases with height at a rate of between $5 \text{ K}\cdot\text{km}^{-1}$ and $10 \text{ K}\cdot\text{km}^{-1}$ (Roedel, 1994). It was expected that this would also be true for air temperatures within the Jöri catchment. Higher lying lakes would experience lower air temperatures than lower lying lakes. The investigations show that this is not always true.

3.4.1 Measurement errors and correction

One of the difficulties in measuring air temperature is the heating of the thermometer due to exposure to direct radiation or the cooling of the thermometer due to radiative heat loss from the sensor. A simple solution to this problem is to mount a multiplate protective radiation shield around the thermometer to shade it from the sun. This was done at Jöri AWS. This approach may be ineffective at low wind speeds, since the radiation shield is heated by radiation, and without sufficiently high wind speeds to cool the shield, the thermometer measures the temperature of the heated shield and not the true air temperature.

An aspirated thermometer was added to the Jöri AWS for the period between 10 March 1998 and 2 July 1998 to provide accurate air temperature measurements under low wind conditions. Due to the availability of simultaneous aspirated and shielded temperature measurements for the stated period, a correction for the shielded thermometer was sought to account for the heating and cooling of the radiation shield. As this comparison showed, the difference between the aspirated and the shielded sensor was only proportional to the global radiation measurements during the snow cover period. This implies that the shielding of the standard temperature sensor against direct sunlight is sufficient for the conditions at this site even at low wind speeds. But

since there seems to be a heating effect induced by global radiation reflected at the snow surface, a simple model was designed which predicted the heating and cooling of the shielded thermometer during times of snow cover based on a comparison of the aspirated and non-aspirated temperature measurements.

There is a significant linear dependence between global radiation and the additional heating of the shielded thermometer ($p < 0.05$, $r^2 = 0.41$, Figure 3.2). The dependence between wind speed and temperature increase due to heating is clearly logarithmic, with high deviations at low wind speeds and values close to 0 K at wind speeds above $2 \text{ m}\cdot\text{s}^{-1}$ (Figure 3.3).

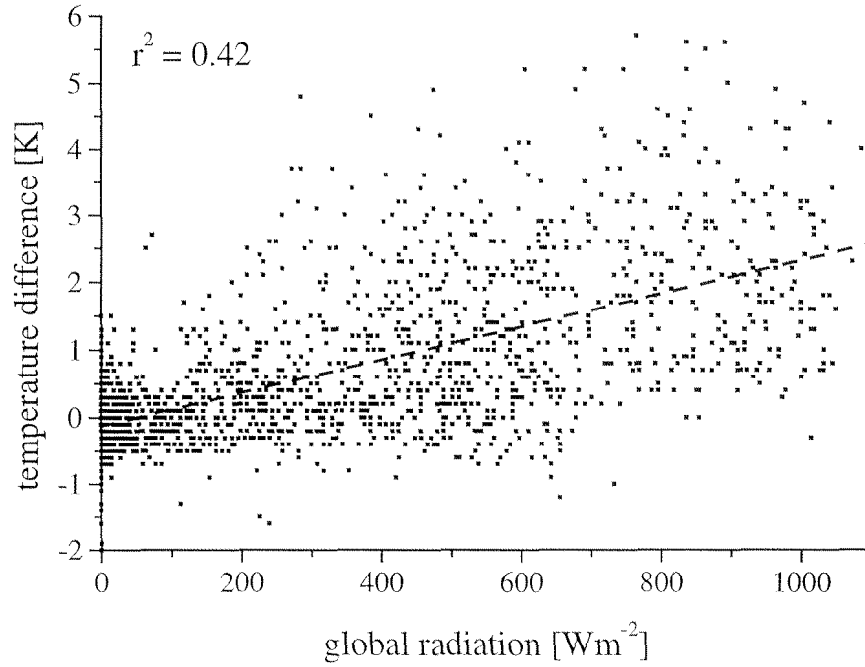


Figure 3.2: Scatterplot of global radiation and the temperature difference between the aspirated and the shielded temperature sensors at the Jöri AWS. Hourly means were plotted during the period from 10 March to 20 June 1998

The model combines global radiation with wind speed in a way that optimizes the prediction of accurate temperature T_{acc} :

$$T_{acc} = T_{sh} + R_{sw} \cdot (-0.0015 \cdot \ln(u) + 0.0026), \quad (3.1)$$

where R_{sw} is global radiation [$\text{W}\cdot\text{m}^{-2}$] and u is wind speed [$\text{m}\cdot\text{s}^{-1}$]. The expression in parentheses is set equal to 0.005 for $u \leq 0.1 \text{ m}\cdot\text{s}^{-1}$.

The regression between the aspirated and the shielded sensor yields an r^2 of 0.97 with a mean bias error of 0.45 K and a root mean square error of 1.1 K. The regression

between the aspirated sensor and the corrected values of the shielded sensor is, as expected, much better with an r^2 of 0.98, a mean bias error of -0.01 K and a root mean square error of 0.63 K. These corrections were applied to all air temperature measurements when snow covered the ground around the Jöri AWS.

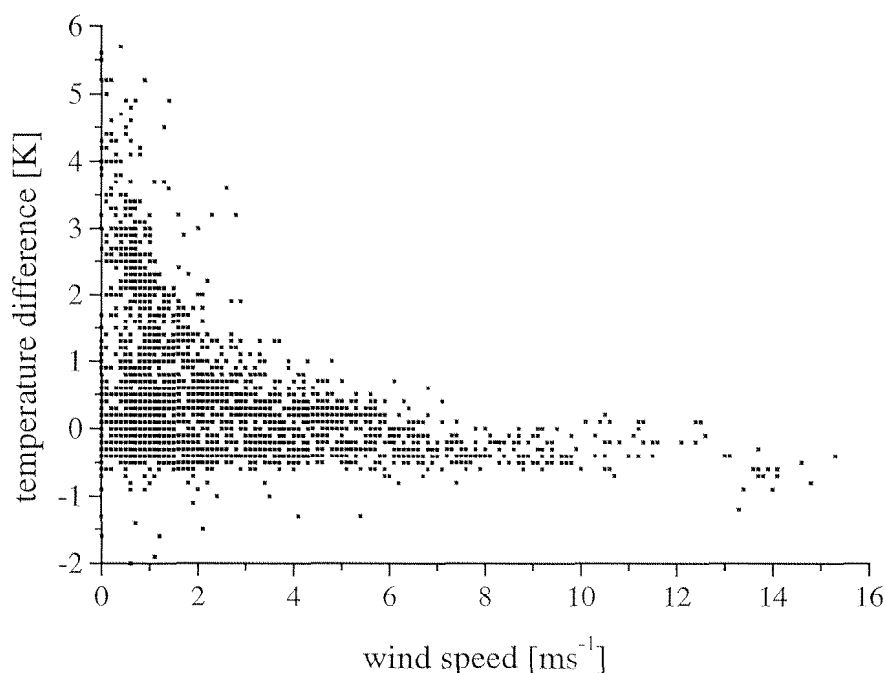


Figure 3.3: Scatterplot of wind speed and the temperature difference between the aspirated and the shielded temperature sensors at the Jöri AWS. Hourly means were plotted during the period from 10 March to 20 June 1998.

Snow inside the multiplate protective radiation shield can be another source of error. When snow falls during high wind speeds, it can accumulate inside the shield, thereby decreasing air temperature due to the conduction of energy from the sensor to the cold snow.

The mast of the Jöri AWS is located at the side of the laboratory shed. Due to the radiative properties of the shed, snow tends to melt around it before it melts at other flat places in the catchment. Therefore, the air temperature may also be affected by the snow-free area around the measuring station, since snow-free ground absorbs more global radiation than snow-covered ground.

Since the temperature sensor at Lake III was not installed at a standard height of 2 m above ground, but at 6 m, the measured air temperatures are probably higher at times when strong air temperature inversions persist. The magnitude of these differences is not known, but is expected to be significant only during clear winter nights.

3.4.2 Regional heterogeneity of air temperature

The heterogeneity of air temperature within a small high mountain region around the Jöri catchment was evaluated by comparing the daily mean air temperature lapse rates between the AWSs from SMI, WSL and SLF (Table 3.1). The use of data from mountain stations may result in erroneous atmospheric lapse rates due to the different expositions of the AWSs. Figure 3.5 shows that the correlation between altitude and air temperature is usually high. Only on a few days is r^2 below 0.9. The lapse rates from these mountain stations can therefore be used for air temperature approximations in the specified region. Data from all five external stations were available on 367 days between 1 October 97 and 31 October 98.

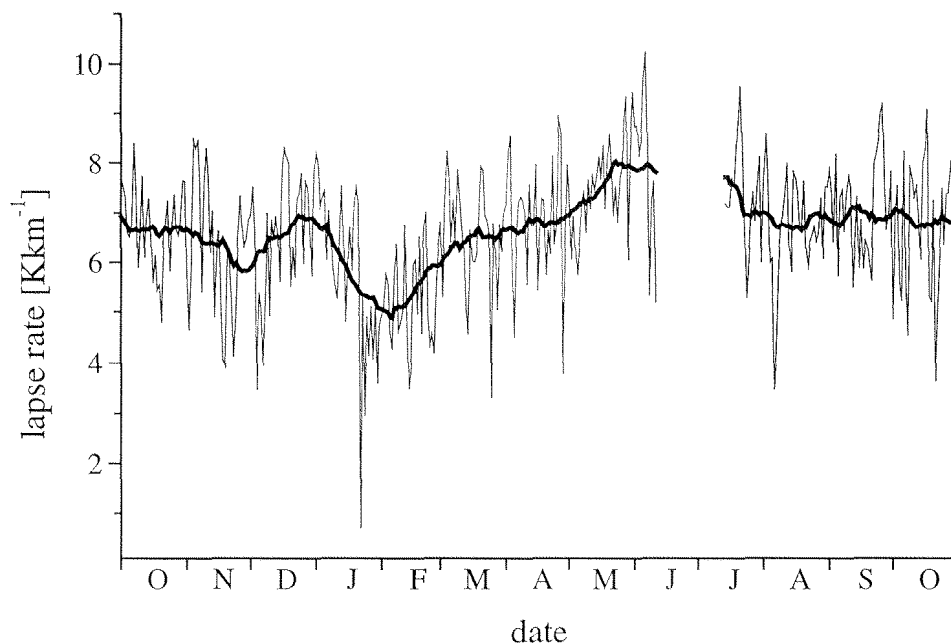


Figure 3.4: Daily mean air temperature lapse rates from 1 October 1997 to 31 October 1998 in the region around the Jöri Lakes calculated based on the data from the AWSs listed in Table 3.1. The thin line depicts the day-to-day variation while the thick line corresponds to 15-day means of the lapse rate.

The mean lapse rate over the year was $6.65 \text{ K} \cdot \text{km}^{-1}$, a value which is close to the generally accepted mean of $6.5 \text{ K} \cdot \text{km}^{-1}$ for the lower troposphere (Running et al., 1987). Convective activity induced by solar heating caused higher lapse rates in the summer (Figure 3.4). The highest lapse rates were observed between May and July, when solar elevation is highest. The day-to-day variability of the lapse rate is quite low, with 90 % of the values being between $4.5 \text{ K} \cdot \text{km}^{-1}$ and $8.5 \text{ K} \cdot \text{km}^{-1}$. The deviations are larger during the winter, e.g. on 22 January 1998, when the calculated lapse rate was $0.41 \text{ K} \cdot \text{km}^{-1}$, an unusually low value. Temperature sonde data from Payerne, 200 km from the study

region, showed that there was a strong temperature inversion between 2000 m a.s.l. and 3000 m a.s.l. on that day, causing air temperatures at Stillberg to be only slightly higher than those at Piz Müra. However, the scarcity of these low lapse rates indicates that large inversion layers at these altitudes are unusual.

The daily correlation of the linear regression between air temperature and altitude was calculated to get an indication of the scattering of the air temperature at the mountain stations around the calculated lapse rate (Figure 3.5). Above lapse rates of $7 \text{ K}\cdot\text{km}^{-1}$, r^2 is always high with values above 0.97. As the lapse rate decreases, so does r^2 , since low lapse rates are an indicator of inversion layers. If an inversion layer is situated between the stations, the temperature decrease with height is not linear, causing a low r^2 . Despite the occasional occurrence of low lapse rates, r^2 is below 0.95 in only 11.7 % of all cases and of these, 61 % occur during the period between November and February.

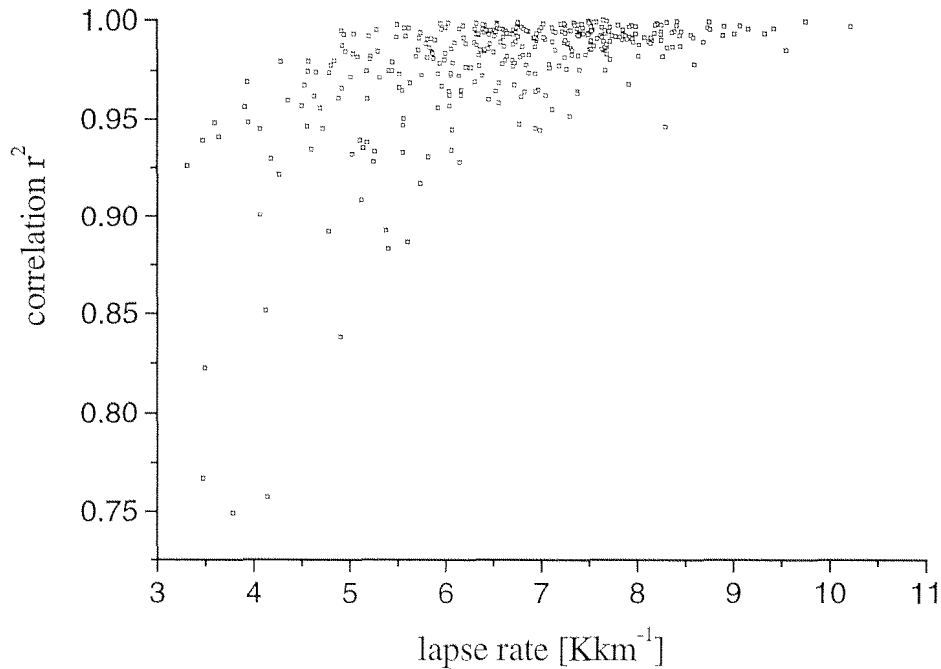


Figure 3.5: Dependence of daily mean r^2 of the linear regression between altitude and mountain air temperatures and the air temperature lapse rate between 1 October 1997 and 31 October 1998.

If the data from the Jöri AWS are included in the lapse rate calculation, r^2 is below 0.95 in 37.4 % of the cases. The lapse rates are not much different during the convectively active months, but from November to February r^2 is below 0.9 in 45 % of all days. This indicates that the Jöri AWS does not fit into the lapse rate calculated from the weather stations in the region, especially in the winter. This is most apparent if one

compares the 15-day mean of the air temperature differences between Jöri and Weissfluhjoch. For the periods 15 July to 14 July of the following year, a floating bar plot was created (Figure 3.6) using data from the years 1996 to 1999.

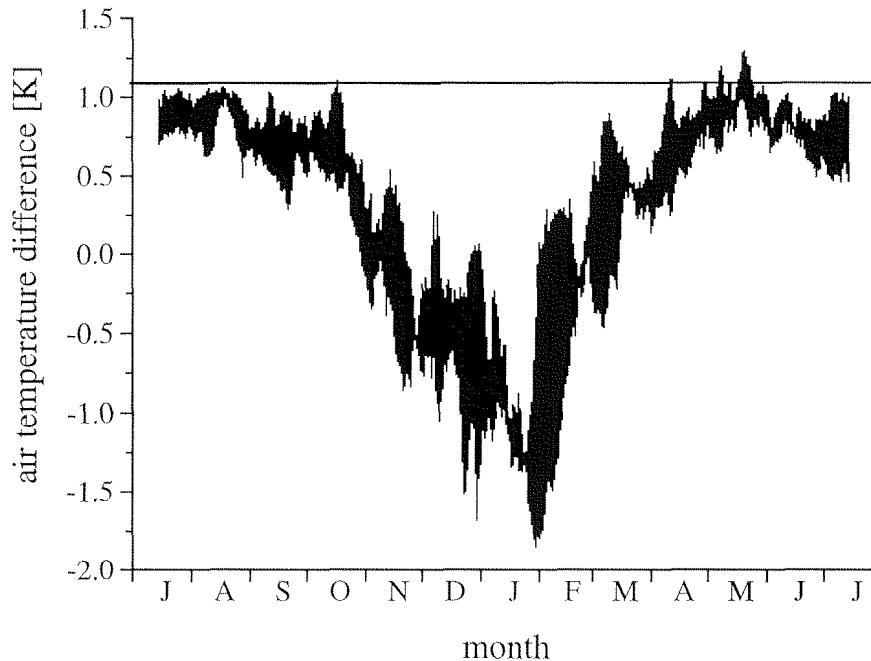


Figure 3.6: Daily range of air temperature differences between Jöri AWS and Weissfluhjoch AWS between 15 July 1996 and 14 July 1999. Values were averaged over a 15-day period. The horizontal line at 1.1 K is the temperature difference between Jöri and Weissfluhjoch at a lapse rate of $6.5 \text{ K} \cdot \text{km}^{-1}$.

The mean air temperature differences between Jöri and Weissfluhjoch AWSs were within the black area for all three years. The theoretical temperature difference at a constant lapse rate of $6.5 \text{ K} \cdot \text{km}^{-1}$ would be 1.1 K. This value was barely ever reached throughout the year, indicating that the air temperature at the Jöri AWS is lower than the local lapse rate suggests even in summer. The reason for the lower air temperatures at Jöri are the cold air masses which tend to build up inversions at the bottom of valleys. The strongest inversions build up when the radiation budget at the snow surface in the valley is negative, which happens during clear nights. At low wind speeds the inversion layer keeps growing until the radiation budget becomes positive with the first rays of sunlight in the morning. Mountain tops are unaffected by the cold air because it flows off to lower elevations due to its higher density compared to the air in the free atmosphere. The largest hourly mean differences of up to 8 K in air temperature between Jöri and Weissfluhjoch usually occurred just before sunrise. The largest daily mean differences of close to 5 K were registered around the winter solstice, when global radiation at Jöri is much lower than at Weissfluhjoch due to the skyline.

Large deviations not only occurred during calm and clear nights, but occasionally also during the day, at high wind speeds. This was probably due to cold inversion air from the Engadine valley being transported across the Jöri lakes by strong southerly winds.

Inside the Jöri catchment, air temperature was also measured at Lakes VII and X during the open-water period of 1997. These two lakes are also situated at the bottom of the Jöri catchment, both 1 km from the Jöri AWS. The altitude range of Jöri AWS, Lake VII and X AWSs is only 64 m. As a result, the air temperatures at these three sites behave similarly, except when the sites experience different global radiation input due to heterogeneous cloud cover or high skyline. The mean air temperatures over the measuring period fit the theoretical lapse rate of $6.5 \text{ K}\cdot\text{km}^{-1}$ well.

In 1998 four thermistors were installed to measure air temperature at Lake III, XIII, Rundseeli and Schottensee (for a description of the latter two lakes see chapter 5.5.2) in order to obtain an estimate of local air temperature variations within and just outside the Jöri catchment. Because of the insufficient shielding only hourly data recorded during nights where wind speed exceeded $2 \text{ m}\cdot\text{s}^{-1}$ at the Jöri AWS were considered, leaving a total of 547 values for the months of August and September 1998. Comparison of the mean temperatures at the four sites (Table 3.2) shows that temperature differences can be explained by altitude differences most of the time. The differences between the data calculated based on the lapse rates from the AWSs listed in Table 3.1 and the data measured with the thermistors show that not all of the temperature deviations can be explained by the lapse rate. The local terrain and the landscape position of a lake seem to have a temperature effect on the order of up to $\pm 0.5 \text{ K}$ during the night. The effect on the daytime values could not be evaluated, but it can be assumed that this will be smaller due to convective mixing in the boundary layer.

| | Schottensee | Lake III | Rundseeli | Lake XIII |
|-----------------------------------------------|-------------|----------|-----------|-----------|
| Altitude [m] | 2374 | 2520 | 2549 | 2639 |
| Measured temperature [$^{\circ}\text{C}$] | 5.19 | 4.44 | 4.74 | 3.76 |
| Calculated temperature [$^{\circ}\text{C}$] | 5.52 | 4.57 | 4.38 | 3.79 |
| Difference from lapse rate [K] | -0.33 | -0.13 | 0.36 | -0.03 |

Table 3.2: Mean of 547 hourly values during August and September 1998 for four stations inside and adjacent to the Jöri catchment. Calculated air temperatures are based on station altitudes and lapse rates calculated from data from the AWSs listed in Table 3.1.

3.4.3 Conclusions

In summer, when radiation-induced convection occurs frequently, air temperatures in the Jöri catchment can easily be approximated with data from mountain stations at distances of 15 km, possibly even more, when the lapse rate is accounted for. The lapse rate in high mountain areas is only rarely influenced by temperature inversion layers. The lapse rate, calculated from AWSs in a small region and at different altitudes, can be used for the interpolation of air temperatures in that region and within the altitude range of the AWSs. Deviations of the catchment air temperature from the mountain-top values are largest during the night, but do rarely exceed a mean value of 0.5 K in the months from April to September. For the other months of the year, air temperatures in mountain valleys and plateaux may be significantly lower than at mountain tops. The only time that this is significant for the energy budget calculation in Lake III is before it freezes over in October or November.

3.5 Humidity

Humidity can be measured and expressed in several different ways. Among these are absolute humidity ($\text{g}\cdot\text{kg}^{-1}$ air), vapor pressure (hPa), dew point (the air temperature at which saturation water pressure would be reached) and relative humidity (percentage of saturation vapor pressure at the prevailing air temperature). Relative humidity is not used often because for equal air masses, relative humidity changes with air temperature, whereas the other quantities are conservative with respect to air temperature. Only little attention has been given to the humidity distribution in mountainous areas. The vapor pressure is usually assumed to be relatively constant spatially over a relatively large area (Running et al., 1987; Greuell et al., 1997).

3.5.1 Measurement errors

At the Jöri AWS, relative humidity was measured under the same multiplate protective radiation shield as the air temperature (chapter 3.4.1). The measurement errors that arise from heating of the sensor are not as large when the data are converted to vapor pressure because vapor pressure does not change with temperature for the same air masses. As mentioned for air temperature measurements, snow and also water inside the radiation shield cause errors in humidity measurements since water vapor near the sensor is increased compared to the air masses in the catchment. This problem could also be solved with an aspirated humidity sensor.

3.5.2 Regional heterogeneity of humidity

Daily mean humidity values at the Jöri AWS and the 5 AWSs outside the Jöri catchment were compared. All values were converted from relative humidity rH to vapor pressure e_a according to the following formula (Roedel, 1994):

$$e_a = 6.1078 \cdot 10^{\frac{7.5T_a}{T_a+237.3}} \cdot rH, \quad (3.2)$$

where T_a is the air temperature. Water vapor e_a decreases with height due to the decreasing air temperature (Reitan, 1963):

$$e_a(z) = e_{a0} \cdot e^{-\beta \Delta z}, \quad (3.3)$$

where e_{a0} is the vapor pressure at reference height and Δz is the altitude difference between the reference height and the height where vapor pressure is to be calculated. The value of β varies with the mean temperature of the atmosphere. Reitan (1963) proposed a general mean value of $\beta = 0.44$. An exponential regression including all the humidity data from 6 AWSs in and around the Jöri catchment yielded $\beta = 0.365$ for the time from 1 January to 31 October 1998. The data of St. Jaggem did not fit into the regression, in contrast to the Jöri data which fit well (Figure 3.7). Vapor pressure values observed at St. Jaggem were regularly higher. It is not known, whether the St. Jaggem AWS is subject to frequent fog or whether the sensor was calibrated wrongly.

Linear regressions between the daily mean vapor pressure data from all 6 AWSs for the period from 1 January to 31 October 1998 showed that r^2 is mostly dependent on distance and altitude between two stations (Table 3.3). All the regressions including the one for Piz Müra, had a clearly lower r^2 , indicating that altitude plays a slightly more important role than distance in the determination of water vapor.

| r^2 | Gatschiefer | Jöri | St. Jaggem | WFJ | Piz Müra |
|-------------|-------------|-------|------------|-------|----------|
| Stillberg | 0.988 | 0.980 | 0.980 | 0.981 | 0.940 |
| Gatschiefer | 1 | 0.976 | 0.986 | 0.980 | 0.934 |
| Jöri | 0.976 | 1 | 0.977 | 0.980 | 0.951 |
| St. Jaggem | 0.986 | 0.977 | 1 | 0.984 | 0.943 |
| WFJ | 0.980 | 0.980 | 0.984 | 1 | 0.967 |

Table 3.3: Correlation r^2 of the linear regression of vapor pressure between AWS pairs for the period from 1 January to 31 October 1998. Forward and reversed comparison which give the same r^2 appear in the table.

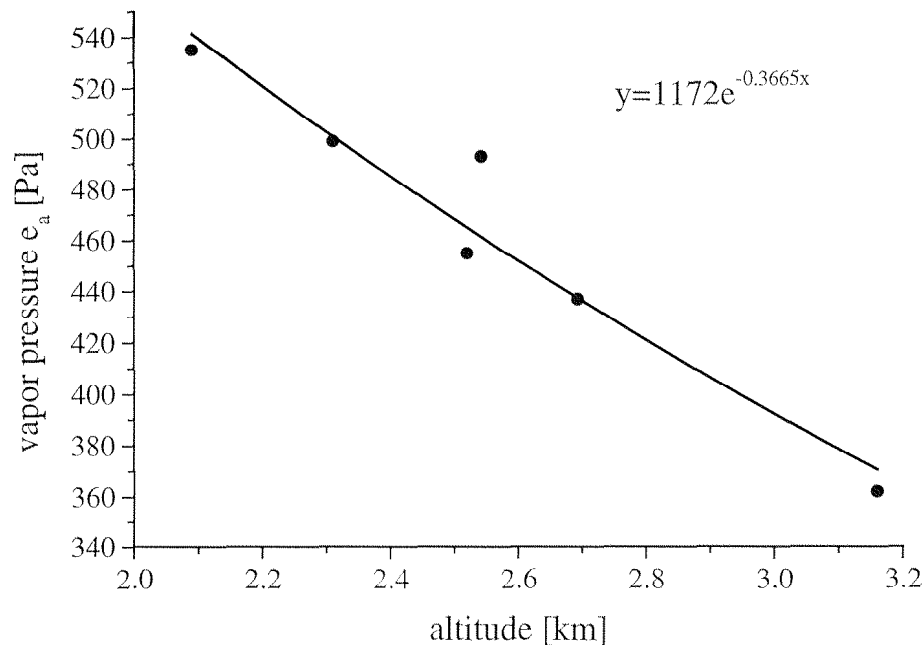


Figure 3.7: Exponential regression between altitude and mean vapor pressure for the period from 1 January to 31 October 1998 and the AWSs of Table 3.1.

3.5.3 Conclusions

On a daily basis, vapor pressure values of locations in high mountain regions can be approximated by using observations from nearby AWSs, even if the location is at a different altitude. If the altitude difference in between becomes too large, then the correlation of the regression between the data from the two stations becomes smaller due to the increased frequency of inversion layers between the two stations. Deviations from expected water vapor pressure at certain stations are difficult to explain if only a limited selection of meteorological parameters are measured at the site in question.

3.6 Wind speed and direction

Local circulation over complex terrain is influenced by features like differential heating of the ground and the surrounding air, surface characteristics (vegetation cover, moisture and water coverage, roughness), large-scale synoptic forcing, radiation and clouds (Koracin and Enger, 1994). The selection of measurement locations in complex terrain, frequency of sampling, and selection of synoptic situations always place limits on the completeness of information about local flows. Since the placement of the wind gauges within the Jöri catchment was not ideal for an analysis of air flow inside the

catchment, only point comparisons of wind speed and direction between different AWSs within and around the Jöri catchment were performed.

3.6.1 Measurement errors and problems

In winter, cold and moist air as well as snow can lead to the freezing of the wind gauge, causing data loss, sometimes for several consecutive days. This occurred most frequently between October and December when global radiation was too weak to melt the snow and ice from the gauge and air temperatures during snowfall events can be just below 0° C, enhancing the freezing of the snow to the gauge. Low wind speeds are difficult to measure with a cup anemometer because the latter starts rotating only above a certain threshold wind speed (Sweers, 1976).

Another problem arises when wind speed data from different networks are compared. Unless the wind gauges are installed at the same height above ground at all stations the data are biased since wind speed decreases close to the ground.

3.6.2 Regional heterogeneity of wind speed and direction

Wind speed and even more so wind direction are site specific in mountain regions. Wind speed and direction measurements on mountain tops are dominated by the synoptic-scale gradient wind while measurement sites at valley floors predominately experience the mountain and valley winds initiated by radiational cooling or heating of sloping surfaces (Greuell et al., 1997). Of the five AWSs Jöri Lake III, Gatschiefer, St. Jaggem, Piz Müra and Stillberg where wind direction data were available, only Piz Müra is a mountain top station. However, higher mountains towards the west shield Piz Müra from westerly air flows. Wind direction distribution graphs were plotted for the five stations mentioned above (Figure 3.8a-f). Data from 1997 was used, 10-minute means for Stillberg and 30-minute means for Gatschiefer, Piz Müra and St. Jaggem. At the Jöri AWS wind direction measurements were not reliable all through 1997, therefore hourly means from Summer 1996 and Winter 1998/99 were used.

Air flow at all five AWSs was rarely from the sector North to East. This is due to the synoptic scale circulation which rarely causes winds in the sector from North to East. The wind direction distributions in Figure 3.8a-e are very diverse. Although all stations are within a radius of 20 km and the atmosphere above the stations is subject to similar air flows, the predominant wind directions are by no means the same. The air flows at the AWSs are mostly affected by a high skyline nearby. The Jöri AWS is shielded by terrain towards all directions except southeast. Therefore by far the highest frequency of wind is from the latter direction. At St. Jaggem AWS the mean wind speed in 1998 was $2.5 \text{ m}\cdot\text{s}^{-1}$ over all directions. Mean wind speed from directions 270° to 300° however was $3.1 \text{ m}\cdot\text{s}^{-1}$. The situation at the Jöri AWS is even more extreme, with mean

wind speed being $2.9 \text{ m}\cdot\text{s}^{-1}$ over all directions from November 1998 to June 1999. When averaging over the directions from 90° to 150° , the mean wind speed over the same period was $4.5 \text{ m}\cdot\text{s}^{-1}$.

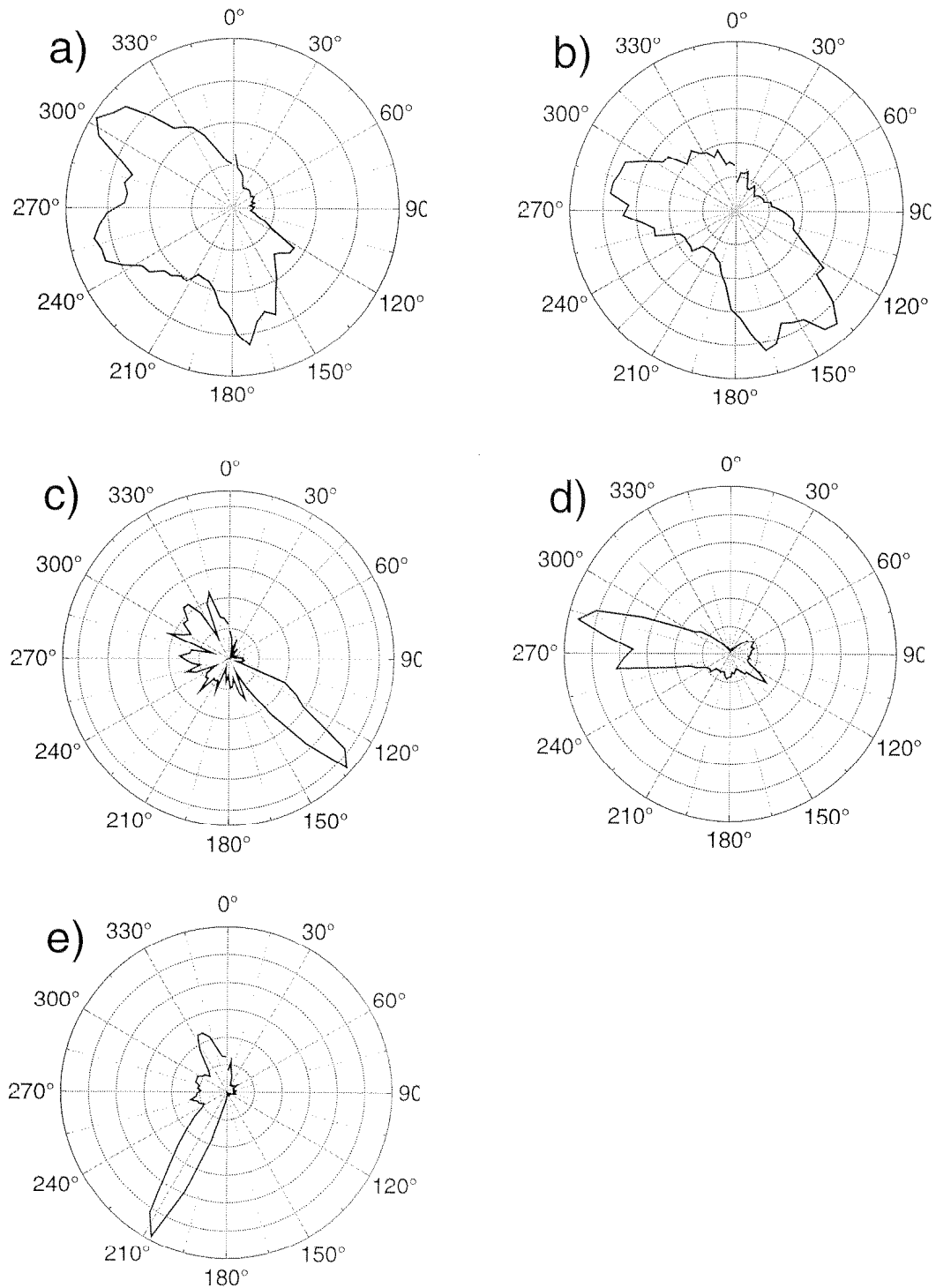


Figure 3.8a-e: Distribution of wind direction at six different AWS. a) Stillberg, b) Gatschiefer, c) Jöri, d) St. Jaggem, e) Piz Müra. Wind direction frequencies were determined for intervals of 5° . Points close to the origin indicate low wind direction frequency from the direction corresponding to the point. 0° indicates wind from the north, while 90° indicates wind from the east.

As expected r^2 of the linear regression of daily mean wind speeds is fairly low for all AWS pairs. The highest r^2 was 0.34 for the period from January 1998 to October 1998, recorded for the pair Weissfluhjoch and Jöri AWS. This means that for the use of wind speed in energy budget calculations of lakes (see chapter 5) it is essential to set up a wind gauge at the lake in question. Otherwise, errors caused by wrong wind speed data can be large. Even the linear regression of daily mean wind speeds between the two mountain top stations of Weissfluhjoch and Piz Müra yields an r^2 of only 0.24. Intuitively, they should both be subject to similar atmospheric forcing. However, both AWS are shielded by higher mountains towards the west, from where synoptic air flow comes most frequently.

Regardless of the poor correlation between all daily means, a method was found that could predict daily mean wind speed of the Jöri AWS using data from the St. Jaggem AWS. The idea was to split up the St. Jaggem wind data in an easterly and northerly component. These two components were weighted differently to calculate the daily difference between the wind speed at Jöri and St. Jaggem AWS U_{diff} in the period from 1 January to 20 November 1998:

$$U_{diff} = -0.35 - 0.22 \cdot U_E^{SJ} + 0.98 \cdot U_N^{SJ}, \quad (3.4)$$

where U_E^{SJ} is the easterly wind component and U_N^{SJ} is the northerly wind component at St. Jaggem.

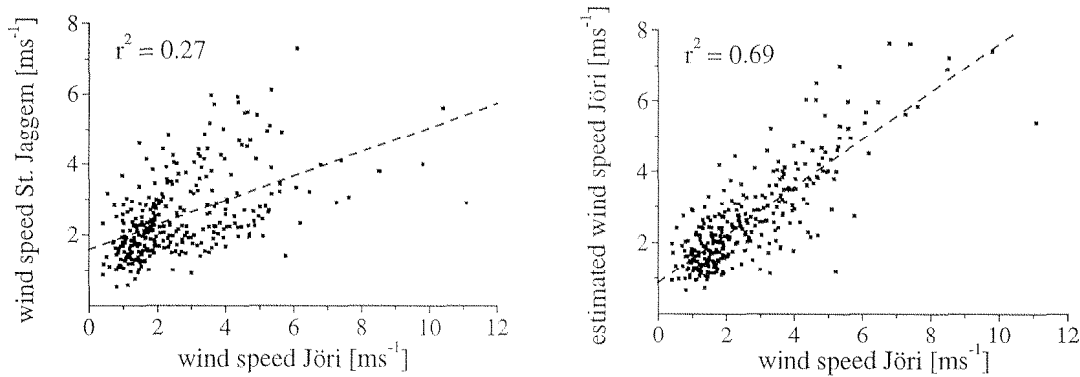


Figure 3.9: Left: Dependence between daily mean wind speeds at Jöri and St. Jaggem AWS. Right: Dependence between daily mean wind speed at Jöri AWS and estimated daily mean wind speed based on wind data from St. Jaggem. Both graphs include daily mean values from 1 January to 20 November 1998. The dashed line represents a least squared errors linear regression.

The results of this method can be seen in Figure 3.9. The left figure depicts the linear regression between the daily wind speed means of Jöri and St. Jaggem. The

regression in the right figure between the daily mean wind speed at Jöri and the estimated daily means at Jöri based on St. Jaggem data is clearly much stronger ($r^2 = 0.69$). Unfortunately this method does not work equally well for all AWS pairs. The Jöri wind speed was also estimated based on the Stillberg observations, but the resulting regression was less encouraging with an r^2 of 0.52.

Figure 3.10 shows the different effects of the mountain and valley winds on the AWS at Lake VII and III in the Jöri catchment. For every hour the data were averaged for September 1997, which was an unusually warm month with clearly above average global radiation and only 3 days with rain. It is visible that during the night wind speed is lower at Lake VII. This is possibly due to the cold air from the glacier increasing wind speed at Lake III during the night. As the sun rises, wind speed at Lake VII AWS increases steadily up to a maximum value at 16:00 CET, while at the Lake III AWS the increase is much smaller and the maximum is reached at noon already. The large wind speed differences during daylight between the two AWS are due to the mountain-valley wind system. While at Lake VII, which is situated at a pass, the valley wind develops to its full strength, the AWS at Lake III is shielded from the valley wind by a small ridge to the north of the station. This is another example how wind speed can vary within a small area.

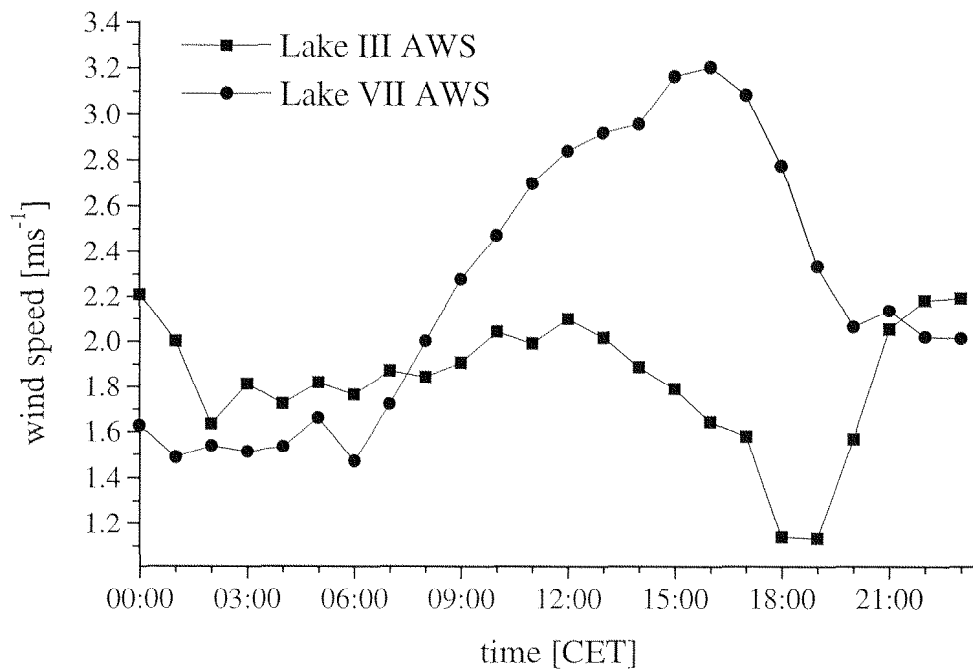


Figure 3.10: Hourly mean wind speed at Lakes III and VII for the month of September 1997.

3.6.3 Conclusions

The measurement of representative wind speed and direction is difficult if not impossible in complex terrain. Air flow is highly variable and heterogeneous within a small mountain catchment and therefore wind speeds measured are at the most representative for a lake adjacent to the wind gauge. For the present study of lake energy budgets, this is sufficient, but for distributed snow or evaporation models more information about air flow would have to be gathered. Wind speed is also heterogeneous on a water surface, leading to water temperature differences especially during the freezing phase (see chapter 6.2). Although daily mean wind speed at the Jöri site could be modeled using St. Jaggem data, this was only possible because data were available from the Jöri AWS over from 1996 to 1999. Without measurements, this model could not have been developed. It is therefore crucial to set up a wind gauge for at least several months at a lake where energy budget calculations are to be carried out. The effects of wind on the energy budget and the surface temperature of lakes are described in chapter 5.

3.7 Global Radiation

The radiant energy of the sun is by far the most important source of energy forcing atmospheric motions and many different processes in the atmosphere, at the earth's surface and in oceans and lakes (Plüss, 1997). Global radiation is the sum of direct and diffuse shortwave radiation, measured with a pyranometer. The amount of direct radiation reaching a horizontal plane at the earth's surface is a function of latitude, time of the year, cloud cover and constitution of the atmosphere. The latitude and the time of year determine the path length of the solar beam through the atmosphere and the cloud cover and constitution of the atmosphere determine the attenuation coefficient (Kondratyev, 1973). The main cause of diffuse radiation are clouds. On overcast days, global radiation may be entirely diffuse and almost isotropic (Plüss, 1997). Diffuse radiation in complex terrain like in the Jöri catchment also has a component originating from the reflection at the surrounding topography.

3.7.1 Measurement errors

The pyranometer at the Jöri AWS was neither heated nor ventilated. Snow covered the sensor when it fell under calm conditions. Because of the radiative cooling of the sensor, wet snow falling at temperatures around 0° C can freeze at the instrument surface. This can lead to erroneous measurements of up to two weeks after heavy snowfall (e.g. in November 1996). The days with snow on the sensors were evaluated comparing the daily average global radiation at Jöri with data from Weissfluhjoch, also considering snow data. Depending on the application of the radiation data, the erroneous

values were either deleted or estimated from the values at Weissfluhjoch and Stillberg on a daily basis. For the year 1997 radiation data from Weissfluhjoch was also available from the World Radiation Center (WRC) in Davos. WRC is a world leading calibrator of radiation instruments and therefore their measurements are expected to exhibit the least errors at all times. At Weissfluhjoch the sensors from SMI and WRC are in fact only a few meters apart, so they are expected to measure similar values. This was not true for some days in 1997. On 48 days during that year, the differences in daily means exceeded $10 \text{ W}\cdot\text{m}^{-2}$. Most of these deviations were negative, meaning that the SMI sensor measured less radiation than WRC sensor. This is the result of snowfall which affected the SMI sensor more severely. The effects were comparable to the ones observed for the Jöri sensor, although the SMI-sensor was heated. Global radiation measurements are delicate and they can be erroneous on days with snowfall which are quite frequent in the high mountains. At Weissfluhjoch, snowfall is recorded on more than 100 days every year (Ammann, 1997).

3.7.2 Regional heterogeneity of global radiation

Global radiation heterogeneity has various sources, which can be distinguished into three categories of processes: (1) absorption and scattering by aerosols, water vapor, and other gases in the atmosphere; (2) multiple reflections between the atmosphere and by the surrounding terrain, as well as horizon obstruction; and (3) absorption and scattering by clouds (Greuell et al., 1997). Process (1) is assumed to have a comparably small effect. In summer heterogeneous cloud cover and therefore heterogeneous global radiation is common in mountainous regions due to the variable convection at mountain sides. In the rugged terrain of the Swiss Alps, horizon obstruction is an important factor, mainly in winter, while reflection by the surrounding terrain is important in spring, when global radiation is high and snow still covers most of the ground. Two clear sky days, 2 April 1997 and 9 September 1997, were compared. Both days had about the same sunshine duration, being almost equidistant from the summer solstice. On 2 April the whole catchment was snow-covered, while on 9 September almost all snow had melted away. On the latter day, the daily average radiation was $268 \text{ W}\cdot\text{m}^{-2}$, while on 2 April the radiation reflected at the snow surface in the catchment enhanced the average global radiation to $289 \text{ W}\cdot\text{m}^{-2}$. Also due to radiation scattering at surrounding terrain, an exceptionally high daily mean global radiation value of $409 \text{ W}\cdot\text{m}^{-2}$ was observed on 23 June 1999. Daily mean global radiation can never reach a value that high at a lowland site at the same latitude.

To evaluate possible systematic differences in global radiation between two stations, a linear regression analysis was performed with 1997 global radiation data from the Jöri AWS and each of the other data sets measured in the vicinity of or within

the Jöri catchment (Weissfluhjoch, Research Field SLF, Stillberg, Jöri Lake VII, Jöri Lake X). The Jöri AWS data were also compared with global radiation observations at Payerne, a lowland site more than 200 km from the Jöri catchment. Mean bias error (MBE) and root mean square error (RMSE) with respect to the Jöri AWS data were calculated for each of the measurement sites, once for the complete data sets, and also for four three-month periods of the year 1997 (January - March, April - June, July - September, October - December). The values of MBE are attributed to the processes which change only slowly over the course of a year, such as terrain shading and reflection. On the other hand, RMSE is attributed to the highly variable processes affecting the global radiation, such as varying cloud cover. The latter can also affect MBE, when the cloud cover distribution is permanently different at one site, compared to the Jöri site. This may be the case, if a site is at lower or higher altitude being below the cloud cover frequently, when the Jöri site is not or vice versa.

| | WFJ | Stillberg | Research Field | Payerne | Lake VII | Lake X |
|-----------|-------|-----------|----------------|---------|----------|--------|
| RMSE all | 24.6 | 33.5 | 26.5 | 58.2 | n.a. | n.a. |
| RMSE 1 | 13.8 | 26.6 | 16.2 | 37.4 | n.a. | n.a. |
| RMSE 2 | 31.1 | 33.7 | 33.3 | 67.2 | n.a. | n.a. |
| RMSE 3 | 30.7 | 39.2 | 34.3 | 69.7 | 18.0 | 23.4 |
| RMSE 4 | 14.8 | 27.4 | 15.0 | 39.2 | n.a. | n.a. |
| MBE all | 7.2 | -25.8 | 6.9 | -11.9 | n.a. | n.a. |
| MBE 1 | 6.9 | -38.8 | 8.0 | -35.1 | n.a. | n.a. |
| MBE 2 | 4.6 | -20.8 | 4.8 | -4.6 | n.a. | n.a. |
| MBE 3 | 6.7 | -16.3 | 5.7 | 14.3 | 1.0 | -14.7 |
| MBE 4 | 10.1 | -28.0 | 8.3 | -21.0 | n.a. | n.a. |
| r^2 all | 0.924 | 0.811 | 0.912 | 0.539 | n.a. | n.a. |
| r^2 1 | 0.935 | 0.648 | 0.913 | 0.212 | n.a. | n.a. |
| r^2 2 | 0.834 | 0.781 | 0.809 | 0.205 | n.a. | n.a. |
| r^2 3 | 0.823 | 0.697 | 0.772 | 0.142 | 0.934 | 0.893 |
| r^2 4 | 0.856 | 0.580 | 0.850 | 0.337 | n.a. | n.a. |

Table 3.4: Statistical values of the regression of daily mean global radiation with Jöri AWS for the year 1997. "all" refers to the regression including all values of 1997, while the numbers indicate the quarter of the year of which data were used (e.g. 1 corresponds to the month from January to March). RMSE is the root mean square error and MBE is the mean bias error, r^2 is the square of the correlation coefficient. (n. a. = data not available)

The RMSE values are generally lower in the first and last quarter of the year than in the middle of the year (Table 3.4). This is due to the lower values of global

radiation in winter explicitly implicating lower variability. Therefore RMSE is not comparable between the different regression periods. For comparisons of the different regression periods, the values of r^2 are more suitable. As RMSE values from the third quarter of the year show, global radiation measurements of stations inside the Jöri catchment are more closely related to the values of Jöri AWS. Most of the variability of MBE of all sites and periods can be attributed to horizon obstruction. This is best visible in the Stillberg and Lake X MBEs. Both sites have a high skyline towards the west, shielding late afternoon sunlight even in summer. Shielding is practically non-existent at Weissfluhjoch, due to its mountain top location.

The comparison with the Payerne site shows extremely variable MBEs over the year. This is of course due to Payerne being below the inversion layer in the winter and due to the limited convective activity in summer at that site. The regression with the Payerne data in the third quarter is statistically not significant ($r^2=0.142$, $p<0.05$).

RMSEs and r^2 indicate that from October to March global radiation values for the Jöri site could be substituted with observations from Weissfluhjoch, providing a correction factor can be applied for the additional shading at the Jöri site. Differences in these months were always below $35 \text{ W}\cdot\text{m}^{-2}$ in 1997. In the summer these differences sometimes exceed $100 \text{ W}\cdot\text{m}^{-2}$, due to heterogeneous cloud cover. The high r^2 for the data within the Jöri catchment lead to the conclusion that single global radiation measurements made locally are representative for a small catchment, if the horizon obstructions can be accounted for.

3.7.3 Calculation of global radiation

The daily mean clear sky radiation at any given point can be calculated if the topographic shading is known. Also the radiation input perpendicular to the surface can be calculated, if the exposition and the slope of the point in question are known. All these variables were calculated for the whole Jöri catchment using a DEM.

The dependence of the flux of total radiation R_{SW} and the zenith angle of the sun ϑ_0 can be analytically represented by the following formula (Kondratyev, 1973):

$$R_{SW} = \frac{S_0 (\cos \vartheta_0)^2}{\cos \vartheta_0 + f}, \quad (3.5)$$

where S_0 is the solar constant, f is a parameter whose magnitude depends on the properties of the atmosphere and ϑ_0 is the zenith angle of the sun. The solar constant is not actually a constant, but varies by about 3% around its average of $1368 \text{ W}\cdot\text{m}^{-2}$. The parameter f was approximated according to the values presented by Kondratyev (1973):

$$f = 0.02 + 0.065 \cdot \left(\sin \left[\frac{(day-15) \cdot 2 \cdot \pi}{365} - \frac{\pi}{2} \right] + 1 \right), \quad (3.6)$$

where *day* is the julian day of the year. According to Plüss (1997) it was assumed that diffuse radiation accounted for 15% of global radiation under clear sky conditions. Therefore, if a point in the catchment was shaded by terrain, the global radiation input was set to be 15% of the maximum possible clear sky radiation.

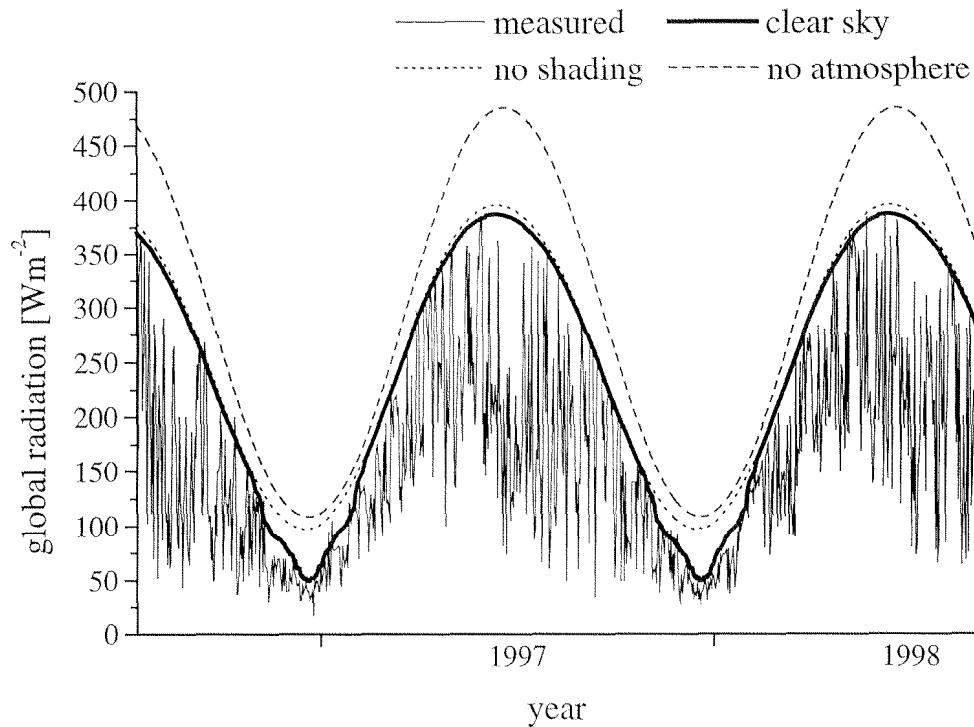


Figure 3.11: Observed global radiation at the Jöri AWS from 15 July 1996 to 31 August 1998 together with the calculated clear sky radiation, the possible global radiation without horizon obstruction and the possible global radiation without atmosphere.

In Figure 3.11 the calculated clear sky global radiation at the Jöri AWS is compared with the actually measured one. Additionally, the graphs of clear sky radiation without terrain shading and without atmosphere are displayed. The measured global radiation fluctuates from day to day owing to variable cloud conditions. On cloudless days, the measured global radiation reaches the calculated one. The reflections of radiation at the surrounding mountains were not parameterized, therefore the measured values can be higher than the calculated ones on rare occasions. Also due to these terrain reflections, the minimum radiation values in the first half of each year are clearly larger than in the second half. The largest shading occurs in the winter around the winter solstice, when sun elevation is low. The effects of shading are smallest when

the sun rises above and sets below the terrain horizon at a low elevation angle. This is the case in February and October, when the obstruction angle is at its lowest yearly value at sunrise and sunset. The attenuation of radiation by the atmosphere is more or less linearly correlated to the incoming global radiation, being proportionally higher in the summer, when water content in the atmosphere is enhanced (Kondratyev, 1973).

Cloudless skies are relatively sparse in mountain regions, therefore the calculated clear-sky radiation cannot be applied to all points in the catchment frequently. In 1997 a clearness index K_0 was calculated for the Jöri AWS. In contrast with Plüss (1997) or Aubinet (1994), we used K_0 as the ratio of measured global radiation H_{meas} to H_{max} , the calculated clear sky global radiation:

$$K_0 = H_{meas} / H_{max} \quad (3.7)$$

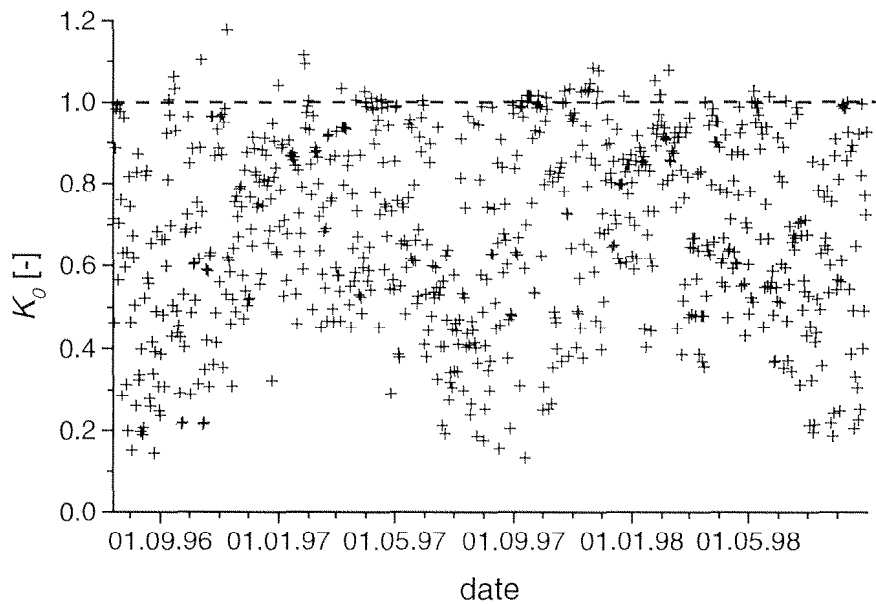


Figure 3.12: Clearness index K_0 for the period from 15 July 1996 to 31 August 1998.

On 68 days in 1997 the ratio K_0 was above 0.95, indicating clear days with little or no cloud cover. Of these 68 days, only 4 days were recorded during the tree summer months. To calculate the global radiation for all days and at each point, a model was developed which included the clearness index K_0 . The value of K_0 from July 1996 to August 1998 is displayed in Figure 3.12. Just like in Figure 3.11, the minimum K_0 during overcast days is clearly higher during the snow-cover period from November through June, when minimum values are between 0.3 and 0.45. After melting of the snow in the catchment, K_0 occasionally drops to values as low as 0.15. The yearly mean of K_0 during overcast conditions was set to 0.3. On days when this minimum was

reached, global radiation was assumed to be homogeneous over the whole catchment, disregarding shading effects and expositions. Therefore, values measured at the Jöri AWS were considered representative for the whole catchment on overcast days.

On clear sky days, when K_0 was 1 or larger, the effects of terrain obstruction for each point in the catchment were expected to be largest. The differences between the measured and calculated global radiation were assumed to be proportional to the clearness index K_0 . This assumption agrees well with the data from Stüve (1988) and Plüss (1997). Of course this is only valid under homogeneous cloud conditions. For daily mean values this prerequisite is probably fulfilled. The errors become large only if cloud cover is regularly different at two different sites. Global radiation calculations for each point in the catchment H_{calc}^P is as follows:

$$H_{calc}^P = 1.43 \cdot (K_0 - 0.3) \cdot (H_{max}^P - H_{max}^{AWS}) + H_{meas}, \quad (3.8)$$

where H_{max}^P is the clear sky radiation at the point where global radiation is to be calculated and H_{max}^{AWS} is the clear sky radiation at the Jöri AWS. The formula was applied to the data from the Jöri catchment from 25 June to 16 October 1997. The global radiation at the Jöri AWS was used for the calculation of the global radiation at the AWSs at Lake VII and X. The measurements recorded at the AWSs of Lakes VII and X were then compared to the calculated values for these AWS, as well as to the measurements made at the Jöri AWS. Linear regressions calculated between all measured and calculated global radiation data sets from 25 June to 16 October 1997 all yielded a $p < 0.0001$. The first value in each parenthesis of Table 3.5 represents the slope of the regression, which was chosen to run through zero. The second value inside the parenthesis is r^2 , the square of the correlation coefficient. Only the bold values will be discussed here, since the other regressions are not meaningful.

| all $p < 0.0001$ | Lake VII meas | Lake X meas | Lake VII calc | Lake X calc |
|------------------|-----------------------|-----------------------|-----------------------|-----------------------|
| Lake III meas | (0.996, 0.941) | (0.916, 0.899) | (0.987, 0.996) | (0.927, 0.988) |
| Lake VII meas | (1,1) | (0.916, 0.889) | (0.984, 0.953) | (0.925, 0.959) |
| Lake X meas | - | (1,1) | (1.064, 0.924) | (1.001, 0.936) |
| Lake VII calc | - | - | (1,1) | (0.939, 0.996) |
| Lake X calc | - | - | - | (1,1) |

Table 3.5: Slope and r^2 of the linear regression between pairs measured (meas) and calculated (calc) data from the Jöri AWS at Lake III, Lake VII AWS and Lake X AWS. The first value in parenthesis is the slope, while the second one is r^2 .

The correlation r^2 between the measured global radiation is quite high for all three possible pairs, being from 0.889 to 0.941. Especially Lake III and Lake VII values are similar, with a slope of 0.996 and an r^2 of 0.941. As expected, the linear regression of the recorded data at Lake X yields a higher correlation with the calculated Lake X data (0.936) than with the Lake III data (0.899). The slope is also much better, being almost exactly 1, compared to 0.916 with the Lake III data.

The model yields a better correlation for Lake VII than for Lake X. However, the use of the model is better justified at Lake X, than at Lake VII. One could just as well use the measurements made at Lake III to describe the global radiation input at Lake VII. At Lake X, this procedure would lead to much larger errors. At sites with a high skyline and much shading, like at Lake X, the application of the model is highly justified. In a sense this is obvious, because assuming homogeneous cloud distribution, shading is the only effect leading to differences in global radiation.

Problems in the application of the model could arise, if the station where global radiation is measured were subject to almost permanent shading. Under these conditions, the global radiation differences between cloudless and overcast days are small or can even be negative, i.e. the global radiation is higher during overcast conditions. This was observed frequently at the AWS at Stillberg during the winter. To avoid this problem, the global radiation measurement instruments would have to be placed at a site, where shading of sunlight is small throughout the year.

3.7.4 Conclusions

At similar altitudes, global radiation in mountainous regions tends to be rather homogeneous over a rather large area. During the summer, the differences are higher than during winter due to the increased local cloud and thunderstorm activity in summer. The largest differences between the global radiation data from two AWSs at the same altitude and in the same climatic region are due to the horizon obstruction. The proposed model for the calculation of global radiation deals with these differences and yields accurate data for all possible locations nearby an AWS. If the horizon obstruction of a lake is known then the measurement of global radiation is not necessarily required since it can well be modeled with data from AWSs nearby.

3.8 Incoming longwave radiation

There are times when incoming longwave radiation assumes greater importance than solar radiation, such as when solar radiation fluxes are zero (at night), or when it is reduced by heavy cloud cover (which simultaneously enhances atmospheric longwave radiation) and when the reflected portion of solar radiation is high as a result of high surface reflectances, such as produced by snow cover (Saunders and Bailey, 1997).

Since mountain environments generally are places where snow and clouds persist longer than they would otherwise, the importance of longwave radiation exchanges becomes readily apparent. The longwave radiation balance can vary substantially within rugged massifs like the Jöri catchment due to differing terrain temperatures and site view factors (Olyphant, 1986). Longwave radiation can be measured directly or indirectly with a pyrgeometer or a pyrradiometer, but these instruments are still quite expensive and delicate and are not used for routine weather measurements. In the majority of practical applications, sky radiation is estimated indirectly using air temperature measurements and cloud cover and sometimes also humidity (Aubinet, 1994).

3.8.1 Measurement errors and problems

Despite the limitations of a pyrgeometer, the longwave radiation is most precise when measured. At the Jöri AWS, a simple pyrgeometer with a viewing field of 150° was used. The restricted viewing field has the effect that all incoming radiation originating at angles of below 15° above the horizon were neglected. Thus, the longwave radiation enhancement by the rugged terrain around the measurement site was not registered. Net longwave radiation was also measured by the WRC at Weissfluhjoch with precise instruments. Because the accuracy of the Jöri sensor specified by the manufacturer is only $\pm 10\%$, the differences between the Jöri and the Weissfluhjoch data were not analyzed.

Complementary to the internal errors of the pyrgeometer, external effects can further falsify the measurements. These effects are mostly the same as for the global radiation measurements, involving snow cover on the sensor. Although the pyrgeometer at the Jöri AWS was heated, it usually took a while until a snow cover had melted from the sensor. The problem of the snow cover is enhanced because the sensor is flat in contrast to the dome shaped pyranometer. Aside from snow cover, a water film also falsifies the measurements of incoming longwave radiation.

The effects of rugged terrain on incoming longwave radiation were not evaluated for the Jöri catchment. Plüss (1997) calculated the additional longwave irradiance for varying elevation angles of terrain. The enhancement was less than $10 \text{ W}\cdot\text{m}^{-2}$ for all points where the mean elevation angle of the surrounding terrain is less than 15° . On only 5 % of the sites with less than 10° surface inclination, the horizon obstruction is above 15° elevation in the Jöri catchment. Therefore the effects of the additional irradiance are assumed to be small for the majority of the flat terrain and therefore also for the lakes. According to Plüss (1997) these effects may be larger for mountain slopes than for valley floors. However, the longwave radiation budget of steep mountain slopes is not of relevance in the study of the Jöri lakes.

3.8.2 An improved method for calculating incoming longwave radiation

The basic equation for most longwave radiation models is the Stefan-Boltzmann Law, which relates longwave radiation flux density (L) to the absolute temperature (T) and the emissivity ε of the emitting object, such that

$$L = \varepsilon \cdot \sigma \cdot T^4, \quad (3.9)$$

where σ is the Stefan-Boltzmann constant. Application of this equation to the incoming longwave radiation at the earth's surface requires some modifications (Saunders and Bailey, 1997). The difficulties are to determine the temperature T_a and the emissivity ε_a of the atmosphere. Several authors (Brutsaert, 1975; Idso and Jackson, 1969; Konzelmann et al., 1994; Swinbank, 1963) have tried to find empirical relations between an effective emissivity for the atmosphere and screen-level data, such as air temperature and vapor pressure, including cloud cover. The problem of these formulae is that they usually only yield good results for the data sets that the formula was calibrated on. Furthermore, these models depend strongly on the cloud cover, a parameter whose measurement can hardly be achieved objectively and, in particular, cannot be registered automatically. Aubinet (1994) introduced a model that avoided these problems by substituting the cloud cover by global radiation measurements.

For this study, Aubinet's approach was modified. With the improved method, daily longwave radiation can be calculated if air temperature, relative humidity and global radiation are measured and if there is an estimate or a calculation of clear sky global radiation for each day of the year.

The basic concept of this method is that daily global radiation is an indicator of daily mean cloud cover. Since longwave radiation is highly dependent on cloud cover, it is obvious that there is also a dependence between longwave radiation and global radiation. The new method was developed with high accuracy data from the WRC at the measuring sites of Weissfluhjoch (2693 m a.s.l.), Research Field SLF (2544 m a.s.l.) and Payerne (490 m a.s.l.) in the year 1997 (Froehlich et al., 1998). Data from different altitudes were used to make the model more realistic and better applicable to various data sets.

In a first step the emission temperatures of the sky were calculated from the actually measured longwave radiation R_{LW}^{meas} according to the Stefan-Boltzmann Law. Subsequently, the difference T_{diff} between the recorded air temperature T_a and the sky temperature was calculated.

$$T_{diff} = \sqrt[4]{\frac{R_{LW}^{meas}}{5.67 \cdot 10^{-8}}} - T_a \quad (3.10)$$

The regression between T_{diff} and the clearness index K_0 yields a reasonable correlation ($r^2 = 0.58$, see Figure 3.13) for the data set used ($n = 1235$). The clearness index is the ratio of measured global radiation and calculated or estimated clear sky radiation (see equation 3.7). Clear sky global radiation can be calculated according to the methods outlined in chapter 3.7, using a digital elevation model or data from a clinometer at the measuring site. If neither is available, daily clear sky radiation has to be estimated based on previous measurements. It is important not to neglect possible shading in the estimation of the clear sky global radiation, otherwise the clearness index will always be too low during the winter, indicating cloud cover, when there is none.

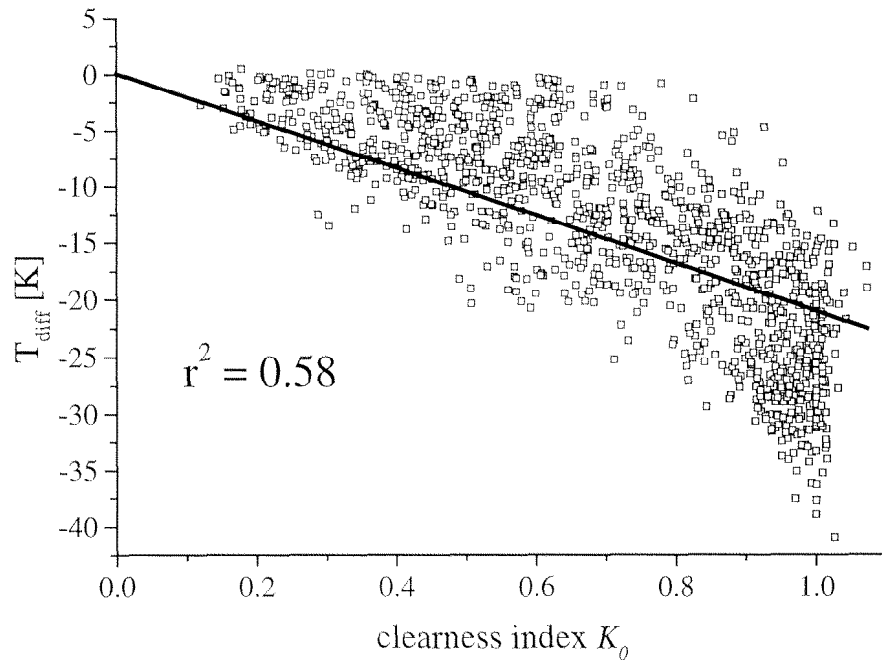


Figure 3.13: The difference between air temperature and emission temperature of the sky as a function of the clearness index K_0 . The line depicts the linear regression of the data.

Based on the linear regression of the whole data set one can propose to calculate R_{LW}^{calc} as:

$$R_{LW}^{calc} = (-21 \cdot K_0 + T_a)^4 \cdot \sigma \quad (3.11)$$

The essential of this formula is that the temperature difference T_{diff} for clear sky conditions ($K_0 = 1$) is expected to be -21 K, but as Figure 3.13 shows, it can be as much

as -40 K. For overcast conditions ($K_0 \sim 0.2 - 0.4$) T_{diff} will approach 0 K. Since the linear regression of the complete data set between R_{LW}^{calc} and R_{LW}^{meas} does not yield a high r^2 for values calculated with this formula ($r^2=0.68$), a correction factor introducing measurements of relative humidity was applied. When correlating relative humidity with the difference between R_{LW}^{calc} and R_{LW}^{meas} , it can be seen, that for clear sky conditions T_{diff} can be much higher than -21 K, especially at times when low relative humidity prevails. This can be observed frequently in high mountains. In fact, T_{diff} can be as high as 41 K, which is equivalent to an atmospheric emissivity ε_a of 0.51, a value which is not supported by many previous models. This was observed on a cloudless day when mean relative humidity was at 12 %. The correction factor including relative humidity was optimized for best regression. The final model for the calculation of incoming longwave radiation is therefore proposed as follows:

$$R_{LW}^{calc} = (-21 \cdot K_0 + T_a)^4 \cdot \sigma + 0.84 \cdot (rh - 68) \quad (3.12)$$

The emission temperature of the sky is rarely larger than measured screen air temperature. For this reason, the sky temperature was set to be equal to the screen air temperature, when sky temperature was calculated to be higher than screen temperature. Atmospheric emissivity ε_a would then take the value of 1.

3.8.3 Results

R_{LW}^{calc} calculated with the new method reached an r^2 of almost 0.90 for the complete WRC data set, including the sites of Weissfluhjoch, Research Field SLF and Payerne. With the same data set, three other models were tested (Table 3.6). The Idso and Jackson model (1969) is based on cloud cover n and air temperature T_a alone, while the other two also incorporate water vapor pressure e_a .

The performance of all equations was evaluated for the complete data set and for the three measurement sites specifically. The mean bias error (MBE) and the root mean square error (RMSE) of the linear regression between measured and modeled values were calculated (Table 3.7).

| Author | Equation | Model Nr. |
|-----------------------------|----------------------------------------------------------------------------------------------------------------------------------------------------------------------------|-----------|
| this study | $R_{LW}^{calc} = (-21 \cdot K_0 + T_a)^4 \cdot \sigma + 0.84 \cdot (rh - 68)$ | 1 |
| Konzelmann et al. (1994) | $R_{LW}^{calc} = \left[\left(0.23 + 0.483 \cdot \left(\frac{e_a}{T_a} \right)^{\frac{1}{8}} \right) \cdot (1 - n^3) + 0.963 \cdot n^3 \right] \cdot \sigma \cdot T_a^4$ | 2 |
| Idso and Jackson (1969) | $R_{LW}^{calc} = (1 + 0.22 \cdot n^2) \cdot \left(1 - 0.261 \cdot e^{-7.77 \cdot 10^{-4} \cdot (T_a - 273.15)} \right) \cdot \sigma \cdot T_a^4$ | 3 |
| Brutsaert (1975) | $R_{LW}^{calc} = (1 + 0.22 \cdot n^2) \cdot 0.642 \cdot \left(\frac{e_a}{T_a} \right)^{\frac{1}{7}} \cdot \sigma \cdot T_a^4$ | 4 |

Table 3.6: Longwave radiation models according to several authors including the model introduced in this study. Abbreviations: Vapor pressure e_a , air temperature T_a , cloud cover n , clearness index K_0 , relative humidity rh , Stefan-Boltzmann constant σ .

| Model Nr. | MBE all | MBE RF | MBE WFJ | MBE PAY | RMSE all | RMSE RF | RMSE WFJ | RMSE PAY | r2 all |
|--------------|---------------|-----------|------------|------------|--------------|------------|-------------|-------------|--------------|
| 1 | -0.48 | -0.92 | 4.29 | -4.59 | 14.82 | 15.02 | 14.22 | 13.70 | 0.899 |
| 2 | 6.32 | 6.11 | 10.45 | 2.51 | 15.11 | 15.75 | 16.03 | 11.83 | 0.880 |
| 3 | -0.32 | 2.76 | 8.06 | -13.13 | 21.48 | 21.32 | 22.83 | 12.82 | 0.606 |
| 4 | -12.19 | -16.94 | -13.57 | -3.90 | 20.95 | 20.17 | 20.00 | 20.50 | 0.847 |

Table 3.7: Mean bias error (MBE) and root mean square error (RMSE) of the longwave radiation data set for all models. The values were calculated for the complete data set (all) and for each AWS separately (RF - Research Field SLF, WFJ - Weissfluhjoch, PAY - Payerne). The correlation r^2 was only calculated for the complete data set.

Overall, the new equation is superior to all the previous ones. The distribution about the 1:1 line in the regression of observed to calculated incoming longwave radiation is visibly smallest for model 1, closely followed by model 2 (Figure 3.14). Obviously, the mean bias error for model 1 is close to zero because the model is based on the data it was tested on. RMSE of equation 1 is lowest and r^2 is highest of all the models. Equation 2 also yields exceptional results. Konzelmann et al. (1994) presented this formula for daily mean longwave radiation based on measurements under arctic conditions. Equation 4 is of limited use under the conditions of the present data set. This

is not astonishing since Brutsaert developed equation 4 using only clear sky data. In fact, for days with a mean cloud cover of less than 0.1, equation 4 yields the best results, but since clear sky days are rare in the Swiss Alps, the equation's performance is limited. The performance of equation 3 is quite reasonable when taking into account that it does not include any water vapor data. When splitting the results up into the three different measurements sites, the lowland site of Payerne is best modeled with models 2 and 4. Especially equation 2 yields exceptionally low MBE and RMSE for the Payerne data set, whereas the performance of the new model is worse for the Payerne data than model 2.

Depending on the available measurements, the parameterization of incoming longwave radiation yields best results with either equation 1 or 2. The reason for this may be that both equations were proposed based on daily means, whereas the other two models were developed using hourly values. Also it would need further investigation as to whether model 1 is suitable for various lowland sites. The new model is superior to all the others at high altitudes and since global radiation is measured at several sites in the Swiss mountains, equation 1 is especially suitable for the parameterization of incoming longwave radiation in the Swiss Alps.

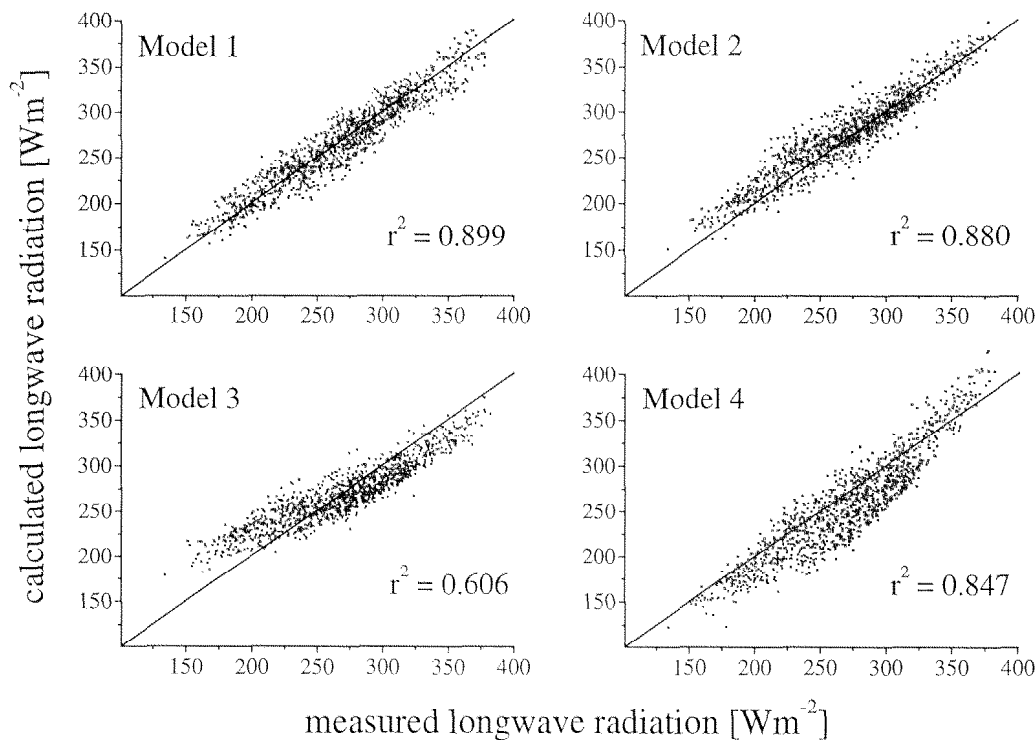


Figure 3.14: Scatterplot between calculated and measured longwave radiation of the complete data set ($n = 1235$) in 1997 for all four models. The 1:1 line is displayed in all graphs. Model numbers correspond to numbers in Table 3.6.

3.8.4 Limitations of the new model

Only daily means of incoming longwave radiation can be calculated with the new model. Better time resolutions would only be possible during daylight. Test runs with the new model adapted to hourly values showed promising results, but were not developed further. The new method yields better results in the summer months because of longer sunshine duration and therefore better indication of cloud cover. Cloud cover during the night is not represented. Consequently, long nights limit the performance of the equation. For measuring sites which experience intensive or complete terrain shading in winter, this method is not applicable because without direct sunlight, cloud cover information is not available. For this method it is also important that the global radiation measurements are precise and free of errors. Erroneous global radiation measurements can seriously affect the calculation of the clearness index and will therefore cause large errors in longwave calculation.

3.9 Precipitation

Precipitation in mountainous terrain is highly variable both in timing and in space (Running et al., 1987). Sevruk (1997) proposes that altitude is the main variable governing the spatial distribution of precipitation in the mountains. In the Swiss Alps, precipitation decreases from the prealpine mountains towards the inneralpine mountains (Gensler, 1978). The reason for this is the dominance of westerly and northerly air flows which tend to unload their water content on the first mountain ranges they reach. Aside from these larger scale precipitation differences, mean yearly precipitation values can vary enormously within a few km² owing to local morphology e.g. single mountains or specific valley shapes (Wahrenberger et al., 1997).

3.9.1 Measurement errors and problems

The exact measurement of precipitation in mountainous areas is virtually impossible. The values obtained are often erroneous and have to be corrected. Some of the systematic error sources and their magnitudes are listed in Table 3.8. Additional errors can be observed with unheated rain gauges as was done in the Jöri catchment due to the lack of sufficient energy. During snowfall the precipitation is not recorded at the time the snow actually falls, but at the time the gauge is warm enough to melt the snow accumulated inside it.

| error source | +/- | effect of error |
|-----------------------------------------------------------------------------------------------------------------------|-----|----------------------------------------|
| Disturbance of the wind field induced by the rain gauge and therefore drifting away of the rain drops and snow flakes | - | 2 % - 10 % (rain) 10% - 50 % (snow) |
| Evaporation of rain from the inner walls of the rain gauge or sublimation of snow accumulated inside the rain gauge | - | 2 % - 5 % |
| Evaporation of the water remaining after emptying of the gauge | - | 1 % - 3 % |
| Water drops splashing out of the gauge | - | 1 % |
| Water drops splashing from the ground into the gauge | + | 2 % |

Table 3.8: *Precipitation measurement error sources and their possible magnitude (from Wahrenberger et al., 1997). The minus sign indicates a measurement deficiency.*

3.9.2 Comparison of precipitation data from different AWSs

It is difficult to compare precipitation values between two stations, if the data are not corrected. Corrections are usually applied to yearly or monthly means making it difficult to compare daily data. The only time when comparison of daily data is acceptable, is during summer, when precipitation falls as rain.

Between 21 July and 27 August 1997 daily mean temperatures were always above 0° C, indicating that all precipitation fell in the form of rain. Precipitation values from Weissfluhjoch, Stillberg and Jöri Lakes III, VII and X were compared (Table 3.9). The correlation of the linear regression generally decreases with distance. This is most likely due to the heterogeneous thunderstorm activity in summer. The relatively high r^2 between several stations with different total amount of precipitation for the observed period, indicate that there are systematic differences in precipitation which cannot be attributed to thunderstorm activity solely. It is not quite clear what led to the precipitation differences between the stations. Climatologic means indicate that precipitation amounts at Weissfluhjoch are generally higher than at Stillberg (Wahrenberger et al., 1997). Most of the large differences between the stations of Jöri Lake VII and X are likely to be related to systematic errors, since these two stations are only 2 km apart and both are situated at the bottom of the Jöri catchment. However, wind speeds are much higher at Lake VII, causing more precipitation to be blown over the gauge than at Lake X. Since Lake VII is shielded by a mountain towards the north, a systematically lower precipitation is possible compared to values at Lakes III and X.

| r^2 | WFJ | Stillberg | Jöri III | Jöri VII | Jöri X |
|---------------|-------|-----------|----------|----------|--------|
| WFJ | 1 | 0.57 | 0.70 | 0.62 | 0.53 |
| Stillberg | 0.57 | 1 | 0.63 | 0.71 | 0.65 |
| Jöri III | 0.70 | 0.63 | 1 | 0.86 | 0.93 |
| Jöri VII | 0.62 | 0.71 | 0.86 | 1 | 0.75 |
| rainfall [mm] | 229.5 | 146.7 | 178.1 | 155 | 191.4 |

Table 3.9: Correlation r^2 of the linear regression between different pairs of precipitation data between 21 July and 27 August 1997 and the corresponding total amount of measured rain for each AWS in that period. Snowfall was not observed during this time period. Forward and reversed comparison which give the same r^2 appear in the table.

For the comparison between Weissfluhjoch and Jöri the periods from 15 July to 21 August 1996 and 20 July to 11 September 1998 can be used because no snowfall was registered during these periods. The precipitation sum for these time periods at Jöri and Weissfluhjoch AWSs differ by less than 1 %. The same observation was made in the years 1961 through 1965, when a storage gauge was set up at the site of the Jöri AWS. Although the precipitation differences between Jöri and Weissfluhjoch can be up to 70 mm during a summer as was observed in 1961, it seems that the climatic averages are almost equal. Similar observations can be made for the periods from 1 October to 30 June in the years 1961 to 1965, when applying the correction factors from the literature (Sevruk, 1983). Winter precipitation at Jöri was less than 5 % off the values at Weissfluhjoch in the years 1961 to 1965. Several observations of snow height in the years 1997 to 1999 also indicate a high similarity of winter precipitation amounts. The mean precipitation amount for Weissfluhjoch from the years 1964 to 1993 is 1585 mm, which in the light of the previous assumptions can also be seen as the climatic precipitation amount for the Jöri AWS.

Snow height measurements were made before the starting of the snow melt on 29 April 1998 throughout the catchment. The variability of the height was large within just a few meters due to snow being displaced by wind forcing. Nevertheless, some indicators of varying snowfall rate within the catchment were found. Snow heights between Lake III and Lake X did not differ substantially, but towards the Jöri Glacier more snow accumulated. The snow heights measured on the glacier were 30 % to 50 % higher than in the valley. Part of this thicker snow cover can be attributed to earlier snow in the fall and decreased sublimation of snow due to lower global radiation.

3.9.3 Conclusions

Precipitation is generally difficult to measure in high mountain regions due to the frequent snowfall. The available data only allowed point comparisons. The complex distribution of precipitation inside the Jöri catchment or over a larger area around the catchment could not be evaluated. Comparisons between stations can only be carried out over period of one month or more. Comparisons of daily means are not feasible due to the large errors associated with precipitation measurements during storms and in winter. Even when including all available stations and correcting the data, the spatial distribution of precipitation is difficult to determine accurately because the use of exclusive valley positioning of gauges which is the common practice in the mountains can overestimate the precipitation on slopes. Also precipitation distribution studies are rather network specific than physically based, depending on the distribution of the rain gauges (Sevruk and Nevenic, 1998). In this particular case, the precipitation at Jöri could be approximated with data from Weissfluhjoch reasonably well. However, this is only a coincidence and the same relation cannot be used for other station pairs without rigorous data analysis.

3.10 General climatology of the Jöri AWS

Based on the comparisons made between data from the Jöri AWS and the AWSs outside the catchment, the mean climate at the Jöri AWS was evaluated. Mainly the data from Weissfluhjoch AWS was used to define the climate at Jöri because regular meteorological measurements have been made at Weissfluhjoch since 1947 (Ammann, 1997). Daily means of the observed meteorological values at the Jöri AWS are displayed in the appendix.

Yearly mean temperature at the Jöri AWS is -2.2°C . The warmest month is August, with a climatic mean of 6.0°C . The coldest month is February with a climatic mean of -10.4°C . The daily means range from below -30°C to about 17.5°C , with maximum air temperatures rarely exceeding 20°C .

Mean cloud cover is 0.65, with the lowest values when daily mean sun elevation is low from September to February. Mean monthly values are above 0.65 in the months from March through August. Therefore, clear days (cloud cover <0.15) are rare in spring and summer due to the increased convection. Due to the large water areas in the catchment and because the catchment is at the very end of the Jöri valley, fog is a common factor, especially during the open-water season.

Relative humidity tends to be low, when clouds are absent. Therefore, there is a positive correlation between cloud cover and relative humidity. Monthly mean values of relative humidity are generally around 80 % from March to August. The lowest monthly means are regularly recorded during January and February with values as low as 47 %

(February 1998). When high pressure systems are active during the winter, daily mean relative humidity can reach values as low as 10 %.

Due to the variable wind conditions, an estimation of mean yearly and monthly wind speeds is difficult. Mean yearly wind speed at the Jöri AWS is between $2.5 \text{ m}\cdot\text{s}^{-1}$ and $3 \text{ m}\cdot\text{s}^{-1}$. The mean monthly wind speeds are largely dominated by the frequency of southerly winds across the Alps because wind speeds are highest from that direction. Mean monthly wind speeds tend to be lowest during summer, with values below $2 \text{ m}\cdot\text{s}^{-1}$. This is due to the mostly missing southerly winds in summer and due to the increased roughness length, when the catchment is mostly free of snow.

Yearly mean precipitation is close to 1600 mm with large year to year variations. The minimum yearly precipitation with only slightly above 1000 mm was observed in 1972 and the maximum yearly precipitation with over 2000 mm was observed in 1982. Between 60 % and 70 % of the precipitation falls as snow. Precipitation events are generally more intensive during the summer month, when rain is associated with thunderstorm activity.

Due to the highly variable precipitation amounts, snow height is also different from year to year. The time of the build up of a permanent snow cover at the Jöri AWS was from early September to the end of November, and the melting of the snow cover ended between the end of May and mid August in the years from 1946 to 1999. Maximum snow height varies between 150 cm to 350 cm and is usually recorded sometime between the middle of March and the middle of May.

4 Effects of suspended erosion particles in lakes

4.1 Introduction

Below a certain water depth, photosynthetically active radiation (PAR) can become limiting for phototrophic growth of phytoplankton. Solar radiation diminishes with depth since its infrared energy is absorbed in the top centimeters of the water column by water itself and its short wavelength portion is scattered and absorbed by "yellow" (organic) substances, phytoplankton, and inorganic particles. Water and yellow substances absorb light, phytoplankton absorbs and scatters light, and inorganic particles mostly scatter light (Effler, 1985). Glacial lakes usually have high contents of suspended particles, little yellow substance and, due to the harsh conditions, only limited phytoplankton growth. Consequently, inorganic particles dominate the attenuation of light in lakes with glacial meltwater input (Koenings and Edmundson, 1991).

Erosion particles are the most important contribution to a summer-season sediment budget in a glaciated catchment (Warburton, 1990). In several Jöri Lakes a substantial amount of particles originates from the activity of the Jöri glacier. A glacier grinds the bedrock surface as it advances, producing "rock flour" which consists of tiny particles of a large range of size classes between less than 1 μm and up to 500 μm . The particles are flushed into the lakes with glacial meltwater. Jöri Lakes I, II, III and XIV are influenced by water from the Jöri glacier. The optical properties of Lake III, measured over the three year period 1996 to 1998, were found to be quite variable between the years and during each season. Since the variability of the particle concentration is due to processes involving the Jöri glacier; emphasis will be given in this chapter to studying the glacier's radiation budget which is the controlling component of its melting and freezing cycle (Plüss, 1997).

4.2 The Jöri glacier

The Jöri Glacier covers the southern tip of the Jöri catchment between altitudes of 2920 m a.s.l. to 2640 m a.s.l. The glacier had its last largest extent in 1850, when it covered about 35% (100 ha) of the catchment (Maisch, 1992). As calculated from the topographic map, it had a size of 40 ha in 1990. The area was reduced by approximately another 10% in the past decade, most probably due to the warmer climate. In 1850 it reached down to the altitudes of Lakes I to X. A subaquatic moraine can be seen close to the shore of Lake I, indicating that the glacier touched the lake at that time (Maisch, 1992). After 1850 the glacier continuously retreated to the small area which is left today.

4.2.1 Glacier melt

The amount of glacier ice melting determines the quantity of cold meltwater and the quantity of glacial erosion particles flowing into the lakes. The inflowing cold water affects the energy budget of a lake (see chapter 5). The particle input into the lakes affects the turbidity and thus the attenuation of light in a lake.

All temperate glaciers are completely snow-covered during the winter and during most of spring. The amount of snow melted away from the glacier every year largely influences its mass balance. A glacier which remains snow-covered perennially will gain mass, while a glacier without snow cover during the summer months will lose mass (Maisch, 1992). The amount of snow melted from the glacier can vary by 100% from year to year due to the changing meteorological conditions. Low snow height in spring and high temperatures in May, June and July favor an early melting of the snow on the Jöri glacier. The opposite is true for high snow heights and low summer temperatures. The melting of snow and glacier ice depends on the amount of energy input from the atmosphere. The energy exchange processes are virtually the same as for a lake (Stüve, 1988); the highest input of energy comes from solar radiation at this latitude, altitude and season (Plüss, 1997). Since energy budget calculations would be inexact and difficult without meteorological data from measurements right at the glacier, only the radiation input (global and longwave) was calculated in this study. Air temperature and humidity were not considered, the calculations thus represent only a crude indicator of the melting process.

Global radiation was calculated for the area of the glacier between June and October, based on the values recorded at the Jöri AWS. The description of the method can be found in chapter 3.7.3. Not all of the incoming global radiation is used for the melting of snow or ice, some or at times even most of it is reflected back to the atmosphere or to the surrounding terrain. The fraction reflected is known as albedo. Snow has a much higher albedo than glacier ice. The albedo for melting snow was set to be 0.6 (Conway et al., 1996), whereas for glacier ice it was set to be 0.3 (Oerlemans and Knap, 1998). The average albedo for the glacier was set according to the snow cover observed on the glacier. In 1997 the glacier was totally snow-covered until 15 August. By 10 September the glacier was 2/3 snow-free and stayed that way until it was fully snow-covered again by mid October. In 1998 the glacier remained snow-covered until 18 July; from then on the snow thawed quickly until 6 August, when the glacier was snow-free for about 80 % of its area. Snow covered the glacier again completely after 12 September 1998.

In addition to global radiation, longwave radiation was included in the radiation calculation. For reasons of simplicity it was assumed, that the longwave radiation input does neither depend on the surrounding horizon nor on the altitude. The sky-view factor

is 0.94 for the Jöri AWS and averages about 0.93 for the glacier. The average altitude of the glacier is about 220 m above the Jöri AWS. Assuming equal longwave radiation for glacier and AWS therefore yields errors of the order of $10 \text{ W}\cdot\text{m}^{-2}$. This is small enough to still be able to interpret the calculated radiation input.

The radiation input was calculated for 1997 and 1998, covering the period from 15 July to 15 October (Figure 4.1). The scale of the figure starts at $0 \text{ W}\cdot\text{m}^{-2}$ because negative values indicate that no melting took place. Radiation input during the observation period was 27 % higher in 1998 than in 1997. The early snowmelt in 1998 favored high radiation input due to the low albedo of the glacier throughout the month of August. During August 1998 the calculated radiation input was 81 % higher than in the same month in 1997. Another important factor is the radiation input peaks occurring between August 5 and 14 in 1998. The values of over $120 \text{ W}\cdot\text{m}^{-2}$ indicate a massive melting of glacier ice especially since these values are also coupled to high temperatures. No values above $90 \text{ W}\cdot\text{m}^{-2}$ were observed in 1997, while in 1998 the radiation input exceeded $90 \text{ W}\cdot\text{m}^{-2}$ on 27 days. This indicates that in 1998 the peak meltwater flow volumes were regularly higher than in 1997.

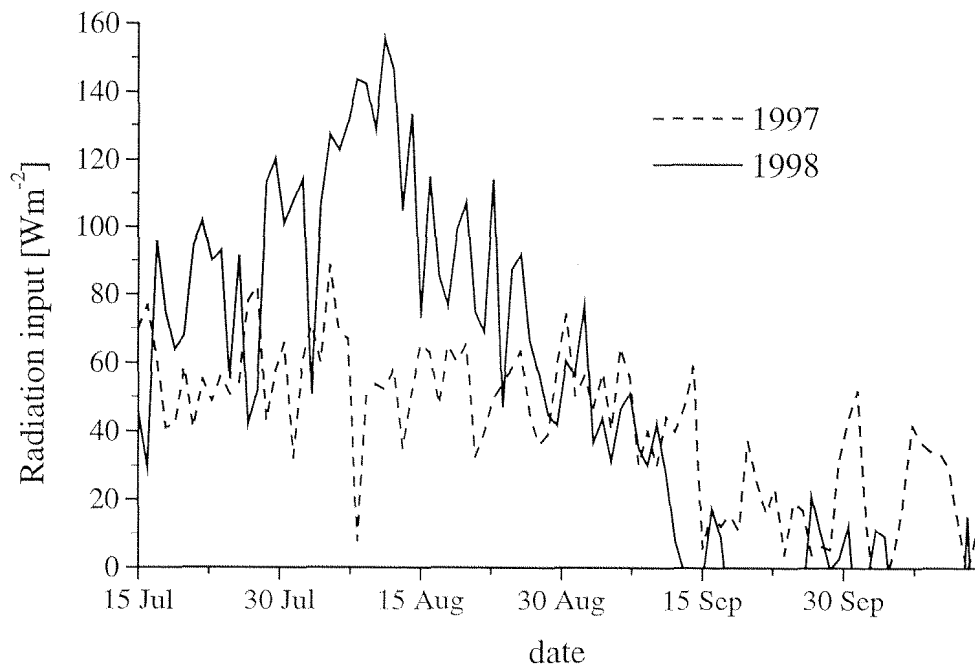


Figure 4.1: Calculated daily mean radiation (sum of longwave and global radiation) input to the glacier in years 1997 and 1998 from 15 July to 15 October.

4.2.2 Flow path of the glacier meltwater

It is of great importance to have information about the flow path of the glacial water because it determines which lakes are turbid from glacial erosion particles. All meltwater from the Jöri glacier flows into Lake XIV. Lake XIV is a small lake that was still covered by glacial ice 50 years ago. It is dammed by a moraine left by the glacier as it retreated. The glacier covers about 50 % of the catchment area of Lake XIV. Because of its small volume, its water body can be exchanged several times in one day. Lake XIV does not feed a surface stream, all water disappears into the moraine damming the lake. A visible outflow into the moraine is located at the northeastern end of the lake. The amount of water flowing into this gap in the rocks depends largely on the lake's surface level which in turn depends on the amount of inflow. The water level can be above the visible outflow on a day with large glacial meltwater inflow as was observed on August 6 and 11 in 1998. The level is also high during snow melt and after heavy precipitation events, although it was never observed to be as high as during the snow and ice melting period. The lake must be losing water through the sediment, since it is empty during the winter. Most of the water from Lake XIV flows to an outlet in the moraine between Lakes I and III and then continues its way through Lake II into Lake I. This was discovered with a tracer experiment applying Uranine to lake XIV on 20 July 1998. Most of the Uranine dye appeared in the moraine spring between Lakes I and III, but small amounts of Uranine (in the range of the detection limit) could be detected in the outflow water of Lake III. The inflow location into lake III could not be discovered so far. The color and the clay particle concentration of Lake III indicate, that some of its water input must be coming from particle rich Lake XIV. Judging from the throughflow velocity and the measured concentrations of Uranine at the moraine outlet, the water flow path must be close to the surface through unconsolidated sediment (Ullmann, 1998). Other lakes receiving glacier meltwater, which are not mentioned above are Lakes XV, XVI, XVIII, XIX and XX, with the latter three only receiving the tiniest fraction of erosion particles washed out from the glacier catchment.

4.3 Turbidity, albedo and color of Lake III

4.3.1 Measuring turbidity and albedo in Lake III

To assess the optical properties of a lake with glacial meltwater inflow, albedo and turbidity were measured at Lake III. Four sensors measuring Photosynthetically Active Radiation (PAR) were installed (Quantum Sensors, LI -COR). Two spherical sensors were attached to a pole on a float 15 m from the shore, measuring PAR at depths of 0.1 m and 1 m. Two flat, cosine corrected PAR sensors were used for albedo calculations. They were attached to the same pole above the water surface, one facing

towards the water surface and one facing skywards. PAR below the water surface is required for evaluating the light field for photosynthesis. For comparison a turbidity sensor was installed at the same site at a depth of 1 m. Measurements were recorded in 10-minute intervals. Additionally, point measurements of turbidity and radiation were taken several times per year in the middle of the lake at different depths and secchi depth was measured on several occasions. Turbidity (tb) was measured as absorbance at 660 nm using a photometer and the readings were converted into nephelometric turbidity units (NTU) by use of calibration solutes (Theis, 1999). The attenuation coefficient k in the top layer of the lake was calculated using the PAR measurements below the water surface:

$$k = \frac{-\ln\left(\frac{PAR_1}{PAR_2}\right)}{d_1 - d_2}, \quad (4.1)$$

where PAR_1 and PAR_2 is the PAR measured at depths of 1 m and 0.1 m respectively and d_1 , d_2 are the depths where the sensors were placed. The PAR attenuation is a function of wavelength of the incident radiation, color of the water, and amount and nature of suspended particles in the water. The attenuation coefficient in greater depths was calculated similarly at times when depth profiles for PAR measurements were available. The conversion of turbidity measurements into attenuation values k was done empirically with the help of the light-depth-profiles. The best fit led to the simple conversion of:

$$k = \frac{\ln(tb)}{3} \quad (4.2)$$

Attenuation and albedo values in this chapter were all measured using PAR measurements. PAR only covers wavelengths between 400 and 700 nm. The total energy included in global radiation is about 2.3 times greater than the PAR energy alone (Stefan et al., 1983). Problems arise when one tries to introduce the PAR-attenuation and the PAR-albedo to energy budget calculations, since attenuation and albedo are both wavelength dependent. Radiation with wavelengths above the PAR spectrum (>700 nm) tends to be absorbed by water in the top few centimeters of the water column. Table 4.1 shows the attenuation coefficients of pure water at different wavelengths. The transmittance values show that at wavelengths above 700 nm virtually all radiation is absorbed in the top meter or at wavelengths above $1 \mu\text{m}$ even in the top centimeters of the water column.

Since no 1-dimensional lake model was applied to Lake III, the-PAR attenuation values were not converted to fit the whole global radiation spectrum. The global radiation albedo, was needed for the energy budget calculations and the PAR measurements were therefore converted according to the method presented in chapter 4.3.4.

| wavelength [nm] | attenuation coefficient [m^{-1}] | transmittance [% m^{-1}] |
|--------------------|-----------------------------------------|--------------------------------|
| 400 | 0.043 | 0.958 |
| 500 | 0.036 | 0.964 |
| 600 | 0.186 | 0.830 |
| 700 | 0.500 | 0.605 |
| 800 | 2.05 | 0.128 |
| 1000 | 50 | <0.001 |
| 1500 | 3000 | <0.001 |

Table 4.1: Attenuation characteristics of pure water for different wavelengths (from Jerlov (1968)).

4.3.2 Color of glacial lakes

Lakes containing suspended erosion particles generally seem to be of a lighter color. The reason for this effect is the intense scattering of light by the particles in the lake. The physical processes are similar to those taking place in the atmosphere, except that the particle and molecule density is much larger in the lake which makes multiple scattering important. The color of lakes with glacial erosion particles is not the same over the year, it depends on the mass of particles flowing into the lake and the resuspension of sedimenting particles. As particle concentrations and scattering increase, the colors change from an intense blue to a milky blue to a light gray. Most of the high wavelength light is absorbed by the water molecules, while blue light is not attenuated significantly by pure water. Particle scattering coefficients are thought to be independent of wavelength (Jerlov, 1968). With higher particle concentrations the scattering is dominated by the particles; and the backscattered radiation becomes less and less dependent on wavelength. Therefore lake color will change from intense blue over light blue to light gray as particle concentrations increase. Particle concentrations in Lake III usually do increase over the ice-free period (see chapter 4.3.3). Turbidity from organisms may play an important role in lakes without suspended erosion particles, while in glacial lakes, that effect is usually overshadowed by the particles (Brown et al., 1992).

Lakes in the Jöri catchment without suspended erosion particles appear black, although they would be expected to look blue due to the lower attenuation and higher scattering coefficients for radiation of lower wavelengths. Since particles concentrations are rather small in these shallow lakes (VII, X, XII and XIII have depths between 4 m and 10 m), a significant portion of visible light is not attenuated or scattered before it reaches the lake bottom. The lakes are too shallow to appear blue because the light is not scattered back sufficiently and the portions reaching the ground are absorbed by the dark rocks or sediment.

4.3.3 Attenuation coefficients

Up until mid August, turbidity in the top meter was similar in the three years that the lakes were monitored (Figure 4.2). Turbidity remained almost constant throughout the summer of 1997 until the end of September. There was a sharp increase in turbidity at the end of August or beginning of September in the years 1996 and 1998, respectively. In September the particle concentration in the top meter of the lake was extremely variable from year to year. A PAR-attenuation coefficient of close to 2 m^{-1} calculated in mid September 1998 meant that more than 85 % of solar radiation was absorbed or scattered in the first meter of the water column. While the PAR-attenuation coefficient started to increase in October 1997, there was quite a steep drop in turbidity at the same time in 1996 and 1998.

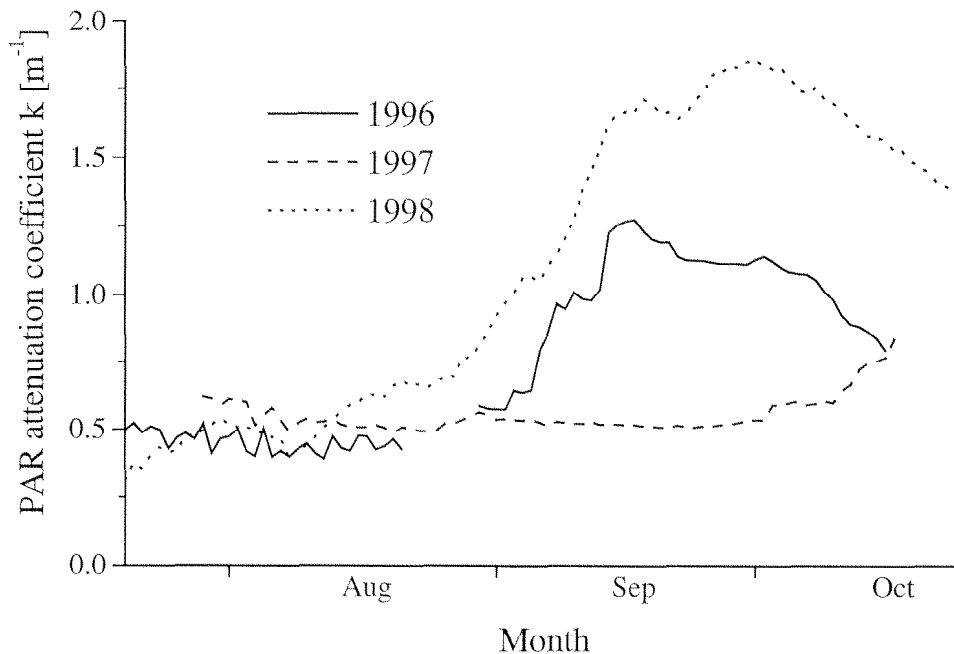


Figure 4.2: PAR attenuation coefficient in the top meter of Lake III measured 15 m from the shore (water depth 4 m) from 20 July to 20 October during the years 1996 to 1998.

A total of 19 coarse turbidity or light profiles were registered from 1996 to 1998. Based on these measurements, the attenuation coefficients were calculated for 5 m intervals. The results are presented in Figure 4.3. For visual purposes the measured points were connected. The attenuation coefficients in the profile are slightly different from those in the top meter. Turbidity in the top layer was measured close to the shore and may therefore be influenced by sediment resuspension, by wave action or by clear water entering the lake from the side during snowmelt or rain.

The differences in attenuation coefficients between the years are large, especially in August and later. In 1996 and 1998, the attenuation coefficient between 5 m and 15 m increased steeply in late July and August, especially in 1998. This indicates an input of large amounts of particles to the hypolimnion. The pattern of the changing attenuation coefficient in 1996 was similar to the one in 1998, but the maxima were not as high at all depths in 1996. Also in the years 1996 and 1998, turbidity seemed to increase later in the top 5 meters than in the hypolimnion. This is most pronounced in 1996 when the increase of turbidity in the top 5 m coincides with a decrease between 5 m and 10 m. A totally different pattern was observed in 1997. The turbidity decreased over the summer in the top 10 m. Only at depths between 10 m and 15 m there was a small increase in turbidity. Therefore the input of particles in 1997 was much less than in the other two years, and it was only observed in the hypolimnion.

There are three reasons for the higher particle concentration in the hypolimnion. First of all, the particle-loaded water reaches Lake III through a subsurface inflow, thereby entering the hypolimnion directly and it stays there as long as the lake remains thermally stratified. Secondly, since particle-rich meltwater is cold (1°C - 7°C) and carries loads of suspended erosion particles, it has a higher density than the warmer surface water. Water entering the lake is heavier than the water above it and it will therefore flow to depths of density equilibrium. Thirdly, since particles have different settling velocities depending on their weight, size, form and density, the particle concentration is usually higher in greater depths. The particles drop out of the epilimnion quickly, while it takes some time until they have settled through the hypolimnion. In conclusion, the particle distribution in a lake depends on the density of the inflowing water, the settling velocity determined by the size of the particles and the mixing processes in a lake. The effect of the latter is clearly visible in 1996, when the attenuation coefficient remained low in the top 5 m until mid August, while there was a sharp increase below 5 m. After mid August the picture reversed due to the mixing of the water column which led to a homogeneous particle distribution. Before ice builds, the lake is usually thoroughly mixed which leads to uniform turbidity at all depths. This was observed in 1996 in 1998 (Figure 4.3). In 1997 the last turbidity profile was taken before the lake was completely mixed. The turbidity just before the freeze-over may be

uniform, but it may not be at its highest level at that time. The reason for this is, that after mid September, the radiation flux to the glacier becomes less relevant. The particle input into any lake in the catchment will then be small. In the meantime the particles already in the lake will start to settle, decreasing the particle concentration steadily. Rain and snow meltwater will dilute the surface water and decrease its turbidity.

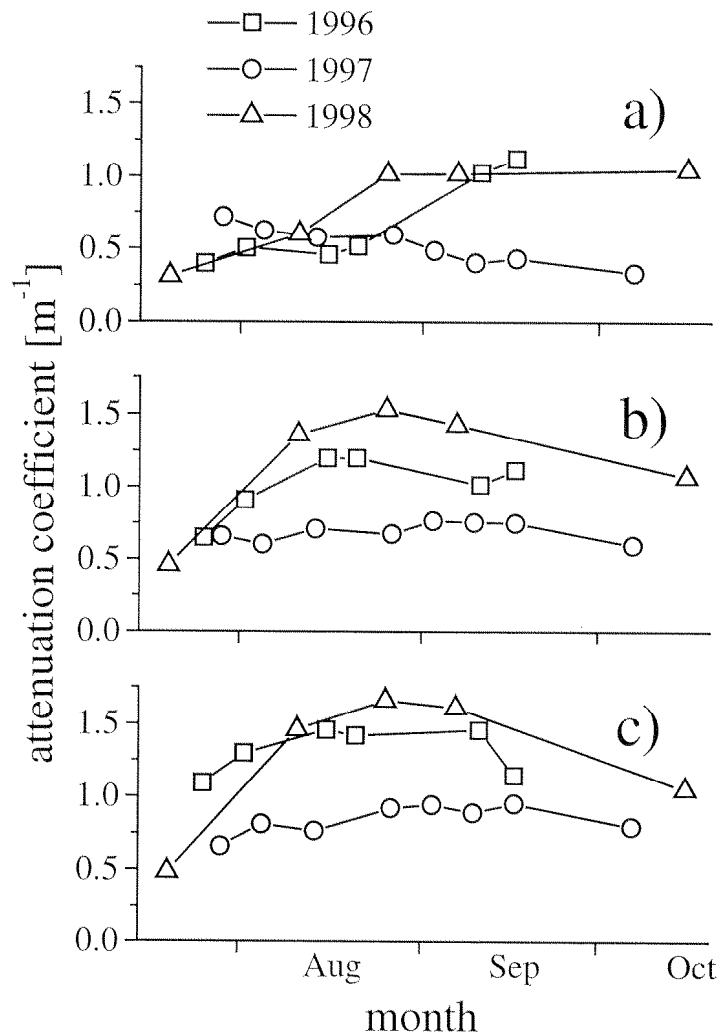


Figure 4.3: Mean PAR attenuation coefficients of three different layers in Lake III from 15 July to 15 October of the years 1996 to 1998. Depth layers: a) 0 m - 5 m, b) 5 m - 10 m, c) 10 m - 15 m. For visual purposes the measured points were connected. However values between the points are not known and cannot be linearly interpolated.

4.3.4 Albedo values

The PAR-albedo of Lake III was set as the fraction of the PAR being reflected by the water surface. Most of the light recorded by the PAR-sensor pointed at the water surface is reflected from below the surface by particles which cause multiple scattering.

Only a smaller fraction is reflected by the water surface itself. The lowest PAR-albedo of Lake III was found to be 0.11 right after ice melt in 1998. The values of 1996 were the only ones available over a wider time span (18 July to 17 September). They showed PAR-albedos between 0.12 and 0.27. It was found that PAR-albedo and the attenuation coefficient k in the top layer were correlated well during this time ($r^2 = 0.94$, $p < 0.0001$) (Figure 4.4). It is obvious that this high correlation is due to the varying concentration of glacial particles changing both albedo and attenuation coefficient similarly. This relationship was used to calculate PAR-albedo when only the attenuation coefficient was known and vice versa. The highest PAR-attenuation coefficient measured (1.85 m^{-1}) on October 1, 1998 would have resulted in a PAR-albedo of 0.32.

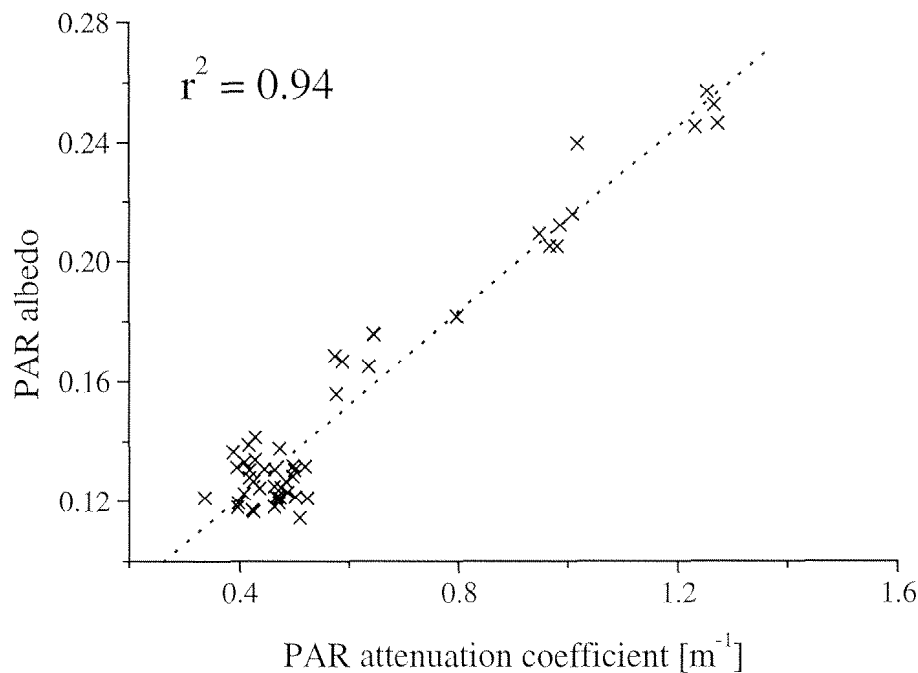


Figure 4.4: Linear regression between PAR albedo and PAR attenuation coefficient of Lake III for the time from 18 July to 17 September 1996.

The global radiation albedo is lower than the PAR-albedo due to the increased attenuation and decreased scattering at wavelengths above PAR. For the estimation of the global radiation albedo it was assumed that at wavelengths above 800 nm radiation is completely absorbed by water and nothing is scattered back. As values in Table 4.1 show, this assumption is reasonable. About 50% of global radiation at the earth's surface has wavelengths above 800 nm (Kondratyev, 1973). The observed PAR albedo was split up in two components. The first one was the PAR portion reflected at the water surface, the second one the upwelling light stemming from multiple scattering below the surface. The latter is most dependent on particle concentration while the first changes with

zenith angle and is largely wavelength independent. Mean surface reflectivity is lowest in June where it was set to be 0.06, while in October, just before freeze-over, higher zenith angles cause a higher mean surface reflectivity of about 0.09 (Kondratyev, 1973). All measured PAR values in Lake III in excess of the surface reflectivity were attributed to variations in particle concentration. According to the assumption above, 50 % of global radiation does not add to these excess values. Therefore, in order to get global radiation albedo a_T , the excess values a_{PAR} were multiplied by 0.5 and the resulting values added to the surface reflectivity a_S :

$$a_T = a_S + 0.5 \cdot a_{PAR} \quad (4.3)$$

The calculated global radiation albedo values were used in the energy budget calculations of Lake III. The highest PAR-albedo of 0.32 on 1 October 1998 was equivalent to a global radiation albedo (henceforth "albedo") of 0.2. This is high compared to lakes without suspended erosion particle input, where albedo at the same time was assumed to be 0.09.

4.3.5 Euphotic zone

From the turbidity profile values, the depth of the euphotic zone was calculated. The depth of the euphotic zone is limited by turbidity and is defined as the depth which is reached by 1 % of the incident radiation through the water surface. The euphotic zone is that part of a lake where phototrophic organisms usually live. The depth of the euphotic zone is not a sharp boundary, since even phototrophic organisms can live below this zone employing a heterotrophic life style. The variations of the euphotic depth are more or less inversely proportional to the attenuation coefficient (Figure 4.5). The differences are large over a season and from year to year. In 1997 the euphotic zone extended into the hypolimnion from July to the beginning of October. In 1996 it reached the hypolimnion only in July and August, while for 1998 the light was already limiting in 4 m depth in parts of August. In the calculations of the euphotic depth only downwelling radiation was considered. According to the albedo measurements, a significant proportion of radiation can be scattered at particles, leading in addition to an upwelling radiation field. In the PAR spectrum up to 30 % of the radiation at a certain depth can originate from sources below that depth. This means that the real euphotic depth would be slightly lower than the values in Figure 4.5 suggest.

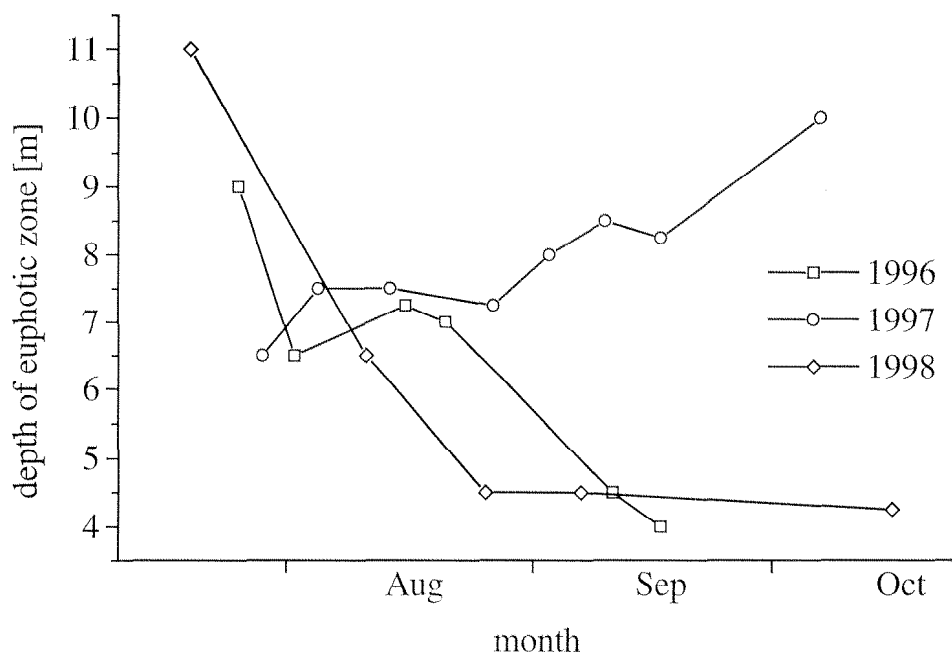


Figure 4.5: Calculated depth of the theoretical euphotic zone of Lake III for the period from 15 July to 20 October in the years 1996 to 1998.

4.4 Interpretation of suspended particle concentration variability

Here we address the question, why the particle concentration varied from year to year and even during the summer season. It is also interesting to know why turbidity in lake III is usually larger in the hypolimnion than in the epilimnion. To answer these questions we considered all aspects involved in the particle input to Lake III. The years 1997 and 1998 were entirely different with regard of the particle concentration in Lake III. In 1997 the turbidity was quite low at all times. This implies that the input of particles must have been minimal throughout the summer of 1997.

From Figure 4.1, it becomes clear that some of the glacier ice melted after the snow had started to disappear from the glacier around 17 August 1997. A small rise in the water attenuation coefficient below 10 m was observed during the second half of August (Figure 4.3). The average radiation flux for the time when the glacier was at least partially snow-free was $38 \text{ W}\cdot\text{m}^{-2}$ in 1997 and $82 \text{ W}\cdot\text{m}^{-2}$ in 1998. Due to the much larger glacial meltwater production, a twofold input of particles could be expected in 1998 compared to 1997. The average turbidity of Lake III in 1998 at times exceeded 50 NTU while the value for 1997 was always lower than 10 NTU. These observations seem to indicate that particle transport to Lake III is not linearly dependent on radiation energy input to the glacier. There are two possible explanations for this observation. Firstly, the wash out of suspended erosion particles from beneath the glacier could be

more efficient during heavy melting episodes. Collins (1988) suggested that this may be the case for alpine glaciers after long periods of below average melting. The size of this effect is not known for the Jöri glacier. Secondly, the flow regime of the outflowing water of Lake XIV may change depending on its surface level. Although turbid water was still observed in Lake XIV in September 1997 and 1998, the overall turbidity in Lake III did not increase any further during that time period. It seems that no water flows to Lake III, once the surface level of Lake XIV is below the visible outflow as it was observed during most of September 1997 and 1998. Even when the level is as high as the visible outflow, as was the case during most of the time between 1 and 10 September 1997 the increase in turbidity in Lake III seems to be negligible or even absent. The largest increases in turbidity were observed in the first half of August 1998, when the surface level of Lake XIV was at its highest, covering the visible outflow with water. It seems that a high water level in Lake XIV increases the water flow to Lake III over proportionately.

This hypothesis is supported by the measurements of particle size in Lakes II, III and XIV (Summa, 1998). 50 % of the particles in Lake XIV were larger than 42 μm , while this value was 29 μm and 10 μm for Lakes II and III respectively. It takes a 10 μm particle 1 hour to settle 1 m, while for a 40 μm particle the time is only 4 minutes. The water flowing towards Lake III seems to originate from surface water of Lake XIV, which contains mostly smaller particles; the larger ones having settled already.

Several factors have to be fulfilled for a large suspended erosion particle input to Lake III; the main one being the time at which the snow on the glacier partially disappears. An early snow melt favoring low albedo on the glacier and thus high radiation energy initiates a massive water flow from the glacier creating a high water level in Lake XIV which leads to large water flow to Lake III. If the high water level is due to heavy precipitation or snow melt only, the water in Lake XIV is less turbid, as was observed in both 1997 and 1998, and turbidity in Lake III will not increase or even be diluted.

4.4.1 Suspended erosion particles in other lakes

Optical properties and turbidity was only measured in Lake III. Information on the other lakes is based on observations without measurements. With regard to turbidity there are two types of lakes in the catchment, those with glacial water inflow and those without. As mentioned earlier, the glacial lakes are Lakes I, II, III, XIV, XV, XVI, XVIII, XIX, XX. No information was collected so far on lakes XV and above because they are all rather small.

Since all glacier meltwater flows through Lake XIV, it is the most turbid lake in the catchment from the time when the glacier starts melting to the time when it dries out in late fall. The lake acts as sediment trap; the largest particles settle quickly and the water leaving Lake XIV is less turbid than the inflowing water. Since most of the water from Lake XIV flows into Lakes I and II, those lakes are usually more turbid than Lake III, which obtains only a small fraction of its water from Lake XIV. The times when this is not the case is during snowmelt in September and October or after heavy rain events in that same period. Because of the low V/C ratio (Table 5.3) of Lakes I and II the turbid water can be substituted quickly by clear rain or meltwater.

4.5 Conclusions

Turbidity not only influences the changing color of a lake, it also contributes to its energy budget (see chapter 5). Albedo in turbid lakes is generally much higher than in clear lakes (Koenings et al., 1991). The global radiation albedo measured at Lake III was in the range of 0.08 to 0.17 and the calculated values were up to 0.2. The resulting global radiation input to Lake III is up to 15 % less than what it would be if Lake III was clear. In general, the energy accumulation of a turbid lake will be smaller than that for a clear lake if they are both subject to the same meteorological conditions.

Due to the high attenuation coefficients in Lake III, radiation is absorbed mainly in the top layers from August to October. This leads to a shallow epilimnion if the lake is not subject to constant wind induced surface turbulences. Because most of the energy is stored in the top meters, the lake loses energy readily through radiative and convective processes and the total amount of energy stored is lower than in a comparable clear lake. Since the energy content is small in a glacial lake in general, it attains isothermal conditions earlier in the fall and it freezes earlier than a clear lake.

Life supporting ecological conditions are also quite different from year to year. Phototrophic microorganisms, for example, are most productive in a layer of the lake where they receive sufficient light and where they are not constantly displaced by turbulences. Also nutrient concentrations should be high enough in order for the algae to grow and reproduce. The trophic conditions are most favorable below the thermocline in nutrient rich, mostly calm water layers. Here, nutrients are probably enriched due to the ion scavenging ability of erosion particles (e.g. Cuker 1993, Fukushima 1991). Towards fall, light becomes growth limiting as observed in September 1996 and 1998 (Figure 4.5). Under these conditions, the chlorophyll *a* concentrations were low and the remaining algae were most abundant in less favorable habitats closer to the surface of the lake (Hinder et al., 1999).

5 Energy budget of a high mountain lake

5.1 Introduction

The water temperature distribution in a lake is of great importance for the growth of biota, since the temperature determines growth rates (Stefan et al., 1996). Ecologically important is the fact, that temperature stratification divides a lake into hypolimnion and epilimnion, two compartments which differ also with regard to water mass stability and mixing. Energy budget calculations are well suited to define the living conditions for biota in a lake and they are prerequisites for any numerical lake simulation model. The energy budget components are the input variables for the models. To make water temperature projections for lakes of different geometries at different latitudes and altitudes, and for possible climate change scenarios, numerical simulation models become useful ecological tools (Hondzo and Stefan, 1993).

Heat budget components are not of equal proportions at all lakes. In large lowland lakes some heat components which are important for high mountain lakes are usually neglected in the calculation because they are too small to contribute significantly to the entire heat budget (Marti and Imboden, 1986; Livingstone and Imboden, 1989; Hondzo and Stefan, 1993). The concepts of the heat flux calculations from lowland lakes were applied to the mountain lakes to evaluate whether these concepts can be applied in alpine waters. Some stratification developments unique for mountain lakes will be discussed and a method to calculate lake surface water temperature (henceforth referred to as "LSWT") is evaluated and applied to the six largest lakes inside the Jöri catchment and two lakes situated outside.

5.2 Energy budget components

The total heat flow H_{tot} from atmosphere to water is determined by the following terms (Marti and Imboden, 1986):

$$H_{tot} = H_S + H_{La} + H_{Le} + H_E + H_C + H_F + H_{SD} + H_P \quad (5.1)$$

- H_S : global radiation absorption
- H_{La} : longwave radiation absorption
- H_{Le} : longwave radiation emission
- H_E : latent heat flux
- H_C : sensible heat flux
- H_F : throughflow heat flux
- H_{SD} : sediment heat flux
- H_P : precipitation heat flux

If H_{tot} is positive the lake heat content and the volume-averaged lake temperature will rise. The formulae of the heat flux components in chapters 5.2.1 through 5.2.6 were taken from Marti and Imboden (1986).

5.2.1 Shortwave radiation

Global radiation (see chapter 3.7) is partially reflected at a lake surface. How much of the radiation is being reflected depends on the incident angle of the ray of light (Fresnel's law) as well as the structure of the water surface. If the zenith angle is 90° , only little global radiation is reflected at the water surface; depending on wave activity and transmissivity of the atmosphere the value is from 1 % to 6 % (Payne, 1972). The mean reflectivity at latitude 45° N is 4 % in July and 14 % in January (Kuhn, 1977). Particles, organic matter or organisms can also increase the albedo of a lake surface through scattering. This can have large effects in lakes that are fed by particle rich glacier meltwater (see chapter 4.3.4). In shallow and clear lakes portions of global radiation can also be reflected at the ground. The albedo of a lake is therefore by no means constant over a year and it should be measured to prevent erroneous calculations. The amount of global radiation energy absorbed by the water can be described as follows:

$$H_s = (1 - \alpha) \cdot R_{sw} \quad (5.2)$$

α : reflected portion of global radiation at the water surface (lake albedo) [-]

R_{sw} : global radiation [$W \cdot m^{-2}$]

Most of global radiation is not absorbed at the water surface, but penetrates into the water body depending on light attenuation. In a turbid lake most of global radiation is absorbed in the top few meters, while in a clear lake significant amounts (>1 %) can reach depths of several dozen meters. The calculations for Lake III are based on global radiation measurements with a pyranometer and albedo was evaluated using sensors measuring PAR from the atmosphere and PAR reflected at the water surface. Due to horizon obstruction, global radiation observations are only representative for the point that they are measured at. Therefore, at Lake III, they were calculated as a mean for the total lake area (see chapter 3.7.3).

5.2.2 Longwave radiation

Incoming longwave radiation was described in chapter 3.8. It is assumed that 97 % of the longwave radiation is absorbed by lakes.

Longwave emission of the lake is easy to calculate if one takes water as a nearly black body with an emission coefficient ε_w of 0.97. The Stefan-Boltzmann law can be applied as:

$$H_{Le} = \varepsilon_w \cdot \sigma \cdot T_s^4 \quad (5.3)$$

T_s : Surface water temperature [K]

5.2.3 Latent and sensible heat flux

These two heat fluxes both depend on either the gradient of temperature (sensible heat flux) or vapor pressure (latent heat flux) across the air-water interface, and on the wind speed, as was already stated by Dalton in 1802. Similar approaches are used for the calculation of the latent and the sensible heat fluxes. The gradient of the quantity to be exchanged at the air-water interface is multiplied by a wind function. The wind functions $f(u)$ and $f^*(u)$ enter into the convective heat transfer relationships (5.4) and (5.5):

$$H_E = -f(u) \cdot (e_s - e_a) \quad (5.4)$$

e_s : saturated water vapor pressure at the lake surface temperature [hPa]
 e_a : water vapor pressure of the atmosphere [hPa]
 u : wind speed [$m \cdot s^{-1}$]

$$H_C = -f^*(u) \cdot (T_s - T_a) \quad (5.5)$$

The wind function $f(u)$ and $f^*(u)$ are proportional through the Bowen ratio Bo (Bowen, 1926), the latter being between 0.61 and 0.65:

$$\frac{f^*(u)}{f(u)} = \frac{Bo \cdot p}{1000} \quad (5.6)$$

p : air pressure [hPa]

There are many different approaches to define the wind function $f(u)$, which depends largely on the size and the sheltering of the lake (Sweers, 1976; Hondzo and Stefan, 1993). The wind function usually takes the form:

$$f(u) = a + b \cdot u, \quad (5.7)$$

where a and b are constants. The constant a implicitly accounts for buoyancy or instability as well as other possible factors such as unsteadiness and finite anemometer threshold (low wind speeds recorded as zero) (Adams et al., 1990). Some of the proposed values for a and b are shown in Table 5.1.

| author | equation |
|-----------------------------|-----------------------------------------|
| McMillan (1973) | $f(u) = 3.6 + 2.5 \cdot u_3$ |
| Harbeck (1962) | $f(u) = 9.17 \cdot A^{-0.05} \cdot u_2$ |
| Volker (1951) | $f(u) = 7.2 + 1.79 \cdot u$ |
| Keijman and Koopmans (1973) | $f(u) = 2.63 \cdot u_2$ |
| Brady et al. (1969) | $f(u) = 6.9 + 0.49 \cdot u_2^2$ |

Table 5.1: Proposed wind functions by several authors. The subscript at wind speed u refers to the measurement height of wind speed at which the function yields the best results. A is the surface of the lake, the surface dependent function was introduced by Harbeck (1962). The different equations were taken from Sweers (1976).

It is quite common to use the wind function as a calibration parameter for lake energy exchange models (Marti and Imboden, 1986; Bonderer, 1997). In these cases the parameters a and b of the wind function are changed for a best fit of the lake model. However, the fitting process does not only adapt to the deviations caused by the wind regime, but also partly reduces the deviations caused by the neglected heat fluxes from throughflow, precipitation and by changes in albedo. This may be beneficial for lakes where the neglected terms are small. For mountain lakes, fitting the data from one year to an optimized wind function would cause model deviations in other years if throughflow, precipitation and albedo changes are included in the fitting process.

It is generally difficult to find wind functions in the literature that are applicable for lakes of different sizes and at different locations. Also, the calculated wind functions are dependent on the measurement height of wind speed and on the reaction of the wind gauge at low wind speeds (Sweers, 1976). There are differences between measurements made over water and measurements made over land. The use of a wind function for the flux calculations at the Jöri lakes is further complicated because the lakes are small compared to the lakes at which the wind functions are usually used and they are embedded in rugged terrain, which is seldom common for lowland lakes. Farther out from the shoreline the wind speed over a sheltered lake usually increases, increasing in

turn the mixing of the air and thus intensifying the transport efficiency by turbulence. On the other hand, the greater the distance from the shoreline the more moist the air and the closer the air temperature to the water temperature above the lake surface will be, and this tends to reduce latent and sensible heat flux (Venäläinen et al., 1998). For the small Jöri lakes it can be assumed that the increase of humidity over the lake is small. Therefore, the convective heat fluxes will be enhanced in lakes where wind forcing is large. To determine precise values of latent and sensible heat flux, it is inevitable that they are calculated using high resolution profile measurements of temperature, humidity and wind in the middle of the lake. These measurements are rarely available for financial and practical reasons, and also for Jöri Lake III we relied on standard meteorological measurements from a station located on the lake shore. In spite of all the shortcomings of the wind function for small mountain lakes, the bulk aerodynamic method was applied for the modeling of water temperature at the Jöri lakes because it still yielded accurate results. The wind function of McMillan (1973) was applied, including the correction factors by Harbeck (1962) for height of the wind measurement and for size of the lake. The resulting parameters used for the Jöri catchment were $a = 4.2$ and $b = 2.65$.

5.2.4 Precipitation heat flux

The temperature difference between the precipitation and the lake water surface causes an energy flux of positive or negative value to the lake. Since the precipitation volume is usually small compared to the lake volume, the effect on lake temperature is minimal. This is different, when the precipitation falls in the form of snow. Because of the latent heat of fusion, the energy loss during snowfall is 80 times higher than for rain with a temperature 1 K lower than that of the water surface. For a mountain lake, where snowfall events are quite frequent even in the summer, the precipitation heat flux should not be neglected. The precipitation heat flux including the latent heat of fusion is as follows:

$$H_p = P \cdot c_p \cdot \rho \cdot (T_a - T_s) - P \cdot c_m \cdot \rho \quad (5.8)$$

- P : amount of precipitation [mm]
- c_m : specific heat of ice-melt [$J \cdot kg^{-1}$]
- c_p : specific heat of water [$J \cdot kg^{-1} \cdot K^{-1}$]
- ρ : density of water [$kg \cdot m^{-3}$]

At the Jöri AWS, precipitation was only measured with an unheated rain gauge. The measured values during snow fall events are therefore not accurate. All the

precipitation data for the calculation of the energy budget were taken from the Weissfluhjoch AWS (see chapter 3.9). Although the precipitation differences between Jöri and Weissfluhjoch are significant during thunderstorms, the influence on the energy budget is insignificant because of the small heat flux associated with rain. During snowfall events, the precipitation values are much more homogeneous (see chapter 3.9). When a snow cover already exists around the lake during snowfall, then blowing snow can enhance the energy loss due to precipitation. A quantification of this effect is not possible with the resources available in the Jöri catchment.

5.2.5 Throughflow heat flux

Heat from throughflow of water is usually small in large lakes and can be neglected, if the temperature difference between water inflow and outflow is close to 0° C, which usually is the case for lowland lakes (Livingstone, 1989). In the Jöri lakes however, water often comes from snowmelt, glacier melt or cold subsurface inflows and therefore the inflowing water can be more than 10 K colder than the outflowing surface water. The cold inflows coupled with the small area of the lakes can cause a significant heat loss. Also, the distance the water flows until it reaches a lake is short, not allowing stream water to heat up to lake temperature. Generally, water leaves a lake at the surface by means of an outflow, whereas inflow can reach great depths, depending on stream temperature and density stratification of the lake. Measurement of inflow volume can be difficult not only in mountainous regions. Surface streams entering the lake may only account for part of the inflow volume, the other part being from subsurface inflows. Further complication arises from the fact that subsurface inflows are usually colder due to the lack of radiative heating and therefore cause an over proportionate heat loss in relation to the surface stream inflow. The throughflow heat flux can be described as follows:

$$H_F = \frac{Q \cdot c_p \cdot \rho \cdot (T_i - T_s)}{A} \quad (5.9)$$

Q : inflow volume [$m^3 \cdot s^{-1}$]

A : lake surface area [m^2]

T_i : mean inflow temperature [K]

For Jöri Lake III only the temperature of the inflowing surface stream was explicitly measured. The mean volume of the inflowing water could only be estimated through the precipitation measured and the approximate ratio of snow-covered area in the catchment. For the subsurface inflow the estimations are even more complicated

because its volume probably depends on the surface level of Lake XIV (see chapter 4.2.2). Furthermore, because the location of its entry is unknown, no temperature information is available. It was assumed that the outflow of the glacier water between Lake III and Lake I has approximately the same temperature as the subsurface inflow to Lake III because it also flows from Lake XIV to lower elevation through the ground. From these assumptions some rough estimates of mean throughflow heat flux could be made.

5.2.6 Sediment heat flux

Heat from sediments may be of significance in shallow lakes and in lakes with an ice cover period. Heat absorbed from solar radiation and conduction at the water sediment interface during the summer will be released in colder periods (Bengtsson and Svensson, 1996). During the ice and snow-covered season, part of the heat input into the lake comes from heat stored in the sediments. The opposite is true after ice break-up, when the warmer water provides energy to heat up the sediment. The heat flux from the sediments is generally in the order of a few $\text{W}\cdot\text{m}^{-2}$, being largest when water temperature fluctuates heavily (Fang and Stefan, 1996). Thus, the sediment heat flux acts as a kind of buffer reducing large water temperature fluctuations slightly. The dampening is most prominent in shallow lakes (Bengtsson and Svensson, 1996), where the sediment heat flux can reach values of up to $50 \text{ W}\cdot\text{m}^{-2}$ on rare occasions. The lake temperature under the ice will be slightly higher and the ice cover duration may be decreased slightly for lakes with a higher heat flux from the sediments. There has to be good knowledge of the temperature distribution at the water-sediment interface in order to calculate the correct fluxes. For Jöri Lake III these fluxes are only known for a short period, therefore not allowing calculation of the heat flux from the sediments. The conductive heat exchange H_{SD} between the water and the sediments can be determined from the temperature gradient at the sediment-water interface:

$$H_{SD} = -k_s \cdot \left(\frac{dT_s}{dz} \right) \quad (5.10)$$

k_s : thermal conductivity of the sediment [$\text{W}\cdot\text{m}^{-1}\cdot\text{K}^{-1}$]

5.3 Heat content and heat flux calculations for Lake III

For the years 1996 through 1998 the energy budget of Lake III was calculated for the open-water period. During this period the AWS at the shore of the lake recorded data at 10-minute intervals, while two thermistor chains measured the temperature profile in 20-minute steps. Where data were not available at the Jöri AWS, observations

from AWSs outside the catchment were used, such as from 20 June to 14 July 1996. The calculated heat fluxes were compared with the measured energy changes of the lake based on the temperature changes in the lake profile. The formulae for the heat fluxes which determine the lake water temperature were described in the previous chapter.

5.3.1 Thermistor data from Lake III

Thermistor data are available at 20-minute intervals for most of the open-water periods 1996 to 1998. They were provided by Olivier Besson from the university of Neuchâtel. Missing data include 20 June through 26 July and 1 October through 20 October of 1996 as well as 28 July through 5 August of 1997. During the winter, temperatures were recorded in 3-hour intervals. The thermistor data were used to calculate the lake's heat content, to analyze the stratification development and to compare the measured heat fluxes to the calculated ones. To facilitate analysis and calculations, the temperatures were linearly interpolated to depths with an increment of 1 m. For the comparisons with the calculated energy fluxes, the high time resolution could not be used. Internal waves called "seiches" at times changes the water temperature at a certain depth by 3 K in just 20 minutes. This would have caused large, unreal heat fluxes although internal seiches were no heat sources or sinks. The thermistors only measured temperature locally and while temperatures changed at the measuring points due to seiches, they changed in the other direction at points without measurements. In Figure 5.1 the reduced wave activity due to averaging can be seen for the depth of 2 m. While the fluctuations in the 20-minute values are large throughout the period from 18 to 27 August 1997, the 6-hourly means seem to filter the seiches sufficiently and still show some diurnal temperature variation associated with solar heating of the epilimnion. For the comparisons with the calculated heat budget 6-hourly or daily means were used.

Although the time constant of the thermistor sensors in water is quite low as opposed to the time constant in air, heating effects at the sensors due to solar radiation can still play an important role. This effect was evaluated at Jöri Lake III and was not detectable at depths greater than 3 m. This is due to the high turbidity in Lake III not permitting substantial amounts of solar radiation to penetrate below 3 m (see chapter 4.3.3). Above 3 m depth it is difficult to prove the effect because it goes hand in hand with the diurnal warming and cooling of the mixed layer. Because the extent of the effect could not be determined, the obtained temperature measurements were not corrected in any way, they may be slightly too high in the uppermost layers of Lake III. In clear lakes the effect may be significant even in greater depths, where diurnal temperature fluctuations can be observed (pers. com. H. J. Thies, University of

Innsbruck). They have no physical background since in deeper layers the heat can only be dispersed slowly through internal waves and not as quickly as at the surface.

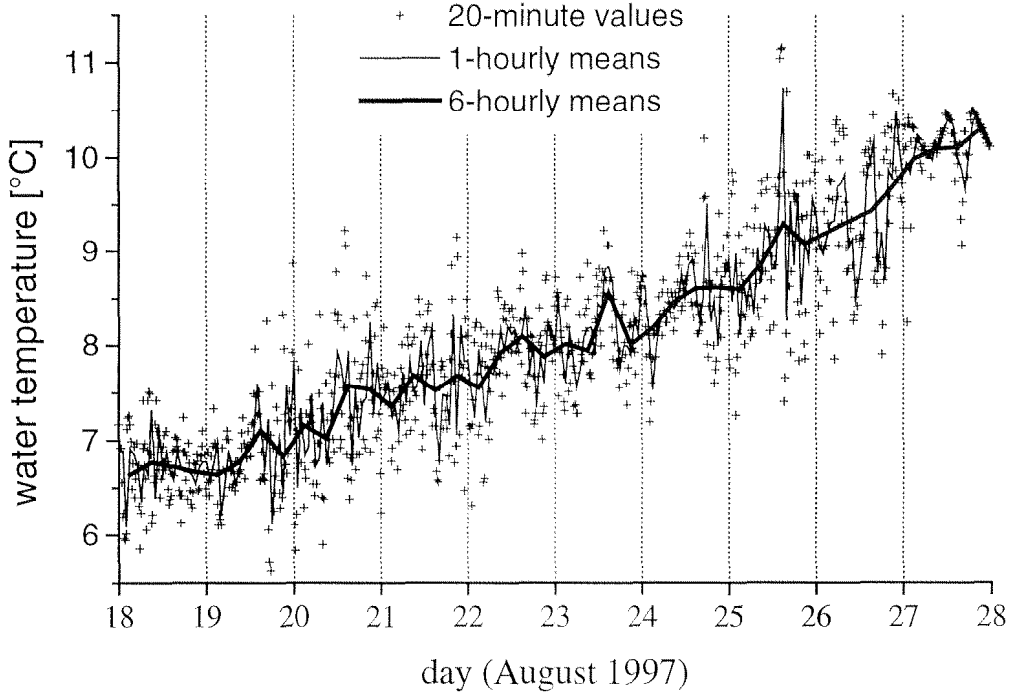


Figure 5.1: Water temperatures of Lake III for different averaging periods at a depth of 2 m over a 10-day period in 1997. The grid lines correspond to the time of midnight each day.

5.3.2 Lake III heat content

The heat content per area was calculated for all days for which thermistor data were available. The mean lake temperature was calculated taking into account the declining volume with depth. Temperatures below 16 m were not measured with thermistors, but point measurements during the open-water period indicate that the temperatures below 16 m were not different from those at 16 m. Thus, for the depths between 16 m and 22 m, which account for only 6 % of the total lake volume, the temperatures recorded by the lowest thermistor at 16 m were applied.

To convert the mean lake temperature T_{mean} to the heat content per area of the lake, the mean depth z_{mean} of the lake is used, which is 10.1 m in Lake III:

$$E_{tot} = T_{mean} \cdot c_p \cdot \rho \cdot z_{mean} \quad [Joule] \quad (5.11)$$

Because in Lake III the surface level is not constant, z_{mean} is a function of time, which further complicates the calculation of E_{tot} . During the open-water period the

surface level of Lake III was monitored and thus z_{mean} can be calculated with the use of the bathymetric data. Because the lake surface level drops in the course of the summer, less and less energy is needed to change the mean lake temperature by 1 K. A level of 1 m below maximum increases the temperature gain/loss by 5.5 % compared to the maximum surface level. For a lake with a depth of 100 m, the effect of a 1 m level drop is assumed to be a 1 % increased temperature gain/loss per area.

The daily heat flux into the lake is equivalent to the total energy change from one day to the next (midnight to midnight). To calculate this and to eliminate the effects of seiches, 6-hourly means were calculated centered at midnight for best comparisons with the calculated daily heat flux. Thus, the heat content at midnight was assumed to be the mean between 9 PM and 3 AM of the following day.

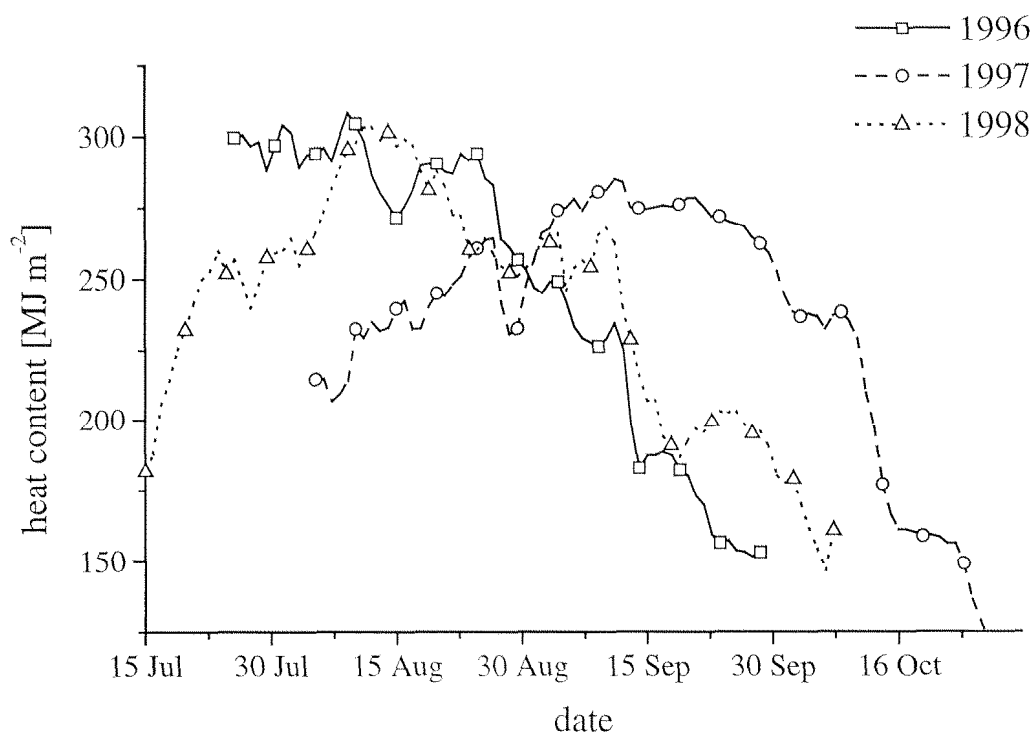


Figure 5.2: Heat content of Lake III of years 1996 through 1998 for the periods from 15 July to 31 October. The parameter energy content refers to the surplus of heat in a lake compared to a mean lake temperature of 0° C. Graphs are plotted where data were available.

Figure 5.2 shows the heat content for the summer periods of 1996 to 1998. The differences between the years are large at times, especially in early summer and early fall. In July and parts of August the differences are due to the different break-up dates. Lake III was mostly or totally ice-free from 20 June 1996, 28 July 1997 and 15 July 1998 (see chapter 6.3.1). The mean temperature of a lake with a total or partial ice cover

is usually below 4° C and can only reach values slightly above 4° C during daylight or when the area of the ice cover is minimal compared to the surface area of the lake. For this reason, the heat content cannot exceed 175 MJ·m⁻² (corresponding to a mean lake temperature of 4° C) before the ice finally breaks up. As opposed to the sinusoidal shape of heat content over the year in lowland lakes (Marti and Imboden, 1986), the heat content is nearly constant without large fluctuations for the greater part of the year during the ice cover period (Figure 5.3). After ice melt, the heat content rises quickly and stays at a higher level for 2 to 3 months at the most before strong cold fronts reduce the heat content to 175 MJ·m⁻². The lake subsequently cools down to between 1° C and 3° C before it finally freezes again.

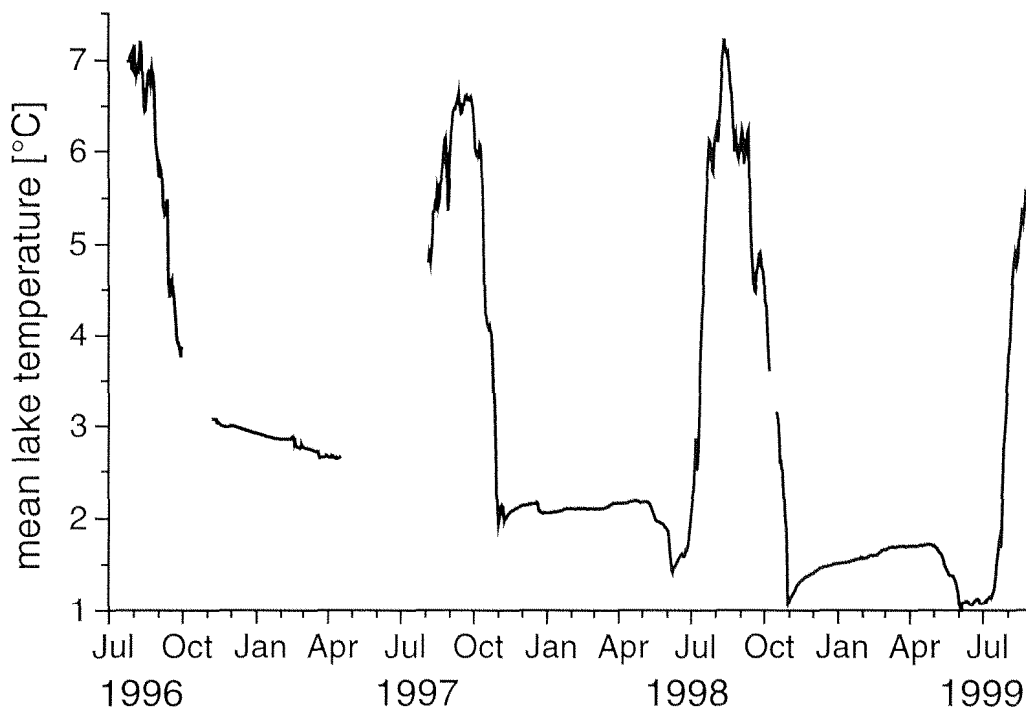


Figure 5.3: Mean temperature of Lake III from 15 July 1996 to 27 August 1999. The ticks indicate the first day of each month.

5.3.3 Lake III heat flux calculation

In a first step only those exchange processes that are thought to be important in lowland lakes were included in the calculations. These include global radiation, incoming and outgoing longwave radiation, latent and sensible heat flux (Marti and Imboden, 1986; Livingstone, 1989; Henderson-Sellers, 1986; Hondzo and Stefan, 1993). To evaluate the importance of the precipitation heat flux, the total heat flux was once calculated including precipitation. The energy exchange calculations were made

according to the formulae in the chapter 5.2. The daily heat flux to Lake III was then compared to the changes in measured heat content. The data used for the heat flux calculations was taken from the Jöri AWS at the shore of Lake III. The albedo of the lake was used according to the calculations in chapter 4.3.4. The mean global radiation was calculated for the total lake surface (see chapter 3.7.3). In the calculations where precipitation was used, the precipitation was assumed to fall in the form of snow when daily mean temperature was below 1.5°C . This high value was used to include days where snow falls at temperatures below freezing when daily mean temperature is above 0°C because of the solar heating during the day. Nevertheless Rohrer and Braun (1994) found that when using daily mean temperature to classify the precipitation type, over 10 % of the events are misclassified (see below).

Figure 5.4 shows the daily differences between the calculated and the measured heat fluxes for the years 1996 to 1998 including the heat flux from precipitation (solid line) and without it (dotted line). Note that the calculated heat flux is larger than the measured one on most of the days in July and August. This is most pronounced in 1998.

There are some large deviations at the end of August and the middle of September 1996 which disappear when the precipitation heat flux is included. This indicates that precipitation heat flux is not a neglectable factor in energy budget calculations of mountain lakes. Including the precipitation heat flux eliminates some of the immense deviations. The high peaks which remain, also seem to indicate precipitation onto the lake. The two largest peaks of the solid line in Figure 5.4 are from 28 August 1997 and 5 September 1998. They represent days with heavy precipitation (35 mm and 45 mm respectively, measured at Weissfluhjoch AWS) and daily mean temperature of 5°C and 4°C respectively, both far from the determined snowfall-threshold temperature of 1.5°C . Nevertheless, as the analysis of hourly data shows, on both days a significant amount of precipitation fell in the form of snow. On 28 August 1997 a strong cold front cooled down the atmosphere below freezing after 8 PM CET, producing 28 mm water equivalent of snow until midnight of that day. This would reduce the peak of $150\text{ W}\cdot\text{m}^{-2}$ to as little as $40\text{ W}\cdot\text{m}^{-2}$, which blends in with the rest of the curve. On 5 September 1998 the air temperature was always close to the freezing mark, which makes it difficult to say how much of the precipitation was snowfall. It is assumed, that the peak disappears similarly to the one on 28 August 1997. The values were not corrected and left in their original state because in cases like the one on 5 September 1998 the real amount of snowfall on the lake cannot be evaluated even from 10-minute data. At temperatures between 0°C and 2°C the precipitation type cannot be determined securely without observation (Rohrer and Braun, 1994).

All the heat fluxes used in the energy budget calculations, including precipitation are presented in Figure 5.5, Figure 5.6 and Figure 5.7 on a daily basis for

all three years from the date of ice break-up to 31 October. The only flux being positive all through the open-water period is global radiation. It is the main reason the lake heats up in the summer, all the other heat fluxes usually add to the cooling of the lake. On rare occasions, when air temperature is higher than water temperature, the lake also gains energy from the sensible heat flux. On the rarest occasions, only right after ice break-up, the dew point temperature may be larger than the water temperature, causing condensation on the lake and thus an energy gain. This was the case only once in the three years on 28 July 1997.

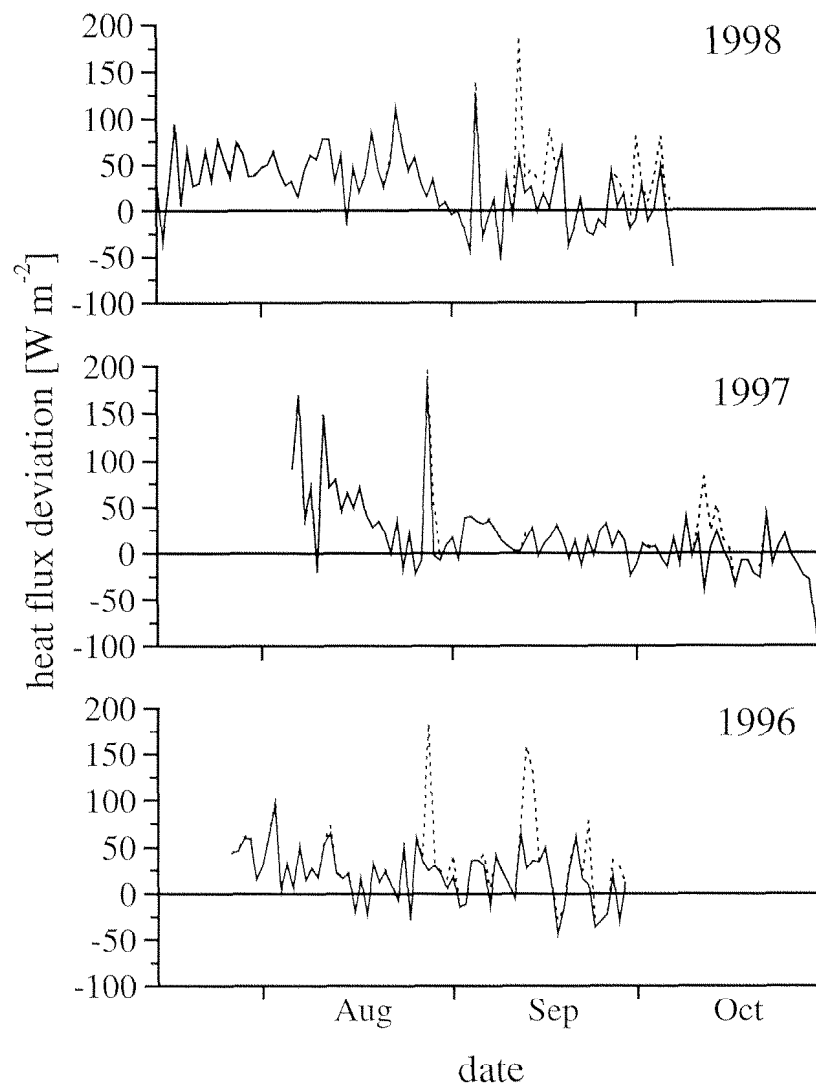


Figure 5.4: Difference between the calculated and the measured daily heat flux in Lake III for years 1996 to 1998. In the calculations presented with dashed lines, the precipitation heat flux was neglected, while in the solid lines it was fully accounted for. Where the dashed line is invisible, the values are equal to one represented by the solid line.

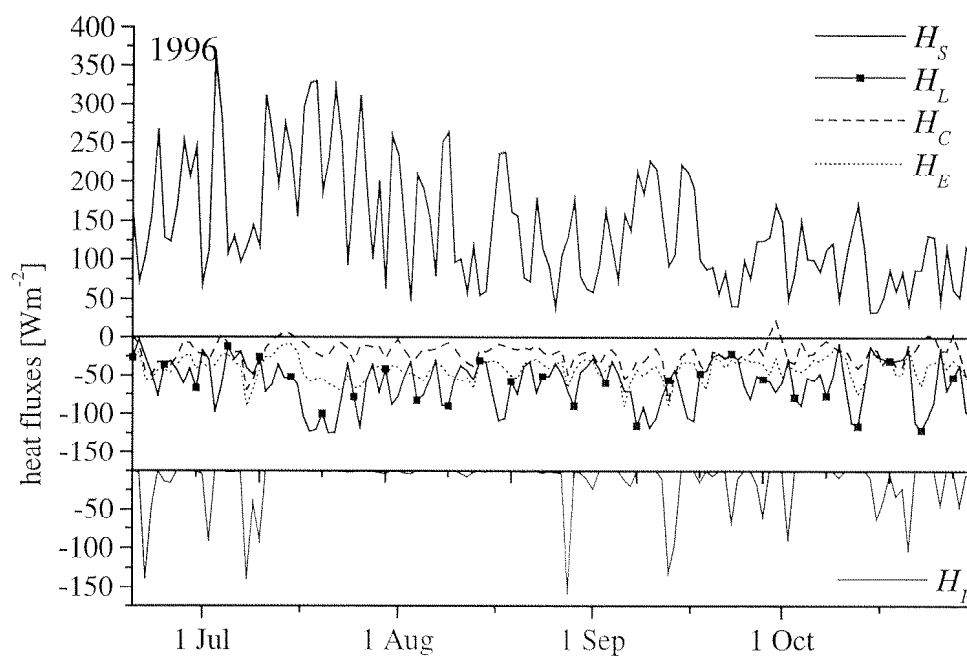


Figure 5.5: Calculated heat fluxes for the open-water season 1996. Note the separate scale for the precipitation heat flux at the bottom of each graph. See chapter 5.2 for abbreviation definitions. H_L is the longwave radiation budget.

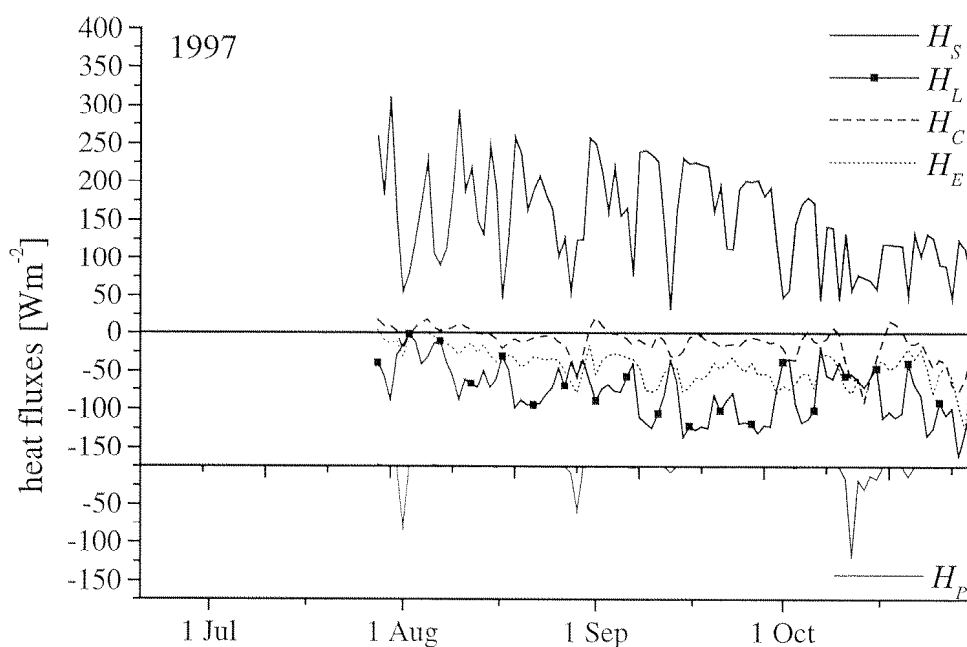


Figure 5.6: Calculated heat fluxes for the open-water season 1997. Note the separate scale for the precipitation heat flux at the bottom of each graph. See chapter 5.2 for abbreviation definitions. H_L is the longwave radiation budget.

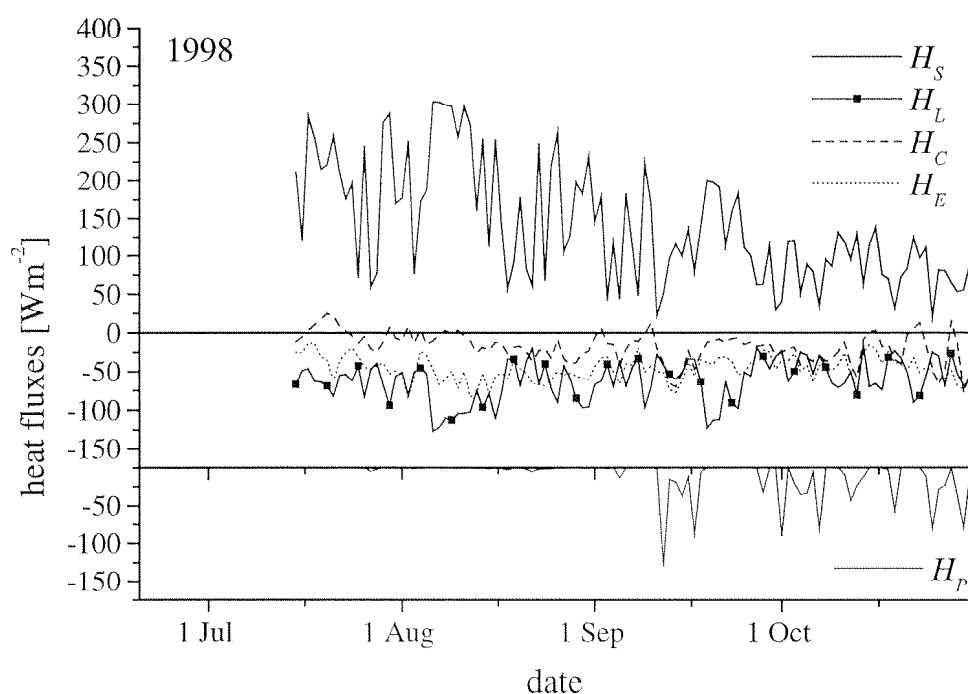


Figure 5.7: Calculated heat fluxes for the open-water season 1998. Note the separate scale for the precipitation heat flux at the bottom of each graph. See chapter 5.2 for abbreviation definitions. H_L is the longwave radiation budget.

Due to the variable meteorological conditions, the heat fluxes usually show large fluctuations from day to day. Only during longer nice weather spells they remain more or less constant (e.g. 14 to 25 September 1997 and 6 to 12 August 1998). Because of the increasing zenith angle of the sun, and the usually increasing albedo of Lake III (see chapter 4.3.4), the heat input from global radiation decreases by more than 50 % from June to October. The other components do not show any significant changes from June to October, except the precipitation heat flux. Snowfall is rare between 10 July and 20 August, therefore the largest heat losses due to precipitation are usually confined to the time before or after that period. The mean values of the heat fluxes over the open-water period are similar, although the ice free periods are of different length in the three years (Table 5.2).

The mean heat loss due to precipitation is quite small compared to the other heat fluxes. Snow does not fall on an open lake surface every day, but when it does, the effects are significant. The heat flux can even be dominated by the precipitation component like on 12 September 1998. The heat loss from longwave radiation, sensible and latent heat flux combined was $130 \text{ W}\cdot\text{m}^{-2}$, the same amount as for the precipitation heat loss alone. The heat flux from global radiation was only $50 \text{ W}\cdot\text{m}^{-2}$ on that day.

| year | SW Rad | LW Rad | sensible heat flux | latent heat flux | heat flux from precipitation |
|------|--------|--------|-----------------------|---------------------|---------------------------------|
| 1996 | 143 | -68 | -20 | -41 | -12 |
| 1997 | 151 | -85 | -13 | -43 | -3 |
| 1998 | 142 | -70 | -18 | -46 | -8 |

Table 5.2: Mean values of all heat fluxes calculated for Lake III for the open-water periods of years 1996, 1997 and 1998. The periods were different from year to year. Positive values indicate a heat flux into Lake III.

5.3.4 Possible errors in heat flux calculations

On most of the days the calculated heat flux is larger than the measured one, even when the precipitation heat flux is included (Figure 5.4). Aside from the fact that the weather sensors may at times not measure accurately, there are also errors associated with the location of the meteorological sensors, time resolution of the measurements and the energy budget formulae. Also, data were not always available due to malfunction of sensors and on those occasions it was estimated from the values at stations nearby. All the precipitation values were taken from Weissfluhjoch (see chapter 3.9).

The meteorological data are assumed to be representative for the whole area of the lake, which may not be correct, although Lake III is small and the AWS is at the shore of the lake. Because the lake is in the middle of rugged terrain, radiation values close to a steep slope may be different from the values measured at the AWS (Figure 6.2). For this reason, the shortwave radiation was adapted to represent the lake surface. For the longwave radiation not enough information was available to adapt it to the lake surface. Other possible heterogeneous variables in or above the lake are LSWT, albedo and wind speed. Air temperature and humidity are assumed to be nearly constant above a lake of this size.

No significant dependence between a single meteorological parameter and the difference between calculated and measured heat fluxes was found. This means that the errors are not proportional to the measurements of any meteorological measurement. The only time dependent error caused by heterogeneous distribution on the lake are the deviations caused by varying ice cover before the lake finally freezes. On 7 October 1998 half of Lake III was covered by thin ice, while the rest was completely ice-free. If heat loss leads to a build-up of an ice cover, then the heat content of the lake does not decrease further because all the cooling is needed for the thickening of the ice cover. On the other hand, a positive heat flux is used up for the melting of a partial ice cover and has less effect on the heat content of a lake. A thin ice cover reduces the input of global

radiation into the lake due to higher albedo. The lake surface is 0° C where an ice cover exists as opposed to 2° C to 4° C without the ice cover in October.

Hypothetical energy budget calculations were performed on Lake III between 5 October and 25 October 1998 and between 25 September and 17 October 1996 assuming a thin ice cover on the lake at that time and comparing the data with heat input under open-water conditions. A mean albedo of the ice of 0.35 was assumed (Matthews and Heaney, 1987). While there was an average heat loss of 31 W·m⁻² for the specified period in the ice-free version, an average heat gain of 6 W·m⁻² was calculated if the lake had been ice-covered. The calculations are of course only valid if the ice cover is reasonably thin (< 5 cm) and if there is no snow covering the ice, which would further reduce global radiation into the lake. The processes leading to ice on a lake are described in the chapter 6.2.

Although seiches were filtered applying 6-hourly means to the measured temperature profiles, some intensive seiches persisted in the data, especially at times when only data from one thermistor chain were available (all of 1996 and until 5 September in 1997). Using daily means of the input variables could be another source of error because of the covariance of wind and air temperature in the sensible as well as latent heat flux calculations. For example assuming a mean surface water temperature of 10° C, a mean air temperature of 10° C and mean wind speed of 3 m·s⁻¹, would lead to a sensible heat flux of 0 W·m⁻². An air temperature of 7° C during the night and 13° C during the day as well as wind speed of 1 m·s⁻¹ during the night and 5 m·s⁻¹ during the day would lead to the same daily means for the input variables. Assuming a constant surface water temperature, the heat flux in the latter case would be 15.3 W·m⁻². In reality, the situation is hardly ever as extreme. The daily mean of the hourly sensible heat flux was calculated between 14 July and 11 September 1998. The result was a mean offset of 0.07 W·m⁻², with a standard deviation of 1.45 W·m⁻². This is small enough to be neglected. For the latent heat flux the situation is expected to be similar.

As a result of the analysis of all these possible error sources, it can be said that the large average deviations between calculated and measured energy fluxes (Figure 5.4) can by no means be explained by these errors.

5.3.5 Estimating the magnitude of neglected heat fluxes

The heat fluxes not included in the calculations were those from the sediment and from the throughflow of water. The sediment heat flux is largest after a rapid increase or decrease in lake water temperature. This would be the case right after ice break-up and later in the summer when cold fronts cool down the lakes. The pattern of the deviations between calculated and measured heat fluxes in Lake III is somewhat consistent with the assumed sediment heat flux direction, being positive after ice break-

up and around zero or negative later (Figure 5.4). This can be seen well in the year 1997 and 1998, whereas in 1996 no data are available for the first month after the break-up of the ice. However, the calculated deviations are too large to be totally accounted to the sediment heat flux. They are in the order of $50 \text{ W}\cdot\text{m}^{-2}$ after ice break-up and sometimes even higher (1997). Fang and Stefan (1996) showed that the mean sediment heat flux over one month cannot exceed $10 \text{ W}\cdot\text{m}^{-2}$ for a lake as deep as Lake III, not even during the rapid heating of the lake after ice break-up. The greater part of the deviations from the measured data can therefore not be explained by sediment heat fluxes. However, the sediment heat flux seems to be large enough to make a significant difference in water temperature. They should be considered when lake water temperature changes quickly like in shallow mountain lakes.

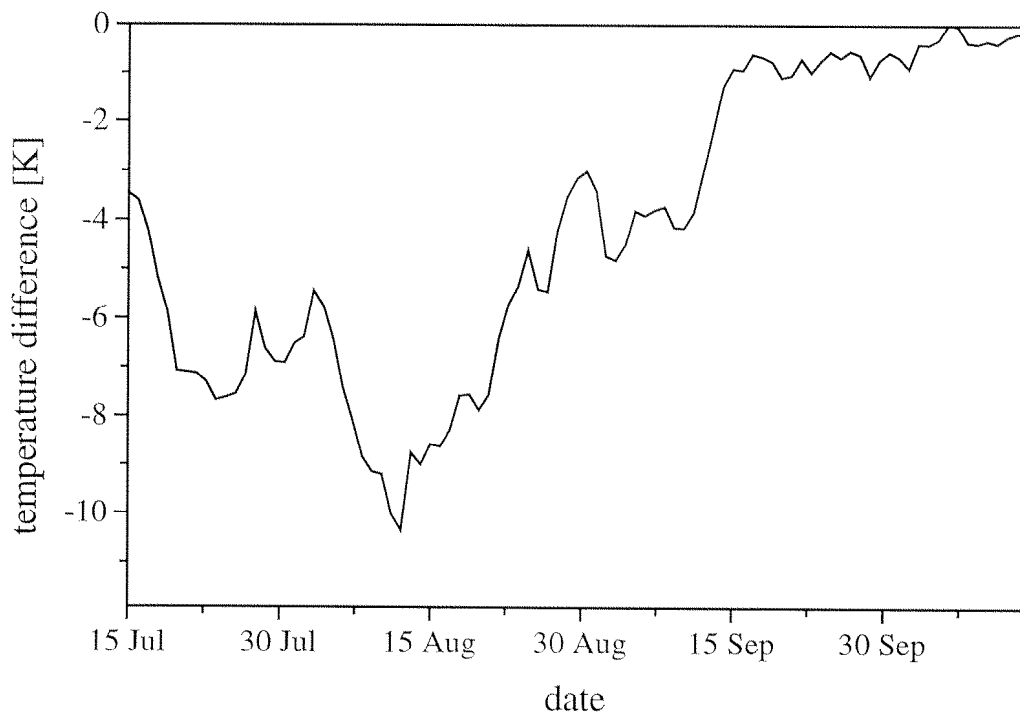


Figure 5.8: Daily mean water temperature difference between the glacier subsurface stream below Lake III and surface water temperature of Lake III in 1998, the latter being warmer.

Inflow temperature of the major surface stream to Lake III was measured from 25 June to 15 October 1998. Because most of the snow in a catchment usually melts before the ice disappears on the lake, the temperature of the surface stream water flowing into Lake III is not much lower than surface water temperature of the lake itself for the time between 15 July and 31 August. Calculating the heat flux due to throughflow of the surface stream alone leads to a mean value of $-5 \text{ W}\cdot\text{m}^{-2}$ assuming an inflow of $40 \text{ l}\cdot\text{s}^{-1}$ and a temperature difference of 1.5 K between stream water and lake

surface water, the latter being higher. This heat flux is too low to explain the deviations of the calculated heat flux from the measured one. However, inflowing water to Lake III stems not only from this surface stream. There is also a subsurface inflow with water from snow and glacier melt (see chapter 4.2.2). The inflowing water from the glacier is assumed to have a temperature between 0° C and 4° C. To get some idea about the variability of the subsurface inflow temperature, stream water temperature was measured where glacier meltwater exits from a moraine between Lakes I and III. The temperature difference between the glacial subsurface stream and Lake III surface temperature averaged 6.7° C from 15 July to 31 August. The temperature difference was less than 4° C after 1 September and less than 1° C after 14 September (Figure 5.8).

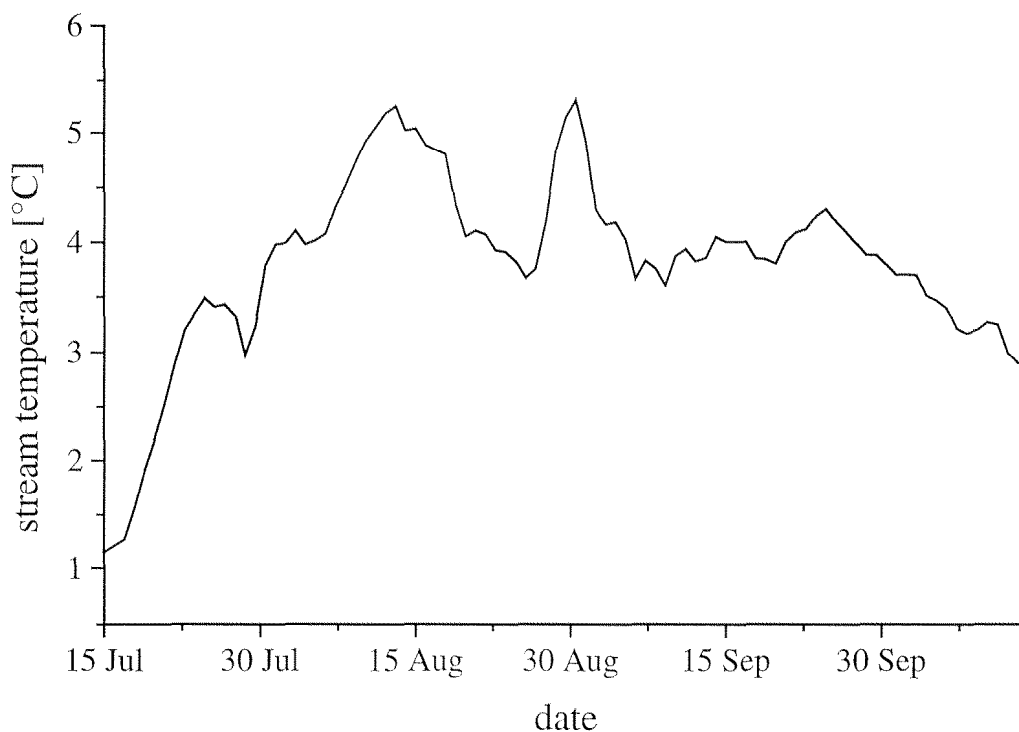


Figure 5.9: Daily mean water temperature at the subsurface stream outflow at the moraine between Lakes I and III in 1998.

The reason for the temperature changes (Figure 5.9) in the water exiting the moraine could not be evaluated precisely. Because the flow time of the water from Lake XIV to Lake I or III is in the order of a few hours (Ullmann, 1998) the water temperature is probably dominated by the ground temperature. Figure 5.9 shows a steady increase of stream temperature after 15 July 1998, but the rise stops on 12 August. Judging from the water temperature measured in Lake XIV, the moraine outflow temperature could actually be the mean value of Lake XIV surface water temperature, averaged over several days. The hypothesis is that the averaging period

depends on the length of the flow path below the surface, as well as on the thermal conductivity properties of the ground, due to heat exchanges between the subsurface stream water and the ground. It is assumed that the water temperature of the subsurface flow from Lake XIV to Lake III is close to that measured at the moraine exit because of its similar subsurface path length. There is no information on the amount of glacier water entering Lake III subsurface due to the complicated outflow situation at Lake XIV (see chapter 4.2.2). Assuming a cold water inflow of about $50 \text{ l}\cdot\text{s}^{-1}$ (based on catchment size and taking glacier melt into account) then mean heat loss due to throughflow would be about $25 \text{ W}\cdot\text{m}^{-2}$ for the period between 15 July and 31 August 1998.

The estimated effects of the sediment heat exchange and the energy loss due to throughflow of water were combined for the period from 15 July to 31 August 1998. These previously neglected heat fluxes add up to about $40 \text{ W}\cdot\text{m}^{-2}$ over the specified time period. This comes quite close to the mean deviation of $45 \text{ W}\cdot\text{m}^{-2}$ between the calculated and the measured heat flux. The mean deviation after August 1998 is around $7 \text{ W}\cdot\text{m}^{-2}$. Similar patterns can be observed for the years 1996 and 1997, with a larger deviation after ice break-up and average deviations around zero in September and October. This implies that the heat fluxes mentioned above are close to zero in the months of September and October. Because the lake is already at or past its highest heat content, the sediment heat flux will become zero or negative as water temperatures decrease. Also, the temperature difference between inflowing subsurface water and surface water is close to zero after 15 September (Figure 5.8), reducing the heat flux from subsurface inflow substantially. Glacier melt ceases in the middle of September due to reduced radiation input (see chapter 4.2.1), thus the cold subsurface inflow disappears. The temperature difference between the surface stream and the lake surface water increases slightly, but because precipitation usually falls as snow after 15 September the inflow volume and therefore also the heat loss decrease.

5.4 Temperature profile analysis of Jöri Lake III

5.4.1 Introduction

The physics of stratification development are the same in all lakes, whether in the mountains or in the lowland, whether in large lakes or small ones. However, due to the varying fractions of the heat fluxes in the various lakes, the evolution and the decay of the stratification is different from lake to lake. Since stratification is a determinant for the ecosystem, its condition is important for the evaluation of biota growth and possibly composition. The stratification processes unique for turbid glacial Lake III will be discussed in this chapter.

The heat exchange between a lake and the atmosphere takes place at the lake surface for the greater part of the heat flux components. The sediment heat exchange affects the water temperature at the bottom of the lake first. Inflow of water changes the temperature profile above the depth where it settles according to its density. For cold water this is at the bottom. For water warmer than the lake surface temperature the temperature profile is only altered in the topmost centimeters. The penetration of global radiation into the lake depends on the turbidity of the water (see chapter 4.3.5). The radiation attenuation leads to an exponential decrease in lake temperature towards the bottom of the lake if the profile is not disturbed by wind energy input. Wind forcing mixes the warmer surface water with cooler water below the surface causing an isothermal layer. The thickness of this layer depends on the wind forcing. An isothermal layer can also be built up by cooling of the surface water, i.e. when H_{tot} is negative.

5.4.2 Case studies

Four different cases of stratification development were analyzed to better illustrate the theoretical processes described above. A combination of the mixing due to surface cooling and due to wind forcing is shown in Figure 5.10b. On 4 September 1996 Lake III was still slightly stratified with a mixing depth of 5 m to 6 m and a strong thermocline between 6 m and 8 m depth. Subsequent cooling in the following days led to a small lowering of the mixing depth to 6 m and then to a complete collapse of the stratification on 8 September. A thoroughly mixed layer reaching down to a depth of 10 m evolved on this date. Warmer epilimnion water was mixed with colder hypolimnion water, producing water with a temperature between the two. So while the epilimnion cooled down during this mixing process, the hypolimnion actually heated up. Generally, mixing processes in a lake leading to a lowering of the isothermal layer involve cooling of the upper layers and heating of the lower layers. The total heat content of the newly mixed layer usually decreases because the mixing process is usually associated with a negative H_{tot} . Because a lower surface water temperature causes less heat loss to the atmosphere, a thorough mixing actually reduces the heat flux at the water-air interface.

Figure 5.10c shows the initial heating of the Lake III water column right after the ice break-up between 15 July and 21 July 1998. The closer the layer to the surface the more rapid the heating. Because initial lake surface temperature was close to 4° C, the heat loss from convection and longwave radiation emission was limited. As the surface water temperature of the lake increased, the mentioned fluxes became more and more negative, reducing the heat gain. Therefore, for equal meteorological conditions more heat is transferred into a lake, when surface water temperature is low. The exponential decay of global radiation due to attenuation is visible. Its effect is the

decreasing temperature rise with depth in the lake. At a depth of 8 m and below, the effect of global radiation on the water temperature ceases at this time.

The case between 27 August and 4 September 1998 (Figure 5.10a) is a combination of cases b and c in Figure 5.10. On 29 August a strong cold front with snowfall cooled down Lake III. Warm and clear weather returned on 31 August. A detailed description of this event including implications for biota is given by Hinder et al. (1999). The large heat loss between 27 and 29 August caused the epilimnion to cool down by 3.5 K. It increased in thickness from 2 m to 3 m during the same period. After 29 August the stratification was too weak to hold up against the wind mixing. Without further heat loss, the epilimnion mixed with hypolimnetic water causing a temperature decrease in the epilimnion and a temperature increase at 4 m and below. The depth of the mixed layer on 31 August was difficult to determine because of the small temperature gradients, it was around 5 m. High global radiation input during the first days of September caused the epilimnion to become thinner again, back to 2 m to 3 m. Although surface temperature on 2 September was 2° C less than on 27 August, the same heat content was calculated for both days. A cold front in early summer can therefore lead to an increase in lake heat content because it favors the transport of heat towards greater depths through mixing processes. If air temperature and global radiation return to high values after the cold front then lake water surface temperature will return to similar values like before the front. Therefore, with similar surface temperature, but higher hypolimnion temperature, the heat content of the lake will be higher after a cold front.

Figure 5.10d shows the transition from a positive stratification to a reversed stratification. As cooling of the lake intensified in September and October of 1997, the LSWT decreased to values similar to those at the bottom of the lake eliminating stratification. In Figure 5.10d the lake is isothermal at 4.9° C on 14 October 1997. Cooling persisted after isothermal conditions were attained and the lake remained completely mixed until the mean water temperature was just below 4° C. As lake surface water cooled down below 4° C, the cold surface water stayed at the surface due to its lower density. If wind forcing is small and cooling is strong, then a temperature inversion builds up with temperatures at the surface being lower than the temperature at the bottom of the lake, like on 27 October 1997. The surface cooling eventually leads to temperatures of 0° C and to the build-up of ice, which in the case of 1997 happened around 31 October.

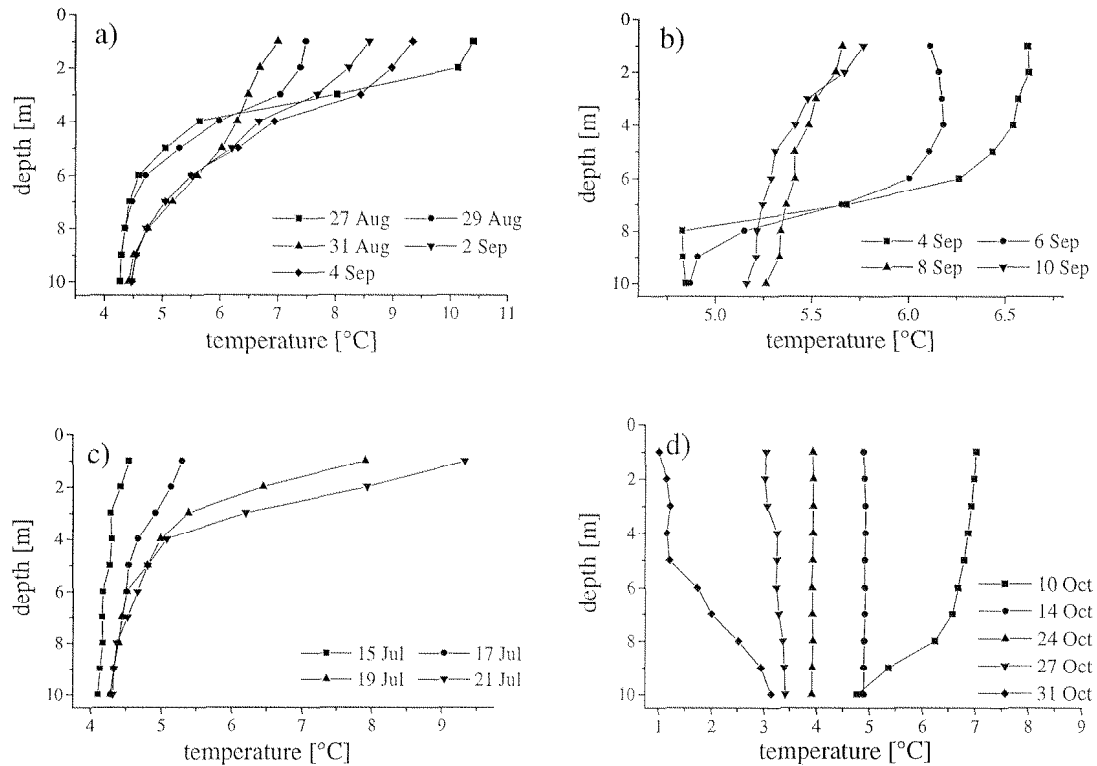


Figure 5.10a-d: Case studies of the stratification development in Lake III in the years 1996 to 1998. Case a): Passing of a cold front with subsequent strong heating of the lake between 27 August and 4 September 1997. Case b): Loss of the stratification due to surface cooling and wind mixing of Lake III between 4 September and 10 September 1996. Case c): Initial warming of the lake's surface layer right after the break-up of the lake ice from 15 July to 21 July 1998. Case d): Transition from a positive to a reversed stratification before final freeze-over of Lake III between 10 October and 31 October 1997.

5.4.3 Comparison of stratification between years

In Figure 5.11a-d the summer temperature profile developments in Lake III are displayed for the years 1996 through 1999 at depths of 1 m, 3 m, 5 m and 10 m. The data set is only complete for the period between August 5 and 27 for all four years. The development of the stratification is a constant mix between the processes described in the case studies above. The temperature profiles are highly variable between the years because they are dependent on the duration of ice cover and the meteorological conditions afterwards. In 1996 Lake III had been ice-free for about a month before temperature profiles measurements were made. For this reason the stratification was already well established by the end of July 1996. The temperature profiles are diverse in the beginning of August. In 1996, a strong stratification had already built up at this time. In 1997 the lake ice had just melted in the first days of August. In 1998 a strong stratification is visible in the top 5 meters. Below 5 m Lake III was essentially isothermal. In 1999, the lake was still completely isothermal and not free of ice at the

beginning of August, with temperatures being below 4° C throughout the lake. The heating rate of the water at 1 m depth is completely different between 1998 and 1999. While in 1998 the water at this depth needed only 8 days to heat up from 4° C to 9° C, in 1999 this heat-up process took 22 days. One reason for this is the lower global radiation input in 1999 than in 1998 during this heat-up phase. The second reason are the small ice floes from the avalanche (see chapter 6.3.1) still present on Lake III during 10 days of the heating period, therefore slowing the heat gain in 1999.

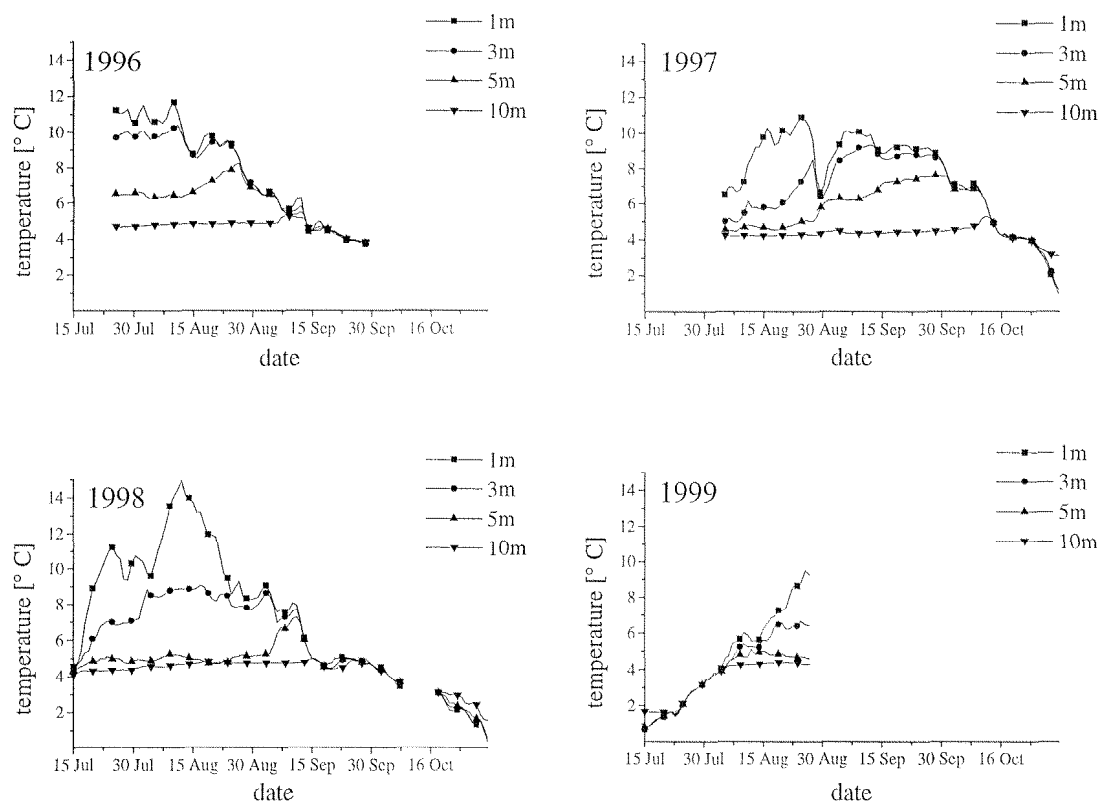


Figure 5.11: Development of the stratification in the years 1996 to 1999 for the periods from 15 July to 31 October. Only the data from the depths of 1 m, 3 m, 5 m and 10 m are plotted.

From 1996 through 1998 cold fronts at the end of August cooled down the lake substantially. Due to massive energy input in early September 1997, the effects of the cold front on surface water temperature were small in that year (see case Figure 5.10a). In 1996 and 1998 the cooling at the beginning of September caused a strong deepening of the mixed layer, leading to an epilimnion of 4 m depth in 1998 and about 6 m in 1996. In the latter two years the stratification did not recover due to unfavorable meteorological conditions. The stratification in 1997 persisted for another few weeks due to warm and clear weather in September. Lake III became isothermal on 8 September 1996, 13 October 1997 and 15 September 1998.

5.4.4 Winter lake temperature

As an ice cover builds up on a lake and snow falls on the ice cover, the heat fluxes through the surface of the lake become small. Snow and ice have a buffering effect between the water and the air (Rogers et al., 1996). Because stream inflow temperature is 0° C just like the outflow temperature, the heat flux from throughflow becomes 0 W·m⁻² as well. Only the sediment heat flux is still large enough to be of importance.

A slight temperature increase in 3 m depth and below from 1 November to 20 December 1997 (Figure 5.12) is assumed to be associated with the sediment heat flux. The same effect was observed throughout most of the ice cover period in 1998 (Figure 5.13), but with a larger temperature increase due to a higher temperature gradient. The decrease of temperature in 1 m depth during the same period in 1997 and 1998 is due to the thickening of the ice layer, causing the underside of the ice to become closer to 1 m depth. On 20 December 1997 large fluctuations in lake temperature were measured (Figure 5.12). Within just 3 hours on that day an intensive mixing process took place. There is no indication as to where the energy for the mixing came from. It is not clear whether cracking of the ice after a heavy snowfall or the release of a water pocket in the ground next to the lake could have caused the temperature disturbances measured.

On 10 May 1998 and 3 May 1999 water temperatures at all depths started to decrease due to the inflow of snow meltwater (Figure 5.12 and Figure 5.13). Although there should not have been a heat flux due to the throughflow of water, both inflow and outflow temperature being 0° C, an accelerating temperature drop was observed from 10 May to 8 June 1998 and from 3 May to 4 June 1999 for all depths. A similar cooling at all depths was observed by Bilello (1968) during the decay of the lake ice cover. It is probable that the large amounts of water flowing close to the surface from the inflow point to the outflow point of the lake caused lower lying water to flow in the same direction, but with a lower velocity. As a result, there would have been an updraft of water near the inflow and a downdraft near the outflow (Figure 5.14). Because the surface water was always 0° C due to the ice cover and the cold inflow water, the mixing process led to lower temperatures in the depth.

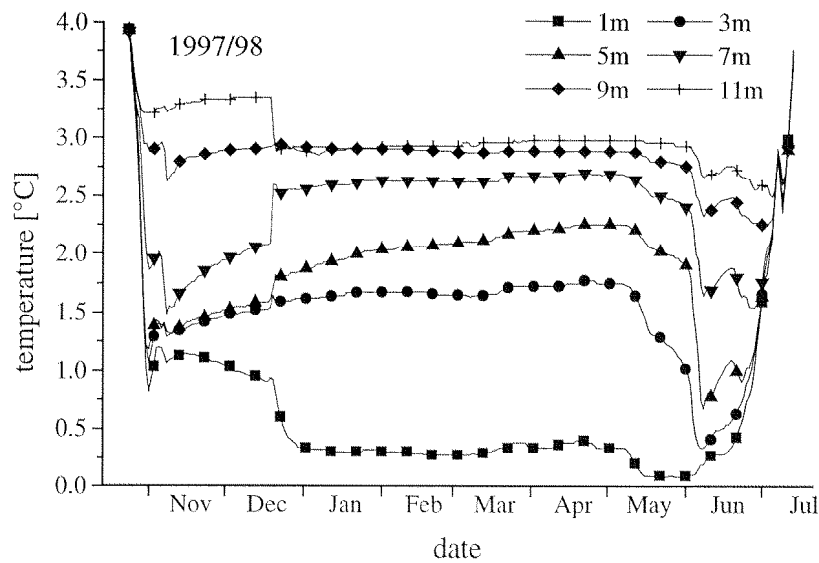


Figure 5.12: Temperatures in Lake III at 6 different depths (1 m, 3 m, 5 m, 7 m, 9 m, and 11 m) from 24 October 1997 to 13 July 1998.

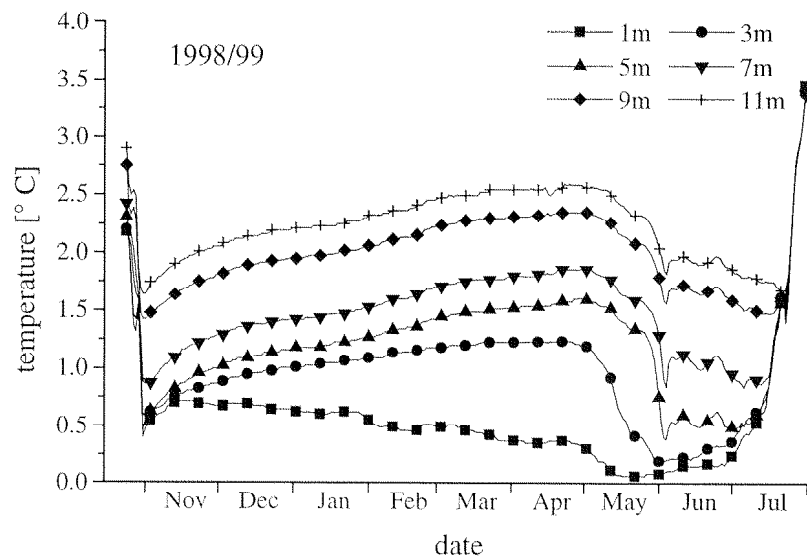


Figure 5.13: Temperatures in Lake III at 6 different depths (1 m, 3 m, 5 m, 7 m, 9 m, and 11 m) from 24 October 1998 to 4 August 1999.

The trend towards lower temperature in greater depths stopped abruptly on 8 June 1998, due to a cold front reducing the inflow volume substantially. Due to the much higher initial snow water equivalent in 1999, temperatures remained at a low level until the beginning of July of that year. As the snow on the ice cover started to melt, more and more global radiation entered the lake, heating up the surface water until it reached the temperature of the bottom water. Once the lake became isothermal, all the

heat fluxes into the lake were needed to melt the ice. Once the ice had mostly disappeared (ice cover $\cong 5\%$), the lake temperature started to rise in both years (Figure 5.10c) causing a positive stratification.

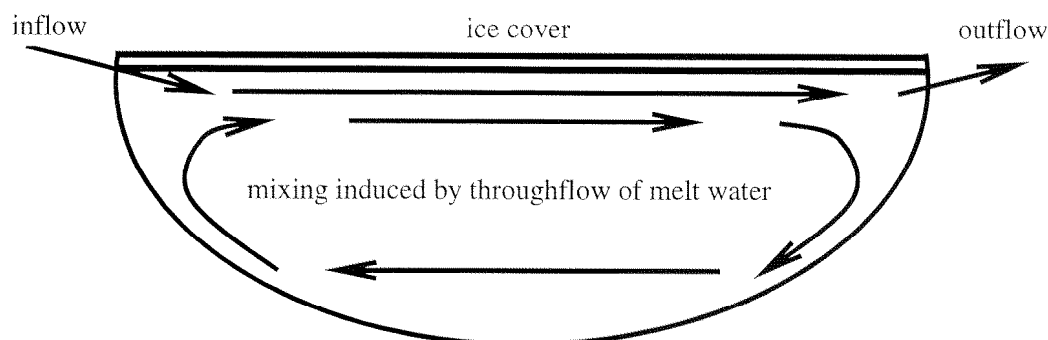


Figure 5.14: Scheme of possible mixing processes in a lake with an ice cover during the snow melt phase.

5.4.5 Effects of throughflow during the summer

Aside from having an effect on the heat content, inflowing of cold water also changes the temperature profile in a lake during summer. If water of a temperature below 4°C flows into a warm, stratified lake then a kind of mixing takes place that can usually not be observed in lowland lakes. The inflowing water is less dense than the heaviest water at the bottom of the lake. Therefore it will flow into the lake layer with a similar density, which would be into a layer of 7°C for inflowing water of 1°C . This is of course not where the water of 1°C will stay because it mixes with the warmer water to produce water of 4°C or more which will then move towards the bottom of the lake. The processes mentioned above do not take place one after another, but interact dynamically. The result is some downward and upward motion of water leading to turbulence and cooling in the meta- and hypolimnion. This turbulence may even be a source for internal waves.

The water flowing from Lake XIV into Lake III is rich in particles and therefore usually heavier than clear water with a temperature of 4°C . This would be the case for subsurface inflow temperatures of 2°C to 6°C , assuming a particle concentration of $60\text{ mg}\cdot\text{l}^{-1}$ (Theis, 1999) and a density of the particles of $2.5\text{ g}\cdot\text{cm}^{-3}$. However, the particle concentration in the hypolimnion of Lake III is already high, reducing the density difference between lake water and inflow water substantially. Since particle concentrations are usually small above the hypolimnion (see chapter 4.3.3) the inflowing water will flow to the hypolimnion due to its higher density, possibly even all the way to the bottom of the lake.

A steady inflow of $50 \text{ l}\cdot\text{s}^{-1}$ to the hypolimnion can lift the water surface of Lake III by more than 1 m during the 14 days from 7 to 21 August 1998. The warmest water at the surface is lost in this process. Below the water surface the water is constantly lifted with a rate of about $3 \text{ mm}\cdot\text{h}^{-1}$. This may not seem much, but in the thermocline, where gradients of $3 \text{ K}\cdot\text{m}^{-1}$ are not uncommon, this leads to an hourly cooling of 0.01 K due to the lifted water column. In depths between 3 m and 5 m this cooling effect is visible between 7 August and 21 August 1998 (Figure 5.15). Temperatures were lower on 21 August than on 7 August in the depths stated, while above and below the temperatures remained constant or even rose. This happened, although the prevailing temperature gradients between 2 m and 6 m would have caused water temperatures between 3 m and 5 m to rise without the lifting of the whole water column. Below 5 m the temperature was already in the range of the inflow water temperature and therefore could not decrease any further. At a depth of 2.5 m there is a subsurface outflow which eliminates most or all of the uplifted water, leaving the temperature profile above 2.5 m virtually untouched by the cold inflowing water from Lake XIV.

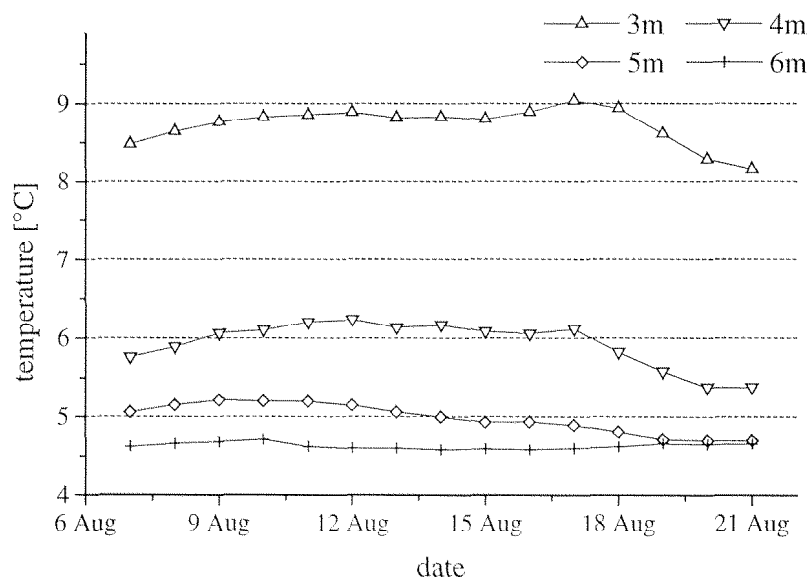


Figure 5.15: Water temperatures in Lake III at depths between 3 m and 6 m from 7 to 21 August 1998.

5.5 Heterogeneity of lake surface water temperature

5.5.1 Introduction

Information on variations in water temperature in remote lakes is usually scarce, since temperature profiles are not measured regularly (Livingstone and Lotter, 1998). Calculation of water temperature in remote lakes with the data from close lying AWS

would be practical. In Switzerland, some meteorological stations are situated in remote mountain areas, therefore possibly allowing the calculation of LSWT even in remote lakes, if the AWS data represent the conditions prevailing at the lake in question sufficiently. It was evaluated, whether LSWT in the small Jöri catchment is different from lake to lake and if it is, which processes are important for these deviations between the lakes. The calculation of LSWT in the Jöri catchment was then evaluated and the results compared to the observed values.

5.5.2 Measurement methods

The surface temperature of 8 lakes was measured in the period between 25 June to 15 October 1998. In addition to the six largest Jöri lakes (Lakes I, III, VII, X, XII, and XIII), two other lakes (Rundseeli and Schottensee) located just outside the Jöri catchment were included in this study. The surroundings of the latter two lakes are similar to those of the Jöri lakes with the exception of the exposition of their catchments. Rundseeli lies about 0.5 km from the western border of the Jöri catchment, its catchment facing southeast. Schottensee lies right on the Flüela pass, about 2.5 km southwest of the Jöri catchment. LSWTs were measured automatically at half-hourly intervals using small "Minilog" thermistors (Vemco Ltd., Shad Bay, Nova Scotia, Canada). The thermistors, wrapped in white tape to prevent possible radiative heating, were suspended from small buoys, so that the actual water temperature measured was that at a depth of 12 cm. The results of a former study in high-altitude Swiss lakes (Livingstone et al., 1999) suggests that water temperatures measured at this depth are likely to be fairly representative of temperatures prevailing in the epilimnion. The buoys were anchored close to the outflow of each lake, ensuring a continual flow of epilimnetic water past them, and at depths only slightly greater than 1 m, so they could be reached easily without a boat. With the exception of Lake III, where buoy malfunction caused the loss of the first 25 days of data, all sensors functioned correctly throughout the measuring period. The thermistors were installed on 25 June 1998, when all the lakes were still at least partly ice-covered. They were removed on 15 October 1998, when the surface temperatures of all lakes were below 4° C and some lakes were already partly ice-covered. After deployment, the resolution of the thermistors was checked and found to lie within $\pm 0.15^\circ$ C over the whole range of temperatures encountered.

5.5.3 Lake surface water temperature data and interpretation

Based on the half-hourly LSWT measurements, daily mean LSWTs in each of the eight lakes was calculated from 25 June to 15 October 1998. The mean LSWT over all eight lakes was then calculated (Figure 5.16), allowing the deviations of the LSWT

in each lake from this overall mean to be determined (Figure 5.17a-h). The overall mean LSWT shows a steep increase in the lakes towards equilibrium temperature in the middle of July. Other distinct features of Figure 5.16 are a warm weather period in mid August leading to a seasonal maximum in LSWT mean and a strong cold front decreasing the LSWT mean by more than 4 K in mid September.

The greatest differences in LSWT occurred in the month of July, especially in the first half (Figure 5.17a-h). At this time, some of the lakes were already free of ice and others still completely ice-covered. Completely ice-covered lakes have a surface temperature of 0° C while the surface temperature of shallow lakes where the ice has melted can rise 5 K in just 3 days (Rundseeli in late June 1998). The temperature difference between Lake XIII and Rundseeli is at times more than 10 K in the time between the break-up of Rundseeli and Lake XIII. The ice coverage of all lakes was observed on four occasions from 25 June to 20 July. On 25 June, all of the lakes were still at least partly ice-covered, while on 2 July Schottensee and Rundseeli were free of ice. By 13 July, only Lakes III, VII and XIII were still partly covered by ice. All the lakes were totally ice-free on 20 July (Table 6.1).

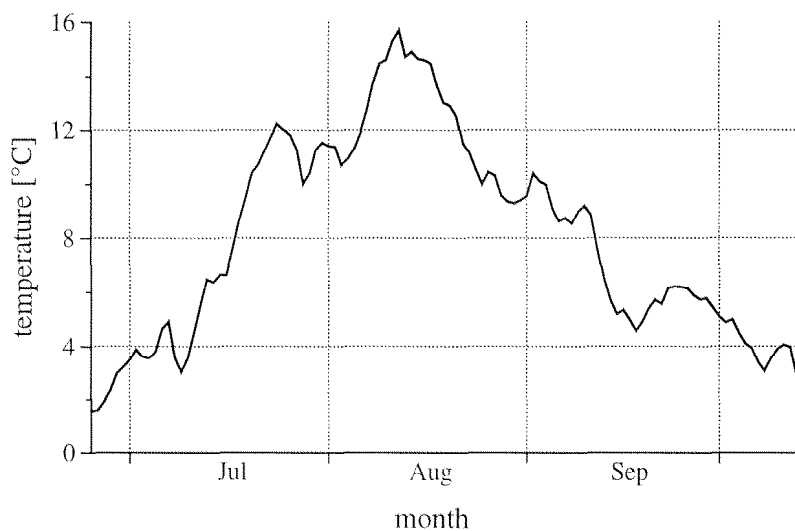


Figure 5.16: Mean lake temperature of all 8 lakes where LSWT was measured in 1998 from 25 June to 15 October.

After the last lake, Lake XIII, broke up on 18 July 1998, the LSWTs of all lakes behaved similarly with only small deviations (<3 K) from the overall mean. These differences in LSWT must be associated to differences in the meteorological forcing or other factors important for lake heat exchange (throughflow, sediment heat flux).

In late July and early August, Rundseeli is still clearly warmer than all the other lakes. The differences between the morphologically similar lakes XII and Rundseeli of 2 K to 4 K cannot solely be attributed to different meteorological forcing. The

differences probably arise from the different fractions of snow in a catchment at the end of July and beginning of August 1998. If the fraction of snow in the catchment is high, then the amount of cold water flowing into a lake will be high as well, therefore significantly cooling the lake. It is therefore important to know which factors influence snowmelt in a catchment.

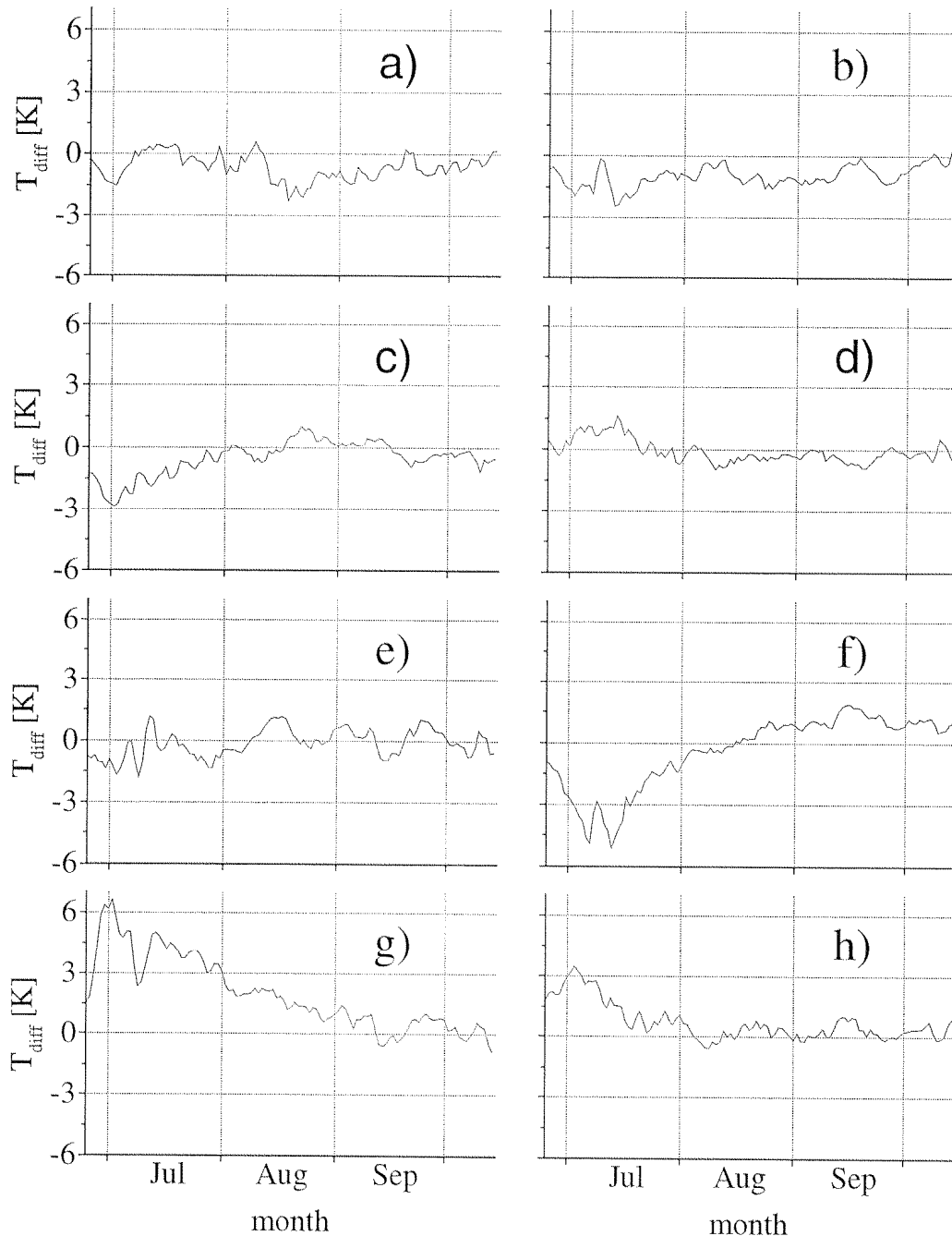


Figure 5.17: LSWT difference for each lake from the mean LSWT (Figure 5.16) for the period 25 June to 15 October 1998. a) Lake I, b) Lake III, c) Lake VII, d) Lake X, e) Lake XII, f) Lake XIII, g) Rundseeli, h) Schottensee.

Only two indicators for snowmelt energy input to each catchment were calculated. These are the mean catchment altitude and the mean clear sky radiation from May to July (Table 5.3). The mean catchment altitude is important because it is an indicator for mean air temperature in the catchment, assuming a constant lapse within the study area. For the lakes in the Jöri catchment these values were calculated from the DEM, for Rundseeli and Schottensee they were estimated but should still be accurate to within ± 20 m for mean altitude and $\pm 10 \text{ W}\cdot\text{m}^{-2}$ for mean radiation. Rundseeli clearly has the highest mean catchment radiation, most of it facing southwest. Only Schottensee has a clearly lower mean catchment altitude, but a much lower catchment radiation as well. From these indicators it was assumed, that the snow in the catchment of Rundseeli melts before it does in all the other catchments.

| Lake numeral | mean catchment altitude [m] | mean catchment clear sky radiation May - July [W·m ⁻²] | V/C ratio [m] |
|------------------|-----------------------------------|--------------------------------------------------------------------------|---------------------|
| I | 2640 | 319 | 0.12 |
| III | 2630 | 321 | 0.48 |
| VII | 2620 | 329 | 0.24 |
| X | 2600 | 307 | 0.16 |
| XII | 2660 | 324 | 0.04 |
| XIII | 2690 | 324 | 0.36 |
| Rundseeli (Rs) | 2620 ^a | 360 ^a | 0.04 ^a |
| Schottensee (Ss) | 2500 ^a | 280 ^a | 0.6 ^a |

Table 5.3: Catchment indices of all 8 lakes where LSWT was measured in 1998. The values were calculated using the DEM. V/C is the volume to catchment ratio.

^a) estimated values

From the middle of August onwards, LSWTs in Lakes I and III were clearly lower than in the other lakes. Lakes I and III are exceptional in that they are the only large lakes in the study area that are partially fed by glacial meltwater (see chapter 4.2.2). Depending on the prevailing weather conditions and on the seasonal state of the catchment, the proportion of cold glacial meltwater entering these lakes can vary between 0 % and 80 %. Assuming the throughflow rate to be sufficient, it is evident that inflowing glacial meltwater with a temperature only slightly in excess of 0° C will tend to depress the LSWT possibly for the whole open-water period. The higher albedo also led to a lower heat input through global radiation (see chapter 4.3.4), which further explains the lower LSWTs in Lakes I and III. The extent to which a cold inflow has an effect on LSWT is determined by the volume to catchment ratio V/C (Table 5.3), the

surface temperature of the lake and the inflow temperature. The ratio of volume to catchment area (V/C) is an indicator of how quickly the water of a lake may be exchanged. A low V/C ratio favors a faster heat loss than a high V/C ratio because then inflowing water makes up a larger percentage of the water already in the lake.

| Lake | heat surplus 20 Aug [MJ·m ⁻²] | heat surplus 7 Sep [MJ·m ⁻²] | heat surplus reduced to 0 MJ·m ⁻² |
|------------------|----------------------------------------------|---------------------------------------------|-------------------------------------------------|
| I | 59 | 37 | 17 Sep |
| III | 65 | 50 | 5 Oct |
| VII | 91 | 48 | 19 Sep |
| X | 56 | 31 | 17 Sep |
| XII | 41 | n.a. | 15 Sep |
| XIII | 91 | n.a. | 9 Oct |
| Rundseeli (Rs) | 42 | n.a. | 18 Sep |
| Schottensee (Ss) | 114 | n.a. | 6 Oct |

Table 5.4: Heat surpluses compared to 4° C isothermal conditions on 20 August 1998 and 7 September 1998, based on profile measurements. The last column states the date in 1998 at which each lake reached 4° C and isothermal conditions. (n.a. = data not available)

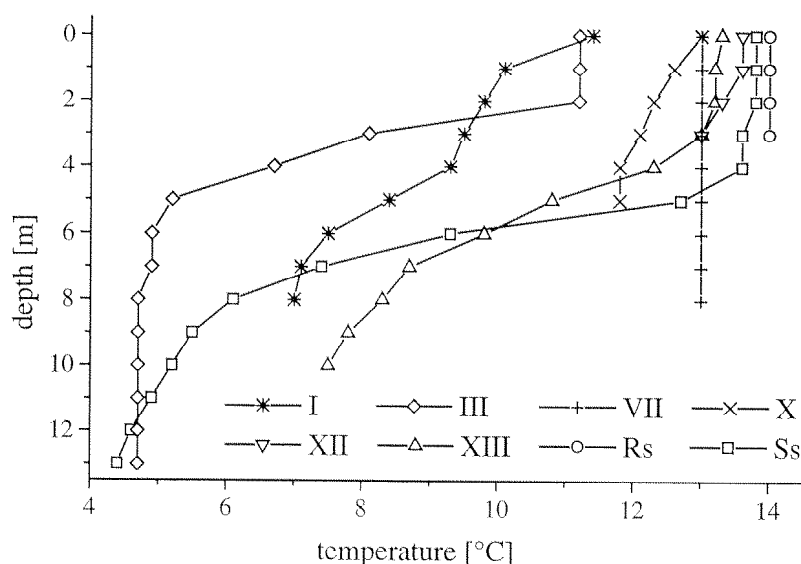


Figure 5.18: Temperature profiles on 20 August 1998 in the 8 lakes, where LSWT was measured in that year. Temperature below 13 m in Lake III was equal to that in 13 m depth and thus was not plotted.

Temperature profiles were measured in all 8 study lakes on 20 August and in four of them on 7 September (Figure 5.18, Table 5.4). The heat surplus per m² of each

lake compared to fall isothermal conditions (4°C) was calculated (Table 5.4). Because the bathymetry was only known for Lake III, the calculations for the other lakes were based on their maximum depths, assuming a bathymetry similar to lake III. Also, the date at which 4°C isothermal conditions were attained was evaluated for each lake. This is equivalent to the date at which the heat surplus dropped to $0\text{ MJ}\cdot\text{m}^{-2}$. Schottensee had the largest heat surplus on 20 August, followed by Lake VII and XIII. Evidentially, there is a clear tendency for higher energy surpluses in deeper lakes. This dependence falls somewhat short in Lakes I and III. There is a sharp decrease in heat surplus from August 20 to September 7 in Lake VII, almost half of the surplus is lost in these 18 days. In Lake III the energy loss is much smaller during the same time span.

On 12 September 1998 a cold front hitting the Swiss Alps resulted in a decrease in LSWT at the study sites by up to 6 K within a few days (Figure 5.16). The temperature drop was most dramatic in shallow lakes (Lake XII and Rundseeli). Immediately after the passing of the cold front on 12 September, Lake XIII had the highest LSWT, followed by Schottensee. Only these two lakes and Lake III saved some of their energy surplus into the month of October (Table 5.4). Most lakes totally lost their heat surplus within the week after the cold front, with Lake VII once again standing out with its rapid loss of energy. There are a few reasons why Schottensee and Lake XIII have the highest LSWT after the cold front on 12 September 1998. Lake XIII and Schottensee are the deepest lakes in the study, aside from Lake III and can therefore store more heat per area by default. Both these lakes are rather clear without glacier particle input. Global radiation penetrates deep into these lakes, also allowing water in greater depths to heat up. Higher temperatures in the meta- and hypolimnion are stored until epilimnion temperature falls below these temperatures. Because of the high erosion particle input to Lakes I and III solar heat input to these lakes is absorbed mainly in the uppermost 1 m ($>99\%$ and 75% in September 98 for Lakes I and III respectively), and is readily lost during the night if it is not mixed down to greater depths by strong winds. Also, albedo is higher in the lakes with higher turbidity, leading to a lower solar heat input. This causes lower energy surpluses in turbid lakes compared with clear lakes.

Schottensee lost its heat surplus faster than Lake XIII, although Schottensee had a higher heat surplus on 20 August and is lower in altitude. The heat loss rate is even higher in Lake VII. Latent and sensible heat loss increase proportional to wind speed. Lake VII and Schottensee situated at passes are most exposed to wind, so that even if the heat content of these two lakes were high before the passing of a cold front, they would be likely to lose more energy than a calmer lake like Lake X or XIII. Calmer lakes hold on to their energy contents better. A calm lake with a large initial energy surplus would reach fall isothermal conditions latest, which is true for lake XIII in 1998.

Wind speed also has an influence on diurnal variability of LSWT. The diurnal variability in LSWT was examined during the period from 6 to 12 August. Fine weather with high temperatures and cloudless skies prevailed during this period, resulting in a strong diurnal cycle in LSWT in most lakes (Figure 5.19). The seven-day mean temperature deviation from the value at sunrise (6:30 CET) was calculated on a half-hourly basis for each lake. Although all the lakes were exposed to similar radiative forcing, they showed great differences in diurnal LSWT variability. While LSWT only rises 1 K in Schottensee over the course of the day, maximum LSWT of Lake X lies 4.7 K above its minimum value at sunrise. There are two basic patterns of diurnal LSWT variation. The first one is a steady, sinusoidal increase of LSWT as a result of global radiation until the maximum temperature is reached between 15:30 CET (Lake III and X) and 17:30 CET (Lake XII), followed by a linear decrease. The second pattern is a slight increase of LSWT in the morning hours until 11 CET. Afterwards the temperature does not rise substantially anymore. The latter pattern is exhibited by Schottensee and Lake VII while all the other lakes show the first pattern. The large heating at the lake surface is suppressed by wind forcing, mixing the warm surface water with colder water below the surface. This process is continuous as long as the wind forcing is strong enough which is the case for most of the day in Lake VII and Schottensee. The cooling process in the late afternoon and at night is dominated by longwave emission. Therefore, the warmest lakes will have the largest cooling rates, whereas lakes without a large diurnal temperature variation do not lose much heat during the night.

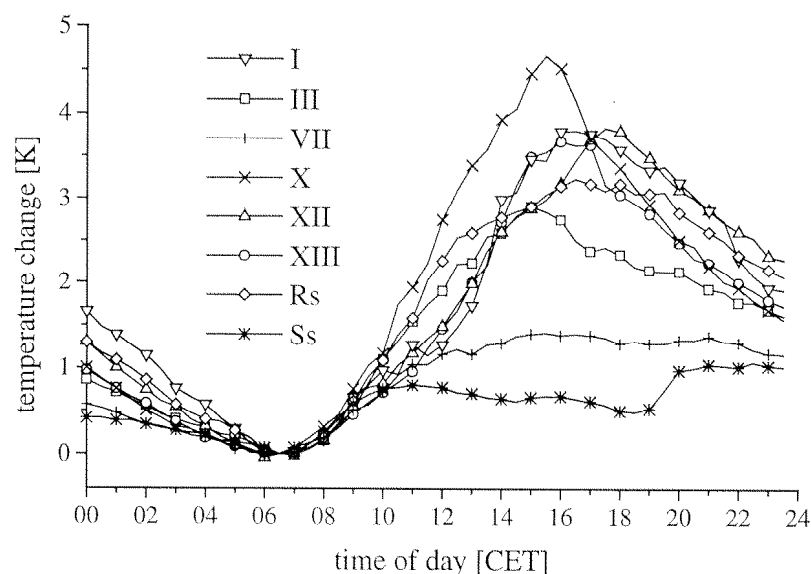


Figure 5.19: Mean diel LSWT variation between 6 and 12 August 1998. The temperatures at 6:30 CET were taken as a reference for each lake and for all other times the difference to the value at 6:30 CET was calculated.

5.5.4 A model for lake surface water temperature calculations

One approach to calculate lake surface temperature is by means of the equilibrium temperature. The so-called equilibrium temperature T_{eq} is the surface temperature at which the net heat flux H_{tot} would be zero (Edinger et al., 1968). It would ultimately be reached by the water surface under stationary environmental conditions. It can be calculated iteratively by changing T_s in equations (5.2) to (5.10) until H_{tot} becomes $0 \text{ W}\cdot\text{m}^{-2}$. The rate of heat exchange between water and atmosphere is a function of the difference between the actual water temperature T_s and the equilibrium temperature T_{eq} . T_{eq} continually changes in response to varying meteorological conditions. The water temperature, in turn, is continually driven toward T_{eq} by the difference between the two. The rate at which T_s approaches T_{eq} is dependent on the mixing depth of the lake and a heat exchange coefficient A . A is defined as the negative partial derivative of the net heat flux H_{tot} with respect to the surface temperature T_s (Sweers, 1976; Livingstone, 1989):

$$A = \frac{\partial H_{tot}}{\partial T_s} \quad (5.12)$$

If the mixed layer z_{mix} is not infinitely thin, T_s cannot reach equilibrium temperature instantaneously. Under stationary conditions the temperature of the mixed layer z_{mix} tends to approach T_{eq} exponentially:

$$T_s(t) = [T_s(0) - T_{eq}] \cdot e^{-kt} + T_{eq} \quad (5.13)$$

where k is the exchange rate:

$$k = \frac{A}{c_p \cdot \rho \cdot z_{mix}} \quad (5.14)$$

If an automatic weather station is situated next to a lake, then it is quite easy to calculate H_{tot} and therefore also T_{eq} , as well as A . The only problem in the calculation of T_s arises from the fact that z_{mix} is not known, if no lake temperature profile measurements are made. In shallow lakes it can be assumed that z_{mix} is always equal to the mean depth of the lake and therefore the calculation of T_s should be quite accurate. For deeper lakes the mixing depth is variable and it has to be estimated based on experience, taking into account turbidity and wind conditions at a lake. However, if

there is absolutely no knowledge of one of these factors, large errors have to be expected in the calculation of lake surface temperature.

For each of the 8 lakes, where LSWT was measured in summer 1998, LSWT was also calculated according to the formulae above. The meteorological conditions prevailing at each lake were mostly estimated due to lacking observations. If the model calculations were correct and the meteorological variables could be determined accurately, then the measured and calculated LSWTs should not differ.

5.5.5 Application of the model

For the calculations of LSWT it is a prerequisite that the meteorological conditions be known at the lake in question. However, in 1998 complete meteorological measurements were only recorded at Lake III. For the other lakes the values from Lake III and in part from nearby AWSs outside the Jöri catchment (see chapter 3) had to be adapted to fit the conditions prevailing at each lake. This was done using data from previous years (Lakes VII and X), from calculations (global radiation) or from personal observations (wind speed, albedo). The range of errors arising from these adaptations of meteorological measurements cannot be quantified exactly.

Humidity and incoming longwave radiation were considered to be homogeneous throughout the catchment for the calculations. Mean global radiation for each lake was calculated according to the method described in chapter 3.7.3. The meteorological adaptations made solely by adding or multiplying with a constant over the whole open-water period are not a highly scientific approach, but they can be implemented into the calculations easily and it was the only available procedure for the limited data and observations existing for most lakes. The errors associated with these assumptions may be large on a daily basis, but over longer periods of time they should cancel. Albedo was set to increase over the year from 0.06 in June to 0.09 in October (Kondratyev, 1973) in lakes without glacier particle input. For shallow lakes the albedo was increased by a constant value due to the radiation reflection at the bottom of these lakes (Marti and Imboden, 1986). In Lakes I and III where suspended erosion particles play an important role, albedo was set to vary over the open-water period according to observations and measurements (see chapter 4.3.4). Air temperature at each lake was calculated based on a mean summer lapse rate of $6.5 \text{ K} \cdot \text{km}^{-1}$ common at these altitudes. A constant was added to the air temperature for lakes that are not situated in a distinct valley, but at the side of the valley (see chapter 3.4.2). Wind speed adaptations for each lake were made based on a constant factor over the calculation period. Only limited measurements and observations were available to estimate the wind multiplying factor.

To keep the epilimnion evolution as simple as possible, only two different depths z_{mix} were used in the calculations for each lake. The first one was used until

12 September 1998. On this date a strong cold front destroyed the stratification that existed in the four deepest lakes. After 12 September all lakes were assumed to be completely mixed and the mixing depth was set equal to the mean depth of the lake. The four shallowest lakes were assumed to be thoroughly mixed throughout the open-water period. The mean depth of the epilimnion for the period until 12 September was estimated based on temperature profiles made in all lakes on 20 August 1998 (Figure 5.18).

Table 5.5 gives an overview for the meteorological adjustments made at each lake. If the meteorological variables, the albedo and the stratification properties had been estimated and adjusted correctly for the lake in question, then the variance between the calculated LSWT and the measured LSWT should be small.

Aside from the calculations with the meteorological forcing individually adapted to each lake, calculations with equal meteorological forcing for all lakes were also made. In the latter calculations only air temperature was adapted to the different altitudes of the lakes according to a constant lapse rate of $6.5 \text{ K} \cdot \text{km}^{-1}$. The same depths of the epilimnion were used (Table 5.5). It was estimated that the break-up of a lake is usually delayed by a week for an altitude increase of 100 m. For each lake LSWT calculations were compared to the values observed. Also the calculations based on the standard meteorological measurements and those with the adjusted meteorology for each lake were compared to each other.

| Lake | Temperature addition | Wind speed multiplication | Albedo addition | mixing depth before and after 12 September |
|------|----------------------|---------------------------|-----------------|--------------------------------------------|
| I | 0 | 1 | variable | 1.5 m / 4 m |
| III | 0 | 1 | variable | 2 m / 8 m |
| VII | 0 | 1.2 | 0 | 4 m |
| X | 0 | 0.8 | 0.04 | 2.5 m |
| XII | 0.1 | 1 | 0.02 | 2 m |
| XIII | 0.1 | 0.75 | 0 | 3 m / 4.5 m |
| Rs | 0.3 | 0.9 | 0.02 | 1.8 m |
| Ss | -0.1 | 1.4 | 0 | 3 m / 6 m |

Table 5.5: Correction factors and constants for the adjusted meteorological conditions at each lake. The last column represents the chosen epilimnion depth before and after 12 September. For lakes with only one value, the epilimnion was assumed to be constant throughout the open-water period.

5.5.6 Results of the lake surface water temperature calculations

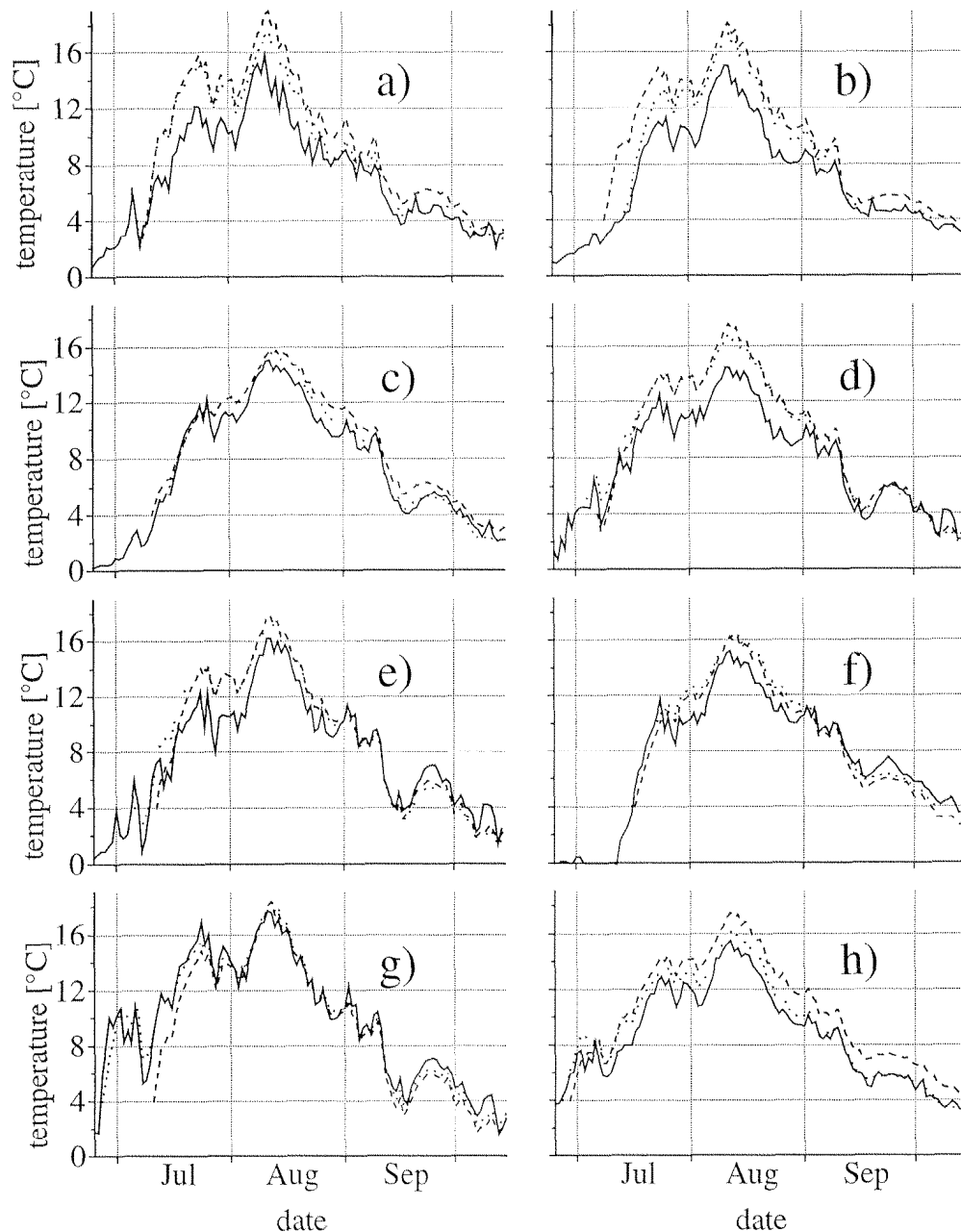


Figure 5.20: LSWT calculations for all 8 lakes, where LSWT was measured in 1998. a) Lake I b) Lake III c) Lake VII d) Lake X e) Lake XII f) Lake XIII g) Rundseeli h) Schottensee. The solid lines represent the observed LSWT. The values represented by the dashed lines were calculated with standard meteorological measurements, those depicting the dotted lines were calculated using adjusted meteorological data from each lake. The calculation period was from 25 June to 15 October.

The course of observed and calculated LSWT over the open-waters season was plotted in Figure 5.20a-h. The solid line depicts the observed LSWT, while the dashed

lines show the calculated LSWT with the standard meteorological measurements. The dotted lines show the calculated LSWT with the meteorological data adjusted for each lake. The differences between the dashed and the solid lines can be attributed to the unique meteorological forcing at each lake, i.e. if the depth of the epilimnion was chosen appropriately. At first sight, it seems that virtually all calculated LSWTs are higher than the measured ones Figure 5.20. This is most pronounced in July and August, but the magnitude is not the same at all lakes. Generally, the differences between the calculations with the different meteorological input variables are quite small. The largest differences can be found in those lakes, where the ice did not break up according to the altitude of the lake, as in Lake III and Rundseeli.

Differences between the two calculations with the differing meteorological input are often smaller than the differences between measured LSWT and calculated LSWT with adjusted meteorological forcing. This indicates that the meteorological adjustments made for each lake were not large enough or erroneous. When comparing the measured data with the calculated ones, good agreements can be observed after 12 September for all lakes. It is not a coincidence, that from this date on all lakes were assumed to be thoroughly mixed. In a completely mixed lake the depth of the epilimnion is a constant, while it can vary greatly when a stratification exists. In order to obtain better results for the calculations, the depth of the epilimnion would have to be adjusted in the model on a daily basis and not just once in a model run. This would require either daily temperature profiles in a lake or applying a one-dimensional lake model instead of the simplistic calculations of LSWT. If the first approach were applied, then modeling of LSWT would be useless, because daily LSWT could be measured easily together with the temperature profile. The application of a one-dimensional lake model also needs higher quality input variables than the LSWT model. One important variable for the one-dimensional model is the turbidity in different depths because it determines the percentage of global radiation absorbed at a certain level. Turbidity is also a variable which has a specific seasonal development for each lake and at different depths and would therefore also have to be measured for a lake to be modeled. Because the measurement of the input variables for the lake model are more complicated than the measurement of LSWT itself, applying a one-dimensional lake model is not feasible.

The deviations of the calculated LSWT from the measured LSWT are quite different from lake to lake in the month of July and August. There are also large deviations in shallow lakes considered to be mixed all through the open-water period (Lake X and XII). Therefore, it is unlikely that the imprecise determination of the epilimnetic depth causes all the deviations. Since the input variables for the LSWT model were the same as for the energy budget calculations of Lake III, heat fluxes from the sediment and throughflow were neglected. Because for most lakes no information is

available on the volume and temperature of the inflow, there was no possibility to include the heat flux from throughflow of water. Some or even most of the deviations before 12 September in Lake I and III can be attributed to the neglected throughflow of glacier meltwater. For the other lakes attributing the deviations to a defined cause is not possible.

For some lakes the LSWT model works exceptionally well. These include Lake VII, Schottensee and Rundseeli. For these lakes the differences between measured LSWT and calculated LSWT with the adjusted meteorology are less than ± 1 K for most of the open-water period. Lake VII and Schottensee are also special in that the adaptation of the meteorological forcing for these particular lakes brings the calculation much closer to the measured values than by just using standard meteorological conditions. These two lakes are the only ones studied, where wind speed is clearly larger than at Lake III (Table 5.5). High wind speeds not only increase the heat loss due to convection, they also keep up the mixing in the epilimnion. The variability of the mixing depth is assumed to be smaller in lakes where wind speeds are generally high, such as at a pass.

For the lakes in this study that have a large inflow of cold meltwater during their ice free period, the method of calculating surface temperature from the equilibrium temperature is unsuitable. Especially in the case of the lakes with glacier water inflows, the discrepancies are large during most of the season. In the case of deep lakes with changing stratification, calculation errors can be large because of the lack of knowledge of the mixing depth. This simple method of calculating LSWT is therefore mainly of use for shallow unstratified lakes with little meltwater inflow during the open-water period. It seems that reasonable results can also be obtained for larger lakes, if they are subject to constantly large wind forcing, thus keeping the mixing depth more or less constant.

5.6 Conclusions on heterogeneous water temperature

Based on the measurements and calculations of LSWT, as well as the temperature profiles in 8 different lakes, one can conclude that differences of water temperature between the lakes is largest below the surface and not at the surface itself. The factors leading to the small differences in LSWT and the large differences of mean lake temperature are clearly defined. The most important factors causing heterogeneity of water temperature in the lakes of a small catchment are catchment characteristics, lake depth, turbidity and wind.

Exposition and altitude are the main determinants of catchment characteristics. They play a major role for the snow meltwater production in spring and summer. Lake depth obviously is important for heat storage, deeper lakes tend to change mean

temperature more slowly than shallow lakes. Deep lakes tend to be stratified, whereas shallow lakes are isothermal throughout most of the open-water season. The differences in turbidity stem mostly from the suspended erosion particles in the lakes. In clear lakes portions of global radiation may reach the bottom, leading to a different stratification than for turbid lakes, where sometimes more than 99 % of global radiation is absorbed in the top few meters of the water column. Of all meteorological parameters, wind speed and direction is the most heterogeneous (see chapter 3.6.2). Because wind speed also plays an important role in energy budget calculations and for the mixing of lakes, it is evident that the heterogeneous wind speed distribution in a small catchment has implications on the water temperature differences between the lakes.

6 Ice cover processes

6.1 Introduction

Interest in lake ice has been spurred by both basic and applied considerations, including its role in the heat budget of lakes (Liston and Hall, 1995; Fang et al., 1996), importance to aquatic ecosystems (Magnuson et al., 1990), structural engineering and navigational implications, as well as a climate indicator (Livingstone, 1997; Vavrus et al., 1996; Stefan and Fang, 1997).

The formation of a continuous ice cover, and later a snow cover on the surface of a lake, greatly changes the conditions of heat exchange with the atmosphere. The heat loss from the water to the atmosphere is reduced by the insulating effect of the cover. As a result, the dynamic effect of atmospheric processes is almost completely eliminated. The remaining effect of these processes is the changing snow and ice cover thickness (Gu and Stefan, 1990).

An ice sheet covered by snow also prevents global radiation from entering the lake since most of it is absorbed in the snow cover. In addition to the low water temperatures in ice-covered lakes, organisms must also endure almost complete darkness for a great part of a year.

In this chapter, the processes leading to a continuous ice cover on a lake are described based on the literature and on observations. The applicability of two ice models to mountain lakes is evaluated. The decay of the ice surface is modeled using a new empirical degree-day model adjusted for snow height. The variability of the break-up date in the past 40 years is analyzed based on this model. Also the processes involved in the decay of the ice cover are described.

6.2 Ice build-up and development

In late summer and fall, a lake suffers a net loss of energy through radiative, sensible and latent heat fluxes at its surface. Initially this surface cooling results in a turnover of water as the denser cooler water ($\sim 4^\circ\text{C}$) from the surface descends to be replaced by less dense warmer water from below (see Figure 5.10d). Eventually, a situation arises in which less dense, cooler water ($< 4^\circ\text{C}$) lies at the surface which can, in the absence of mechanical turbulence by winds or currents, freeze despite the relatively warm water still existing below it. If the weather is very cold and there is little wind after the fall turnover, ice can already form at mean lake temperatures near 4°C (in 1996, see Figure 5.3). On the other hand, if it is windy during fall with air temperatures only slightly below 0°C , the entire water mass is cooled down before the lake finally freezes (in 1998, see Figure 5.3). After an ice-cover has been established,

the lake water continues to lose heat at its upper surface at a reduced rate by conduction through the insulating ice sheet. The ice thickens downward in response to this loss.

Snow falling onto the initial ice surface affects its evolution. A snow cover on an ice surface acts as an insulating blanket due to the lower thermal conductivity of snow compared to ice (Gray and Male, 1981). This further reduces heat loss from the lake to the atmosphere, slowing the downward thickening of the ice. Snow cover may promote ice growth if its weight depresses the surface below the hydrostatic water level. As the ice cover is depressed, its surface and the overlying snow will be flooded initiating a new phase in the evolution of ice cover. Water which moves through cracks in the ice rises by capillary action in the snow cover to a depth slightly above the depth of depression of the ice surface, thereby producing a layer of slush at the snow-ice interface (Gray and Male, 1981). Given continuous below-freezing air temperatures, which is usually the case in high mountains during the winter, the thinly insulated slush will freeze rapidly from its surface downwards, building a new white ice sheet above the black ice initially formed at the water-atmosphere interface. This process can repeat several times during an ice cover period, leading to the formation of several independent ice sheets parallel to each other.

6.2.1 Observations of ice cover on the Jöri Lakes

The surface conditions of several lakes in the Jöri catchment were observed during excursions to the Jöri Lakes in October and early November. Most observations were made on Lake III. The excursions took place about every two weeks during these months in the years 1996 through 1998. With this rather rough time resolution, the exact date of the final freeze-up of the lakes could only be estimated. The time of the complete freeze-up of Lake III could be narrowed down to between 29 October and 9 November in 1996, 21 October and 10 November in 1997 and 27 October and 6 November in 1998 (Figure 6.1). Despite the large uncertainties of the freeze-up dates and the lack of historical data, it can be assumed, that Lake III usually freezes between 15 October and 15 November. Due to the high horizon obstruction in November (Figure 2.5), Lake III even loses energy on clear days. Therefore, a freeze-up date later than 15 November is only possible if strong warm winds persist in late fall.

Lake III was generally one of the last lakes or the very last lake to completely freeze over. The first lakes to completely freeze over were the shallow lakes at higher altitudes (lakes with roman numerals between XIV and XXII). These were usually followed by Lakes X and XII, then I and VII and at last XIII and III. The order of lake-freezing was not the same for all years. However, this order was seldom changed. Lake III for example would never completely freeze over before Lake X. It was observed that all lakes usually partially freeze over and thaw several times before they become ice-

covered completely. A lake can also stay partially ice-covered for several weeks like Lake I in 1998, when a partial ice cover was first observed on 8 October and persisted throughout 27 October until it froze completely at the end of October. This is probably due to the heterogeneous meteorological values on a lake, which favors ice build-up in some parts of the lake, while energy inputs or wind induced turbulences are too high for freezing in other parts of the lake.

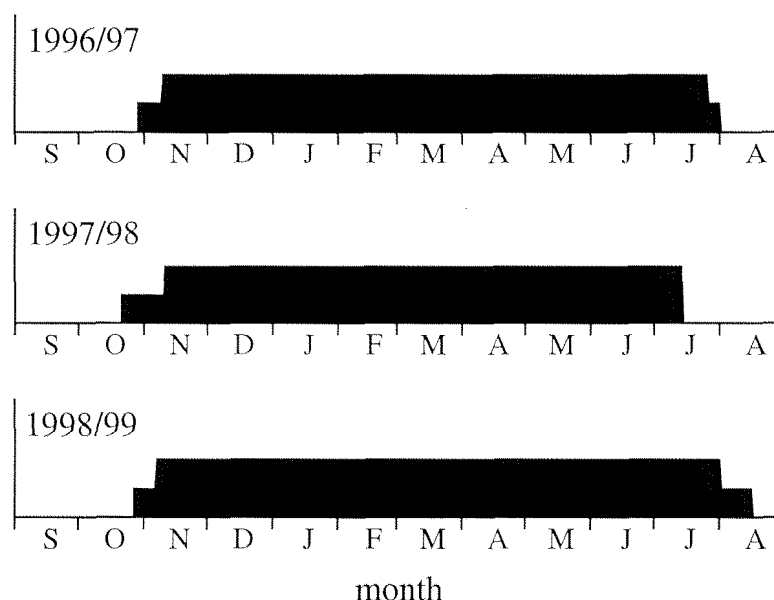


Figure 6.1: Ice-cover duration of Lake III from 1996 to 1999, September (S) to August (A). Half levels in fall indicate the uncertainty of the freeze-up date due to infrequent observations. Half levels in summer indicate times, when only avalanche ice masses were still on the lake.

An interesting observation was made on 8 October 1998, when ice covered about 50% of Lake III. In the days preceding this date, the daily average air temperature was never below -1°C and daily average wind speed was always above $4\text{ m}\cdot\text{s}^{-1}$. These are unfavorable conditions for ice formation, especially since volume-averaged lake temperature was only slightly below 4°C . Also no clear nights were registered during this time period. Therefore, the build-up of ice must have been initiated by heavy snowfalls on 7 October, which led to an accumulation of about 20 mm water equivalent of snow. For several hours on that day, 3 mm water equivalent of snow fell onto the lake hourly, causing an energy loss of $280\text{ W}\cdot\text{m}^{-2}$ in the periods of heavy snowfall. This is an extraordinarily large heat loss, which is only rarely reached even when all heat fluxes are included. Thus, heavy snowfall on a cold water surface can lead to a partial ice cover even if air temperature is not much below 0°C and volume-averaged water temperature is only slightly below 4°C . It could even be assumed, that during more or less calm conditions, a lake could totally freeze for good during a snowfall event, even

if volume-averaged water temperature was barely below 4° C. Another interesting effect on 8 October was, that the ice cover only persisted in the downwind half of the lake. From this observation it can be concluded that surface water cooled by the snow was blown towards one end of the lake, causing currents similar to those in Figure 5.14. As the snow continued to fall, the surface water was colder at the downwind part of the lake, creating the prerequisite for the ice cover to build. At the upwind part of the lake, warmer water rose from greater depths to fill the volume deficiency caused by the surface current in the direction the wind was blowing.

Ice cover thickness was only measured occasionally at Lake III. The maximum depths were regularly observed towards the end of the winter before the melting started in April or May. On 1 May 1997, the ice-slush-snow cover was about 2 m thick, most of the ice being white ice. It was formed by repeated flushing of the ice sheet after heavy snowfalls. As the total ice cover becomes thicker, it is able to support a heavier snow load. Therefore, in absence of winter melting, the water equivalent of the snow cover on the ice tends to increase over the season (Catalan, 1989).

6.2.2 Ice-models and their limitations

There are several different approaches to calculate the date of the build-up of the final ice cover. Two of these methods will be discussed here. The first approach is the formulation of a physically based model which accounts for the processes occurring within, and at the boundaries of the lake, the ice, the snow and the atmosphere (Liston and Hall, 1995; Fang et al., 1996). The second approach uses so called "threshold conditions" (Harleman, 1986). The threshold conditions are to be met before an intact ice cover is established. They include volume-averaged water temperature, daily average wind speed and daily average air temperature. All these values have to be below a certain value before a permanent ice cover can build up.

Using an exact physical model for the calculation of ice cover processes in a lake is probably the most precise way to evaluate the date of lake freeze-over apart from observing the development of the ice cover with a camera. If the time and depth resolution of the model is sufficiently small (hourly data) and the lake is sufficiently small without sheltering by trees or terrain, then the model can yield good results (Fang et al., 1996). The physical processes related to ice formation occur on a timescale of hours or minutes and in a thin region near the surface. Because of this, working with daily average values will lead to significant errors. If a lake is sheltered by terrain like most mountain lakes, then the wind speed distribution at the lake surface is quite heterogeneous. Wind mixing delays the formation of ice because it induces heat exchange between the water surface and warmer internal layers (Gu and Stefan, 1990). Therefore an ice cover will develop at the shore of the lake first, where wind speed is

generally lower, while in the middle of the lake, the mixing may be too strong for an ice cover to build up.

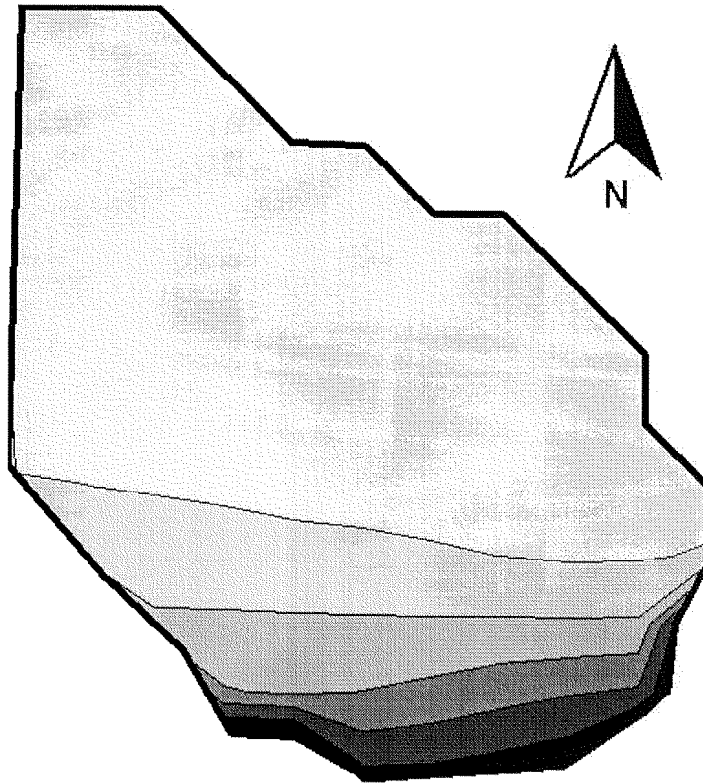


Figure 6.2: Mean daily clear sky global radiation onto Lake III from 15 October to 31 October. The darkest contour area in the south represents a radiation input between $40 \text{ W} \cdot \text{m}^{-2}$ and $60 \text{ W} \cdot \text{m}^{-2}$, while the brightest corresponds to a global radiation input of between $140 \text{ W} \cdot \text{m}^{-2}$ and $160 \text{ W} \cdot \text{m}^{-2}$. The contour spacing is $20 \text{ W} \cdot \text{m}^{-2}$. Due to the grid spacing of 25 m, the lake's shore is not smooth.

In mountain lakes wind speed is not the only heterogeneous variable being used for ice cover calculations, the same is also true for global radiation. The mean global clear sky radiation from 15 October to 31 October was calculated for all of Lake III with a grid spacing of 25 m (method see chapter 3.7.3). The results in Figure 6.2 show that the differences in incoming global radiation are large between grid points of Lake III, with some grid points receiving only 30 % of others. Ice will most likely form at the shore of the lake, where global radiation input is minimal. If a partial ice cover exists on a lake, then the energy budget and ice cover calculations become erroneous because the heat fluxes are of a different magnitude where an ice cover already exists. The sensible and latent heat flux will almost cease to exist while some of the global radiation will be reflected at the ice. The effect of a thin ice cover on the energy budget of a lake was discussed earlier (chapter 5.3.4).

A physically based model can predict the date of complete ice cover quite well, if the ice builds up uniformly on the lake on a clear cold night and if it is followed by snow fall, insulating the ice from the atmosphere. However, if a partial ice cover persists over longer periods of time, as it happens frequently in the Jöri catchment, then the models predict a wrong freeze-up date.

Threshold conditions are unknown functions which depend on the size of a lake (Fang et al., 1996) and they must be calibrated for each lake individually. They are sometimes used for the prediction of freeze-up dates in 1-dimensional lake models. The threshold conditions are generally dependent on daily mean air temperature, daily mean wind speed and volume-averaged lake temperatures. Gu and Stefan (1990) found that appropriate conditions to determine freeze-over date in a Minnesota lake were -2°C mean daily air temperature, $5\text{ m}\cdot\text{s}^{-1}$ mean daily wind speed and 2.65°C mean water temperature.

To find possible threshold conditions for Lake III, the date of freeze-over had to be determined as exactly as possible. This was done calculating the energy budget of the lake and comparing it to the measured energy budget from the thermistors. As soon as the difference between the measured and the calculated heat flux were constantly large, ice cover was assumed on Lake III. The basis for this assumption are the reduced heat fluxes for an ice-covered lake. The dates obtained for these estimates were 1 November for both 1997 and 1998. Based on knowledge of ice thickness on 9 November 1996, the freeze-up date in 1996 was around 30 October. In 1996 the volume-averaged lake temperature after freeze-up of the lake must have been above 3°C , since it was 3.07°C on 9 November 1996. In order to be able to predict ice-on correctly in 1996, the threshold condition for average water temperature have to be set to 3.1°C . This is rather high when compared to values given by Gu and Stefan (1990) and Ashton (Harleman, 1986). In 1997 volume-averaged temperature was only around 2°C and in 1998 just over 1°C when Lake III finally froze. This is clearly below threshold conditions. If the threshold model is correct, then either air temperature or wind speed were too high for a permanent ice cover to build up in 1997 and 1998. Threshold conditions that exactly meet the requirement of the different freeze-over dates of Lake III cannot be defined. The smallest errors are produced when choosing -5°C average air temperature and $3.5\text{ m}\cdot\text{s}^{-1}$ average wind speed and 3.1°C volume-averaged lake temperature. Under these conditions, the maximum offset to the actual freeze-over of the lake is 3 days, which can be considered a good prediction.

It seems that threshold conditions can be applied for to estimate the date of freeze-over in Lake III. The problem is, that the threshold conditions do not represent diurnal variability. Potential freezing during clear nights is offset by warmer day temperatures. Also, volume-averaged lake temperature has to be known, a variable

which can only be measured with thermistor chains. Alternatively one could measure lake surface temperature with the thermistor chain used for calculating volume-averaged lake temperature and from there extract the exact date at which the ice cover was formed. Too many measurements are required for this rather simple method, which makes it less applicable for remote lakes.

The easiest way to evaluate the freeze-up of a lake is to measure surface water temperature in the middle of the lake, where the lake usually freezes last or to constantly observe the lake with a camera. All the other methods are subject to errors and are based on variables which are not always measured at a lake.

6.3 Ice decay

Much emphasis has been paid to the calculation of the ice-on date of lakes (Fang et al., 1996; Liston and Hall, 1995; Harlemann, 1986); only few researchers have tried to model the ice-off date in a lake using energy budget calculations (Heron and Woo, 1994; Vavrus et al., 1996). Ice-off date are usually modeled using empirical degree-day models (Ashton, 1983; Livingstone, 1997). The reason being that the processes leading to ice-decay are more complex than the ones for freezing of a lake. The ice and snow cover on a lake surface seems homogeneous during the winter, it is completely flat. However, the composition of the ice sheet is different at every point measured. A study by Adams (Gray and Male, 1981) suggests that the sum of black ice, white ice and snow is quite homogeneous on a lake, but the fractions of each component can vary largely over a lake. The consequences of this heterogeneous distribution are not visible before the snow starts to melt on the lake surface. If the snow is not evenly distributed over the lake then it will melt earlier in some places. The snow tends to disappear from the shore first, causing a ring of exposed white ice around the still snow-covered lake (Vavrus et al., 1996). Once the snow is partially gone, some white ice will become visible. Due to the lower albedo and the lower light absorption coefficient of white ice, the surface will absorb more global radiation at the exposed places and the heterogeneity of the ice surface will increase as the melting proceeds. As white ice becomes visible, internal melting starts playing an important role as well as melting at the bottom of the ice cover, where it is in contact with the lake water (Heron and Woo, 1994). Only in the few days before the ice sheet has completely melted, the bottom melt at the water-ice interface dominates. This is the time when the lake is mostly free of ice with only a few ice floes left and the surface water starts to heat up. If the wind forcing is strong then the bottom melting is even higher due to currents, vertical mixing and ice movement (Heron and Woo, 1994).

6.3.1 Observation and interpretation of ice cover decay in the Jöri catchment

The melting of the ice on Lake III was observed with a fixed camera on a mountain ridge 200 m above the lake. The camera took one picture every day at 3 PM CET in 1997 and at 11 AM CET in 1998. Pictures are available from 2 May 1997 to 10 July 1997 and from 5 June to 14 July 1998. In 1997 the main melting process in the second half of July was missed due to malfunction of the camera. In 1998 the camera worked properly, allowing continuous visual analysis of the melting phase. The pictures taken with the fixed camera, were supplemented by observing the ice coverage at all major lakes in the catchment at weekly intervals in the years 1997 through 1999.

The melting process in Lake III was quite similar for all three years (1997 - 1999); only the timing was different. Since the ice decay is best documented for 1998, the description of the melting processes on Lake III will be done for that year. In 1998, spots of white ice were first observed on 6 June. These spots grew bigger due to higher radiation absorption (Figure 6.3). Eventually the snow melted away completely at a larger area around these initial white ice spots causing the lake ice cover to look patchy (Figure 6.4). At this time, the lake ice cover had partially disappeared, while the greatest part of the surface was still covered by white ice, some of it even by snow. That part of the lake which receives the least amount of radiation during the winter was still snow-covered on 30 June 1998.

The global radiation input to Lake III is quite homogeneous during the melting phase in May and June, due to the low zenith angle of the sun. There is possibly a delaying effect of the melting due to the heterogeneous radiation condition during ice build-up and in the winter (Figure 6.2). The thickness of the ice cover may be larger where less radiation reaches the lake during winter and where build-up of an ice cover starts earlier. Once the lake is ice-covered, the snow will add to the thickness of the ice cover, while falling snow melts on the open-water surface. In the winter the snow surface temperature will generally be lower at places which are permanently shaded by mountains, possibly decreasing sublimation from these areas leading to a higher snow water equivalent and therefore to a delayed ice melt. On 4 July 1998 less than 50 % of the lake were still ice-covered (Figure 6.5). Some large, but mostly small ice floes were moving around on the lake, increasing the melting rate due to increased turbulence at the ice-water interface. On 13 July, two days before the lake became completely ice free, only one ice floe was left (Figure 6.6). It originated from the southern shore of the lake, where radiation was small during the winter.

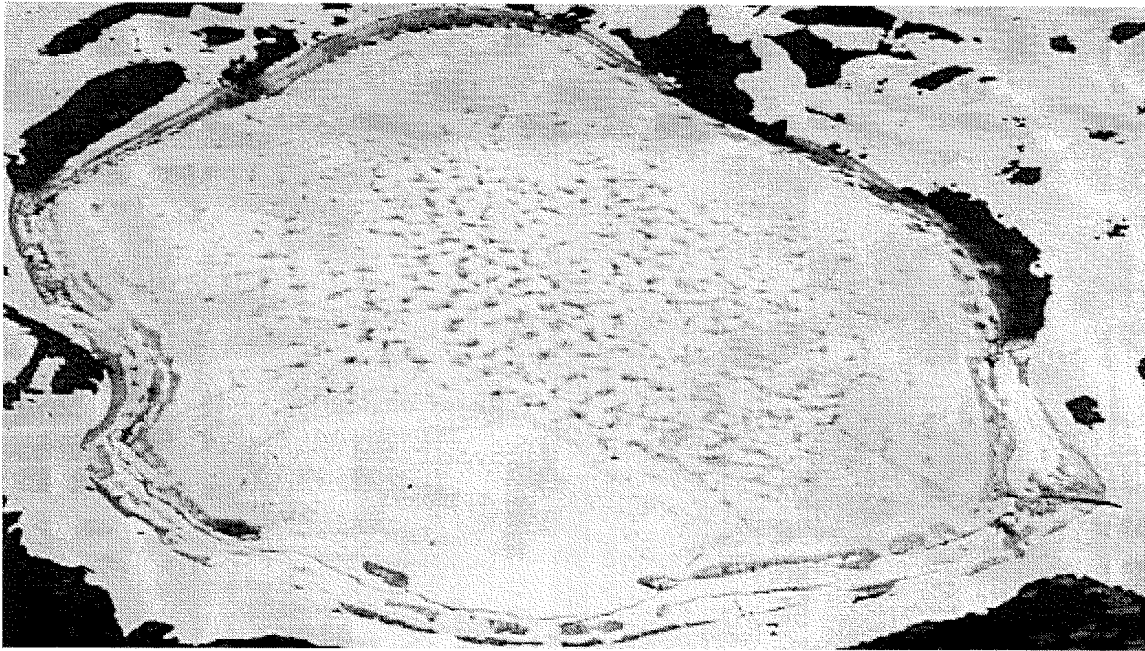


Figure 6.3: Ice cover on Lake III on 10 June 1998. The picture was taken 200 m above the lake facing northwest.

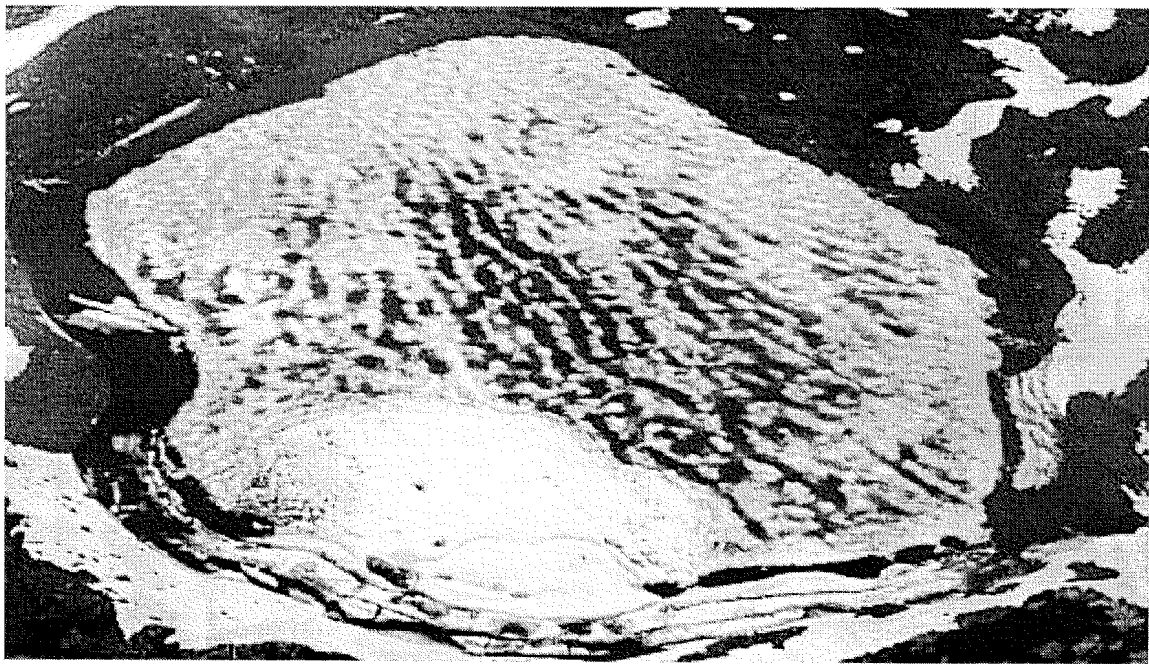


Figure 6.4: Ice cover on Lake III on 30 June 1998. The picture was taken 200 m above the lake facing northwest.

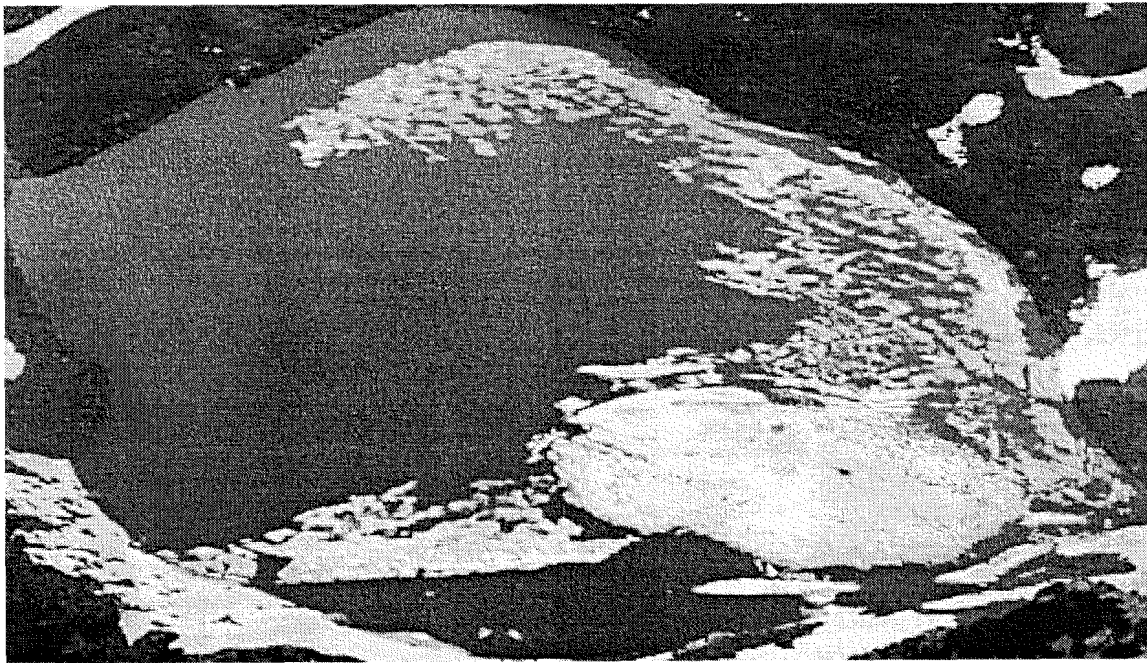


Figure 6.5: Ice cover on Lake III on 4 July 1998. The picture was taken 200 m above the lake facing northwest.

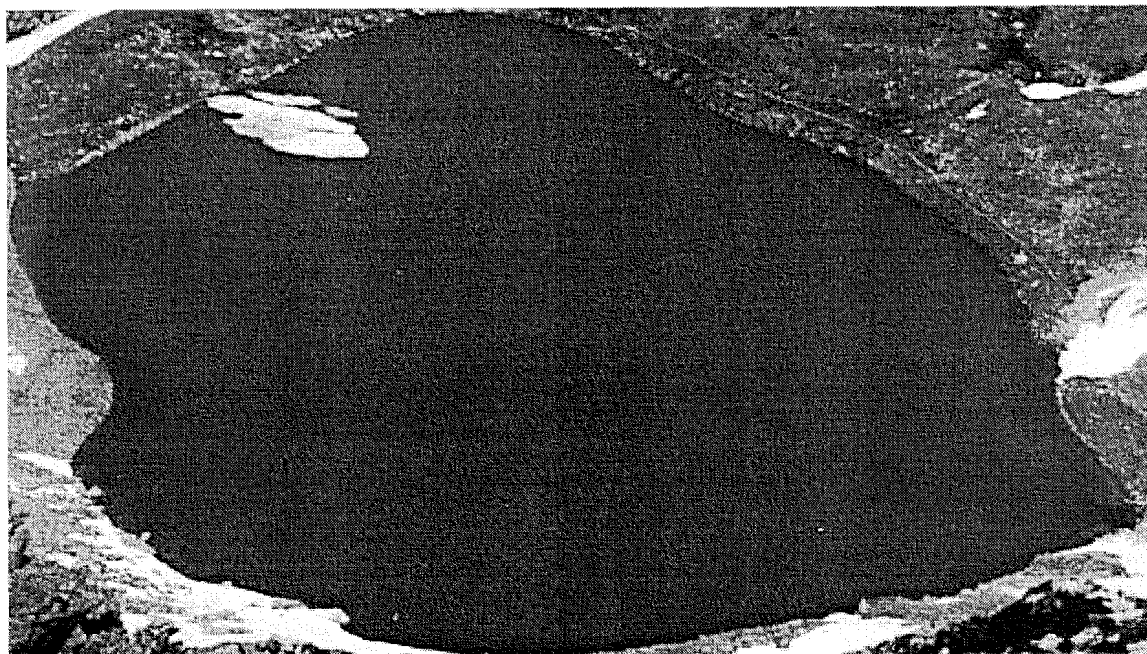


Figure 6.6: Ice cover on Lake III on 13 July 1998. The picture was taken 200 m above the lake facing northwest.

The break-up dates of all major lakes are summarized in Table 6.1. The break-up date was defined as the first day, when no more winter ice was observed on a lake. Due to only weekly observations, the dates may be off by a few days. Lacking visual observations could be partly compensated by surface water measurements, improving accuracy to ± 2 days. It is apparent that the order of ice melt is not the same every year. In fact, differences can be extreme. Lake I melted 27 days before Lake X in 1997, but in

1998 the situation was reversed, with Lake X breaking up 7 days before Lake I. The year 1999 was similar to 1997. Avalanches on Lake X caused it to remain partly ice covered for a long time in 1997 and 1999. Lake X would have been ice free on 23 July 1997 without the avalanche ice in 1997. In 1999 the ice never melted in Lake X due to a particularly large avalanche filling about one third of the lake. In the Jöri catchment, only the ice cover on Lakes III and X can be influenced by the large displaced snow masses. In 1997 the delay of ice break-up in Lake III due to the additional snow was in the range of 10 days, while in 1999 it was about 15 days. No avalanches were observed on any lake in 1998.

| year | Lake I | Lake III | Lake VII | Lake X | Lake XII | Lake XIII |
|------|--------|----------|----------|-----------|----------|--------------|
| 1997 | 25 Jul | 2 Aug | 4 Aug | 21 Aug | n.a. | 16 Aug |
| 1998 | 11 Jul | 15 Jul | 15 Jul | 3 Jul | 7 Jul | 17 Jul |
| 1999 | 1 Aug | 16 Aug | 20 Aug | avalanche | 1 Aug | after 15 Sep |

Table 6.1: Approximate break-up dates of the six largest lakes in the Jöri catchment from 1997 to 1999, based on observations and partly on LSWT measurements. (n.a. = date not available)

The differences in ice break-up which are not associated with avalanches are quite complex. The most important factors are radiation, air temperature, maximum spring snow load and size of the lake. The first two factors are evident, more radiation and higher air temperature accelerate snow and ice melting. The higher the snow load, the more of the snow is incorporated into the ice sheet, therefore thickening it and delaying complete melting. The size of the lake is of importance because the ice first melts at the shore. A smaller lake has a larger relative shoreline fraction than a large lake. Therefore the smaller lake will "see" a warmer climate because a higher fraction of the lake becomes ice free first (Vavrus et al., 1996).

6.3.2 Calculation of the break-up date

The simplest approach to modeling the decay of lake ice is the degree-day method (Ashton, 1983), which assumes that air temperature is a good indicator of the available energy and melt processes. The energy balance approach requires more data, but it deals with the energy exchanges in a more realistic manner and forms the basis of the more comprehensive lake-ice growth and decay models (Heron and Woo, 1994). All the models have to deal with the heterogeneous processes associated with ice melt. It is questionable whether the complex "energy balance models" produce better results than the empirical, easy to use "degree-day models". This is especially true for mountain lakes, where conditions are expected to be more heterogeneous than in a lowland lakes

surrounded by flat terrain. This is the reason why no energy balance model of ice melt was applied to the Jöri Lake III.

An empirical model was created for Lake III based on data measured at the SMI-AWS of Weissfluhjoch. Only 3 years of ice decay observations were available for calibration. Data from Weissfluhjoch AWS were used, because it allowed hindcasting of the ice-off dates back to 1959 and because the used variables air temperature and new snow height are similar at Jöri Lake III (see chapter 3.9.2). In order to avoid large errors, the delay of ice melting due to avalanches was removed. The lake was considered ice free at the time when only avalanche ice masses were still on the lake. The dates for these theoretical break-up dates were 27 July 1997, 15 July 1998 and 2 August 1999 based on observations for Lake III (Figure 6.1).

At first, a simple degree-day model was applied assuming equal ice thickness for all years, adding values of days with positive air temperatures starting 1 May (Livingstone, 1997). The calibration of such a model is impossible for Lake III. The difference between calculated and the observed ice-off dates would have a standard deviation of about 15 days for the years 1996 to 1999. This approach does not work because it assumes equal ice thickness for all years. In previous degree-day models lakes in lowlands, in the arctic or at lower elevation mountain sites were thought to have equal ice-thickness in all years. At the Jöri lakes and possibly at other high mountain lakes this assumption is wrong.

From the description of the evolution of the ice cover earlier in this chapter, it seems that snow plays an important role. Vavrus et al. (1996) found that an increased snowfall rate prolongs the ice cover period substantially in their model. It was assumed that the ice cover on Lake III is essentially defined by the total amount of snow falling during the winter and during the melting period. At first the freeze-up date of the lake was roughly estimated for each year. Depending on prevailing temperature conditions it was set to be anywhere between 20 October and 10 November. Earlier or later freeze-up dates were disregarded and set to the boundary of the mentioned time period. From the estimated ice freeze-up date, the new snow at Weissfluhjoch AWS was added up continuously until the ice cover had disappeared. A degree-day model was applied, subtracting the mean daily air temperature value multiplied with a degree-day factor d from the accumulated new snow height starting 1 May. Days with mean air temperatures below 0°C were disregarded. The constant d was set to be $0.25\text{ cm}\cdot\text{K}^{-1}\cdot\text{d}^{-1}$ after the calibration by trial and error. This value is lower than most of the degree-day factors used for snow melt calculations (Martinec and Rango, 1986). The reason for this is that not only the snow that fell on the ice cover had to be melted. Lake water which flooded the snow also partially froze in the cold winter climate. Therefore the water

equivalent of the ice layer is actually larger than the accumulated snow on the surface, leading to the lower degree-day factor.

The timing of the theoretical ice melt without the influence of avalanches was modeled well for the years 1997 to 1999 with the assumptions above. The standard deviation of the calculated ice melt from the observed theoretical ice melt was only 2 days. The modeled break-up date on 20 June 1996 could also be correct, since the break-up was certainly before July (pers. obs.).

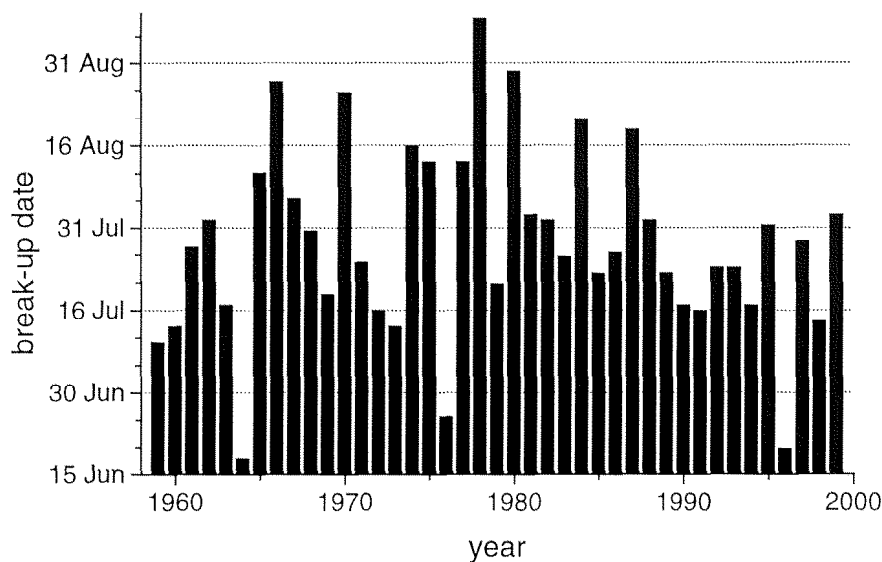


Figure 6.7: Calculated break-up dates for Lake III from 1959 to 1999 based on data from Weissfluhjoch AWS.

The same empirical model was applied to all years from 1959 to 1999 to get some idea of the variability of break-up for Lake III (Figure 6.7). The latest calculated break-up date was 9 September 1978, the earliest calculated break-up date was 18 June 1964. Average calculated break-up date in these 41 years was 28 July with a standard deviation of 18 days. In order to figure out, whether the lake could have remained ice-covered throughout a whole summer, the greatest snow-height on 1 May (year 1970) was combined with the coldest summer (year 1984). In such a year, the ice would never have completely thawed, according to the model. In higher lying Lake XIII this was almost the case in 1999, where ice completely disappeared only after the middle of September. A late break-up date in lake leads to a low heat input, inducing an early freeze-up date. This, in turn, would also favor a late break-up date in the next year, due to higher snow accumulation on the lake. The earliest possible break-up date would have been on 11 June with data from the warmest May and June (year 1964) and the least snow height on 1 May (year 1972).

Figure 6.7 shows that there were no late lake break-ups after 1987. While there were 11 break-up dates after 3 August between 1959 and 1987, there were none after 1987. This may be an indicator for increased May, June and July air temperature or for less snow during the winter. Assuming a homogeneous distribution of the years with break-up dates after 3 August between 1959 and 1987, the probability of 12 consecutive years with break-up dates before 4 August is only 0.2 %. No significant trends were found for accumulated new snow heights (Figure 6.8). For the average air temperature between 1 May and 20 June (Figure 6.9), which is during the melting phase for all years, a significant trend was found. The percentage of years with an average air temperature above 0.8°C was significantly higher ($p < 0.03$) from 1988 to 1999 than before 1988. In fact, of the 12 years between 1988 and 1999, 8 had an average air temperature above 0.8°C for the stated period, while in the previous 29 years, only 6 had an average air temperature above 0.8°C . Despite the significant warming after 1987 in the months of May and June as well as the lack of late break-up dates, there is only a weak significant correlation ($p < 0.05$, $r^2 = 0.21$) between the air temperature from 1 May to 20 June and the calculated break-up date of Lake III. The correlation is better between accumulated height of new snow and the calculated break-up date ($p < 0.05$, $r^2 = 0.55$).

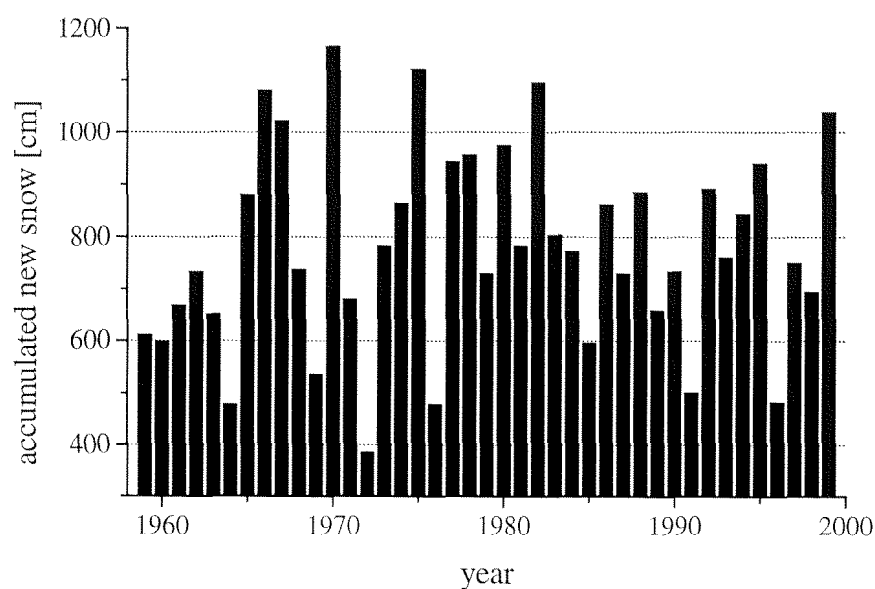


Figure 6.8: Sum of measured new snow at Weissfluhjoch from the time of ice formation on Lake III to 1 May of the following year, for the years 1959 to 1999.

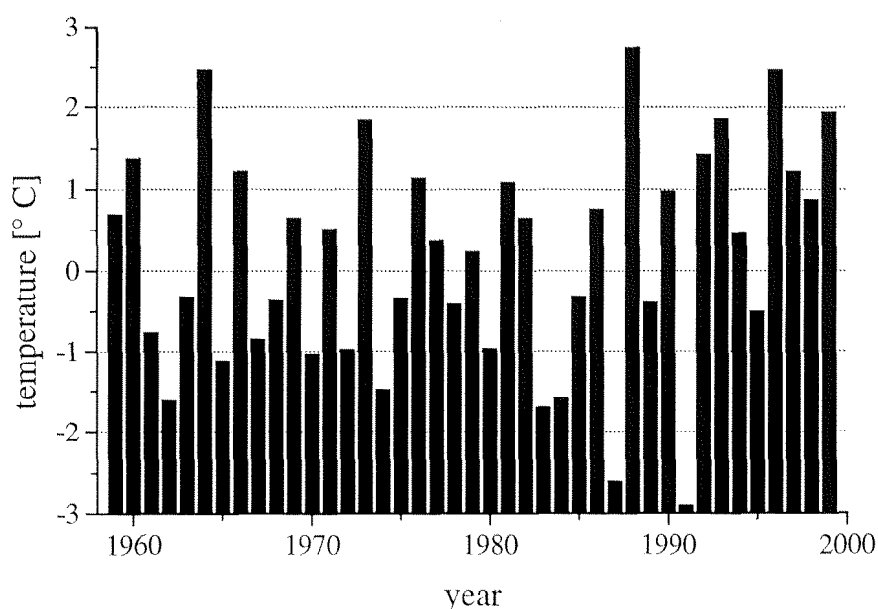


Figure 6.9: Average air temperature measured at Weissfluhjoch AWS in the melting period from 1 May to 20 June, 1959 to 1999.

6.4 Conclusions

The calculations of the freeze-up date in a mountain lake are dependent on meteorological measurements made at the lake and also on water temperature profiles. Therefore it is not possible to calculate the freeze-up date of remote lakes where no measurements are carried out. Even if data from a mountain lake were available, the ice build-up is too heterogeneous in space for exact calculations. The largest problems stem from the heterogeneous wind and radiation distribution on a mountain lake. The application of energy budget models or "threshold conditions" for the determination of the freeze-up date in mountain lakes can yield large errors. In mountain lakes, a precise determination of the ice build-up date can only be achieved with daily visual observations or by measuring continuous surface water temperature in the middle of the lake.

In previous ice-decay models, the maximum winter ice thickness was assumed to be equal every year. At the Jöri lakes and probably also at other high mountain lakes, this is not true, due to large snow heights and a long ice cover period. The time of ice-out in high mountain lakes is most dependent on the amount of snowfall during the ice cover period and on air temperature during the melting phase. The calculated break-up dates are only valid for Lake III and they did not account for avalanches on the lake. Excluding the large effects of the avalanches for the break-up calculations, the model yielded very good results, predicting the ice-out of Lake III to within 2 days from 1997

to 1999. The calculated break-up dates are also an indicator for the break-up of other lakes in a small region. There is a significant trend for earlier break up dates since 1988 compared to the years from 1959 to 1987 if the calculations are correct. This trend is due to the rising air temperature in the months May and June at Weissfluhjoch AWS. No significant trend was found for maximum snow height for the past 40 years.

7 Conclusions and outlook

7.1 Conclusions

High resolution meteorological measurements within and around the Jöri catchment showed that some meteorological variables in a catchment can be approximated well with data from stations nearby (air temperature, humidity, global radiation), while for other variables this task is dependent on the location of the sites of the nearby stations (wind, precipitation). Wind speed is an important component in energy flux calculation of lakes. In order to accurately calculate the energy budget of a lake, wind measurements at the shore of or on a lake are crucial. It was also found that precipitation plays an important role for the heat fluxes between the atmosphere and mountain lakes, as opposed to lowland lakes. The components needed to calculate the energy budget of lakes under all conditions are presented in Figure 7.1.

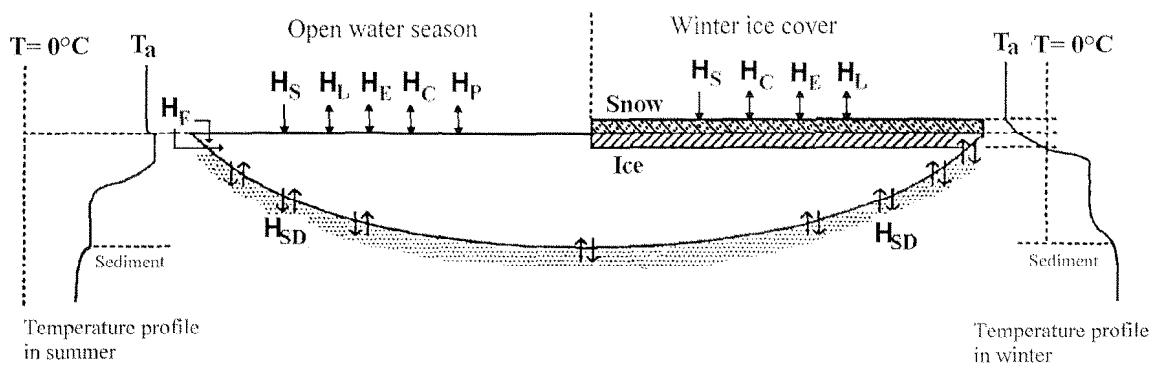


Figure 7.1: Scheme of the meteorological forcing and its effects on a lake during the open-water season and during winter. Explanations of the abbreviations of the heat fluxes can be found in chapter 5.2.

Even if all meteorological variables are measured at a mountain lake, errors between calculated and measured energy budgets occur. The reason for this are those factors influencing the energy budget of a lake, which cannot be parameterized with meteorological data. These include water throughflow, sediment heat exchange and albedo of a lake. Sediment heat exchange only plays an important role in shallow lakes and after rapid temperature changes. Throughflow heat flux is more important, but difficult to measure due to the frequent subsurface inflows in mountain lakes. Because of these difficulties, the accuracy of energy budget calculations in mountain lakes largely varies from lake to lake, with errors being largest for lakes with cold glacier water input. The heterogeneity of lake water temperatures in the Jöri catchment stems from different factors. The most important of these are catchment characteristics, lake

depth, turbidity and wind. These factors can be quantified and thus the heterogeneity of water temperatures of different lakes within a small area can be explained and estimated.

Albedo in lakes with turbid glacier meltwater input is generally higher than in clear lakes. Albedo has to be measured in lakes with high concentrations of suspended erosion particles since its effect on the energy budget is significant. The optical properties of turbid glacial lakes are different from clear lakes, mostly due to the high radiation attenuation of suspended erosion particles. While in most clear mountain lakes enough radiation is available to allow photosynthesis even at its very bottom, in turbid lakes the euphotic zone may be as thin as 4 m. The turbidity in lakes with glacier meltwater input is highly variable, both in time and space (Figure 7.2). Generally, turbidity is higher in the hypolimnion due to the high density of the inflowing glacier meltwater. Turbidity reaches its highest values after fall overturn, when suspended erosion particles are dispersed throughout the lake. As an essential physical ecosystem determinant the changing turbidity has to be monitored throughout the open-water season in turbid glacial lakes.

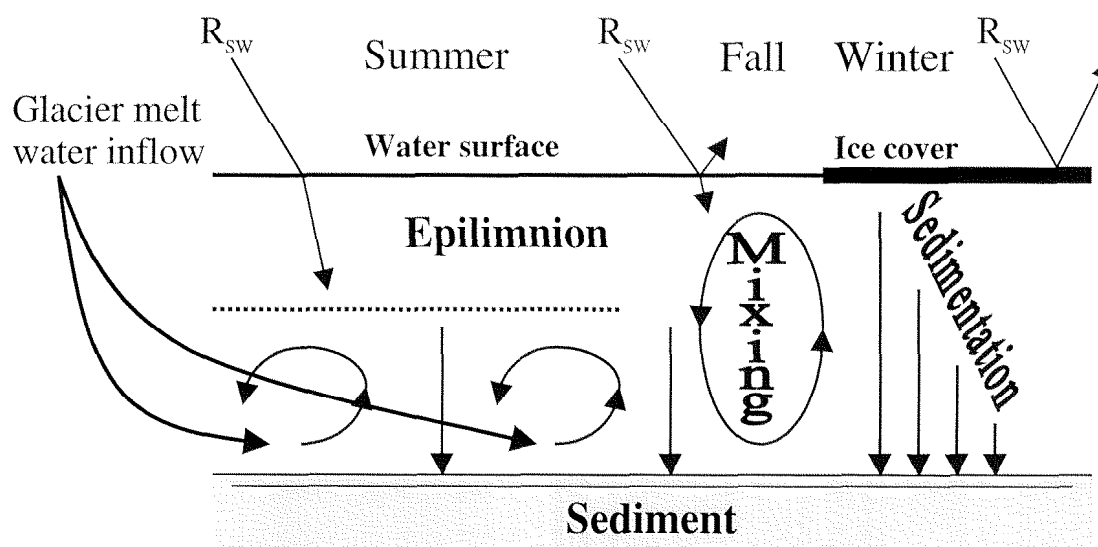


Figure 7.2: Scheme of the distribution of suspended erosion particles for the seasons summer, fall and winter. Particles enter the hypolimnion by subsurface inflows during the open-water period. Within the hypolimnion there is constant mixing and sedimentation of the particles. During fall overturn the particles are dispersed throughout the lake increasing the global radiation (R_{SW}) albedo and the attenuation in the epilimnion. After freeze-over the suspended erosion particles settle slowly to the lake bottom. All global radiation (R_{SW}) is reflected at the ice-cover.

The duration of the ice cover on a mountain lake is an important factor determining the development of organisms. The freeze-over of a lake is difficult to model or estimate from meteorological data. The heterogeneity of the meteorological

variables over the whole lake area and the often lacking high frequency measurements make an exact determination of freeze-over impossible. The most precise method is to measure lake surface water temperature in the middle of the lake, or observing the lake daily. The ice cover duration at high mountain lakes largely depends on the maximum snow height. Previous models assumed equal ice thickness every year, therefore they are not applicable to high mountain lakes. In order to get a good estimate of the timing of ice melt, information on snow height near the lake in question has to be obtained. The degree-day model developed yielded encouraging results for the break-up dates of Lake III. Air temperature data from Weissfluhjoch indicate a warming trend in the months of May and June in the past 11 years, causing the lakes to thaw earlier according to the ice-decay model.

Research in the Jöri catchment has been intensive and the physical ecosystem determinants of Lake III and of some other lakes in the catchment have been described and modeled. The physical processes taking place in mountain catchments and lakes are now known very well. Based on the present study, the physical ecosystem determinants can be estimated in mountain lakes without intensive measurement campaigns.

7.2 Outlook

The research in the Jöri catchment will be intensified in Lake XIII, a lake where ice cover duration is extended compared with Lake III. In fact, under certain circumstances, the lake can remain ice-covered for more than one year. The unknown physical, chemical and biological processes underneath the ice during the melting period will be examined most intensively. Other relevant physical research questions for mountain lakes would be: Are common wind functions for the calculation of sensible and latent heat flux usable in mountainous terrain or do they have to be adapted to each lake? What are the dynamics of water below 4° C entering a well stratified lake? Can a cold inflow induce internal seiches? How important are the influences of heterogeneous longwave radiation on lakes?

Seite Leer /
Blank leaf

Appendix

Technical specifications of instruments

Humidity:

Measuring height: 6 m
 Type: Rotronic Hygrometer C-80
 Accuracy: $\pm 1\%$
 Time constant: < 10 sec
 Not artificially aspirated

Temperature:

Measuring height: 6 m
 Type: Pt-100 Ohm
 Accuracy: $\pm 0.2^\circ$
 Time constant: 10 sec
 Not artificially aspirated

SW Radiation:

Measuring height: 3 m
 Type: Kipp and Zonen CM 6B
 Spectral range: 305 - 2800 nm
 Time constant: 5 sec to $1/e$
 Accuracy: $\pm 1.5\%$
 Not ventilated, not heated

LW Radiation:

Measuring height: 3 m
 Type: Kipp and Zonen CG1
 Spectral range: 5 - 50 μm
 Field of view: 150°
 Accuracy: $\pm 5\%$
 Not ventilated, 1 Watt heating

Wind Speed:

Measuring height: 7 m
 Type: Vaisala WAA 15
 Threshold: $0.4 \text{ m}\cdot\text{s}^{-1}$
 Accuracy: $\pm 0.1 \text{ m/s}$, 2% above 10 m/s
 Not heated

Wind Direction:

Measuring height: 7 m
 Type: Vaisala WAV 15
 Threshold: $0.3 \text{ m}\cdot\text{s}^{-1}$
 Resolution: 5.63°
 Accuracy: 2.8°
 Not heated

Precipitation:

Type: tipping gauge (Gertsch)
 Measuring height: 1.7 m
 Not heated

PAR above water:

Measuring height: 0.5 m above lake
 Type: LI-COR 190SA
 Cosine corrected
 Time constant: $10 \mu\text{sec}$
 Accuracy: $\pm 5\%$

PAR below water:

Measuring depth: 0.1 m and 1 m

Type: LI-COR 193SA

Spherical sensor

Time constant: 10 μ sec

Accuracy: \pm 5 %

Lake surface water temperature:

Measuring depth: 12 cm

Type: Vemco Minilog-TR

Accuracy: \pm 0.3 °C

Time constant: 30 sec

Lake III temperature profile:

Measuring depths [*m*]: 1.1, 1.3, 2.1, 2.3,
2.8, 2.9, 3.7, 4, 4.7, 4.9, 5.3, 5.8, 6, 6.5, 6.7
6.9, 7.7, 8.6, 9.2, 11, 14.2, 16

Type: Anderaa Temperature Profiler TR7v

Time constant: 60 sec

Accuracy: \pm 0.05° C

Data from other institutes

Stillberg climatic data were provided by the group of bioclimatology, Swiss Federal Institute for Forest, Snow and Landscape Research (WSL), CH-8903 Birmensdorf.

Gatschiefer, St. Jaggem and Piz Müra climatic data were provided by the IMIS-group at the Swiss Federal Institute for Snow and Avalanche Research (SLF), CH-7260 Davos.

Weissfluhjoch and Payerne climatic data were extracted from the Swiss Climate Database of the Swiss Meteorological Institute (SMI), CH-8044 Zürich.

Weissfluhjoch, Research Field SLF and Payerne radiation data were provided by the World Radiation Center (WRC), CH - 7260 Davos.

The data used for calculations and comparisons in this study (see chapter 3) can be obtained from the respective institutes. For copyright reasons they cannot be distributed by the author.

Meteorological data from the Jöri AWS

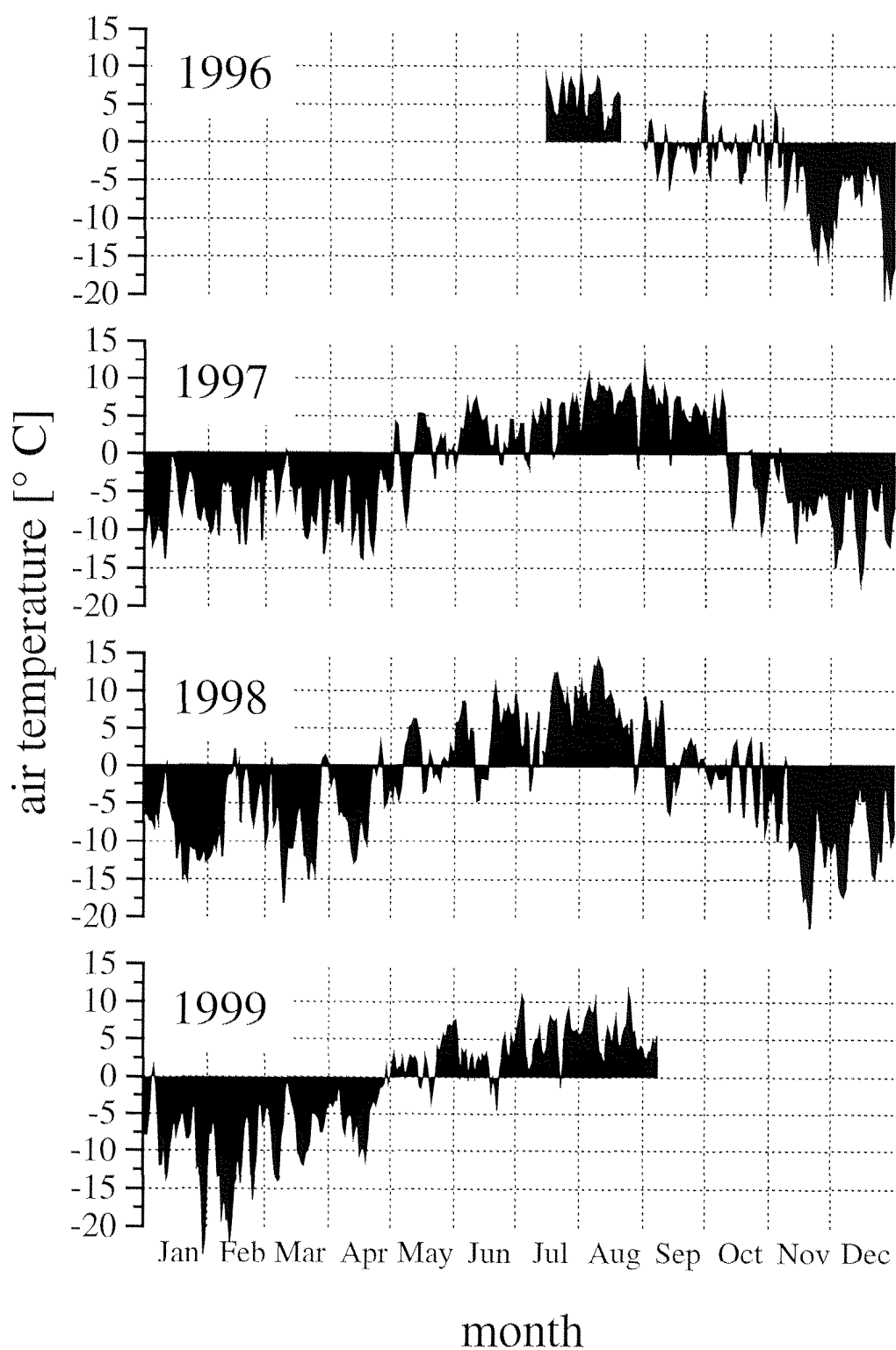


Figure A-1: Daily mean air temperature at the Jöri AWS from 15 July 1996 to 8 September 1999.

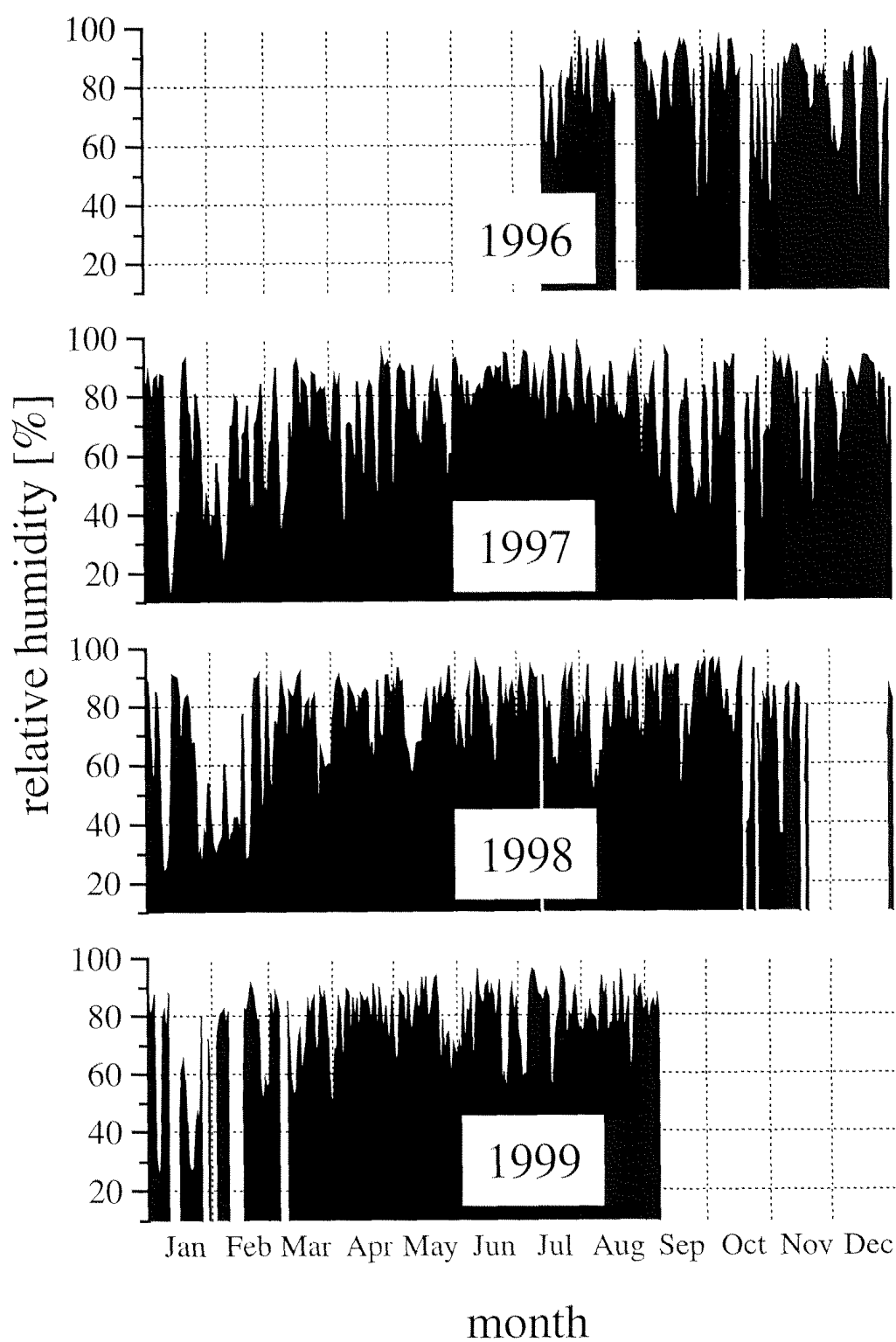


Figure A-2: Daily mean relative humidity at the Jöri AWS from 15 July 1996 to 8 September 1999.

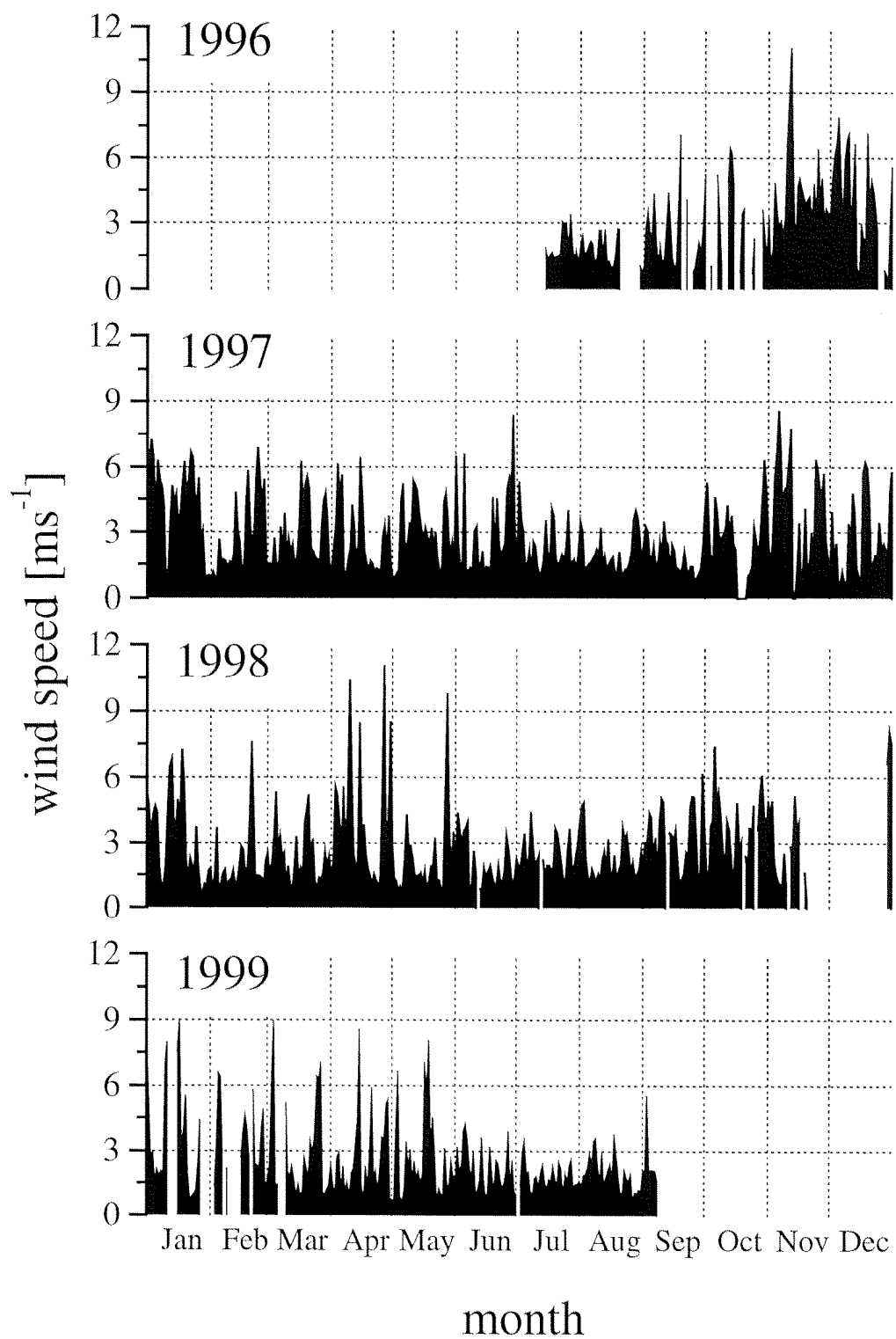


Figure A-3: Daily mean wind speed at the Jöri AWS from 15 July 1996 to 8 September 1999.

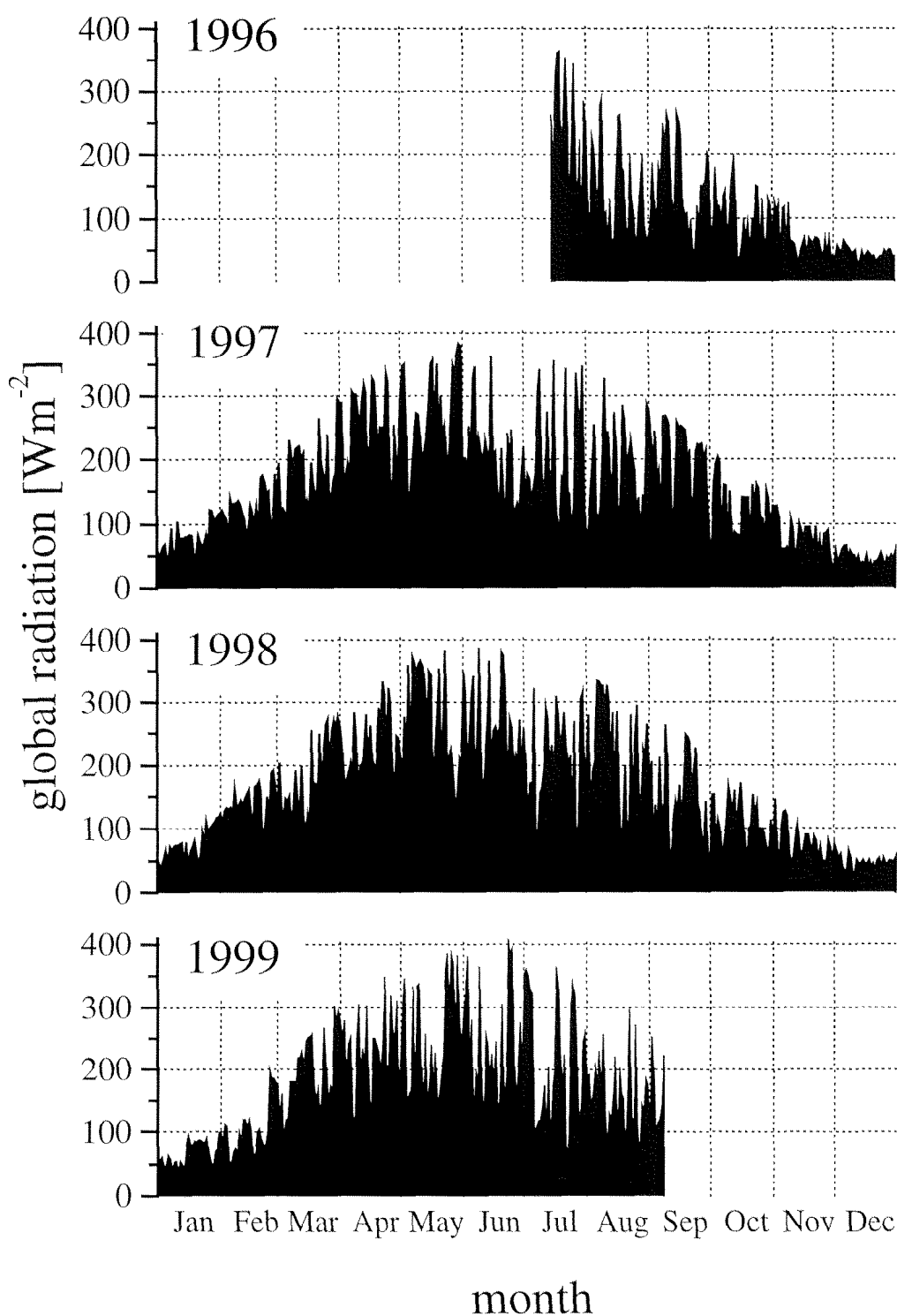


Figure A-4: Daily mean global radiation at the Jöri AWS from 15 July 1996 to 8 September 1999.

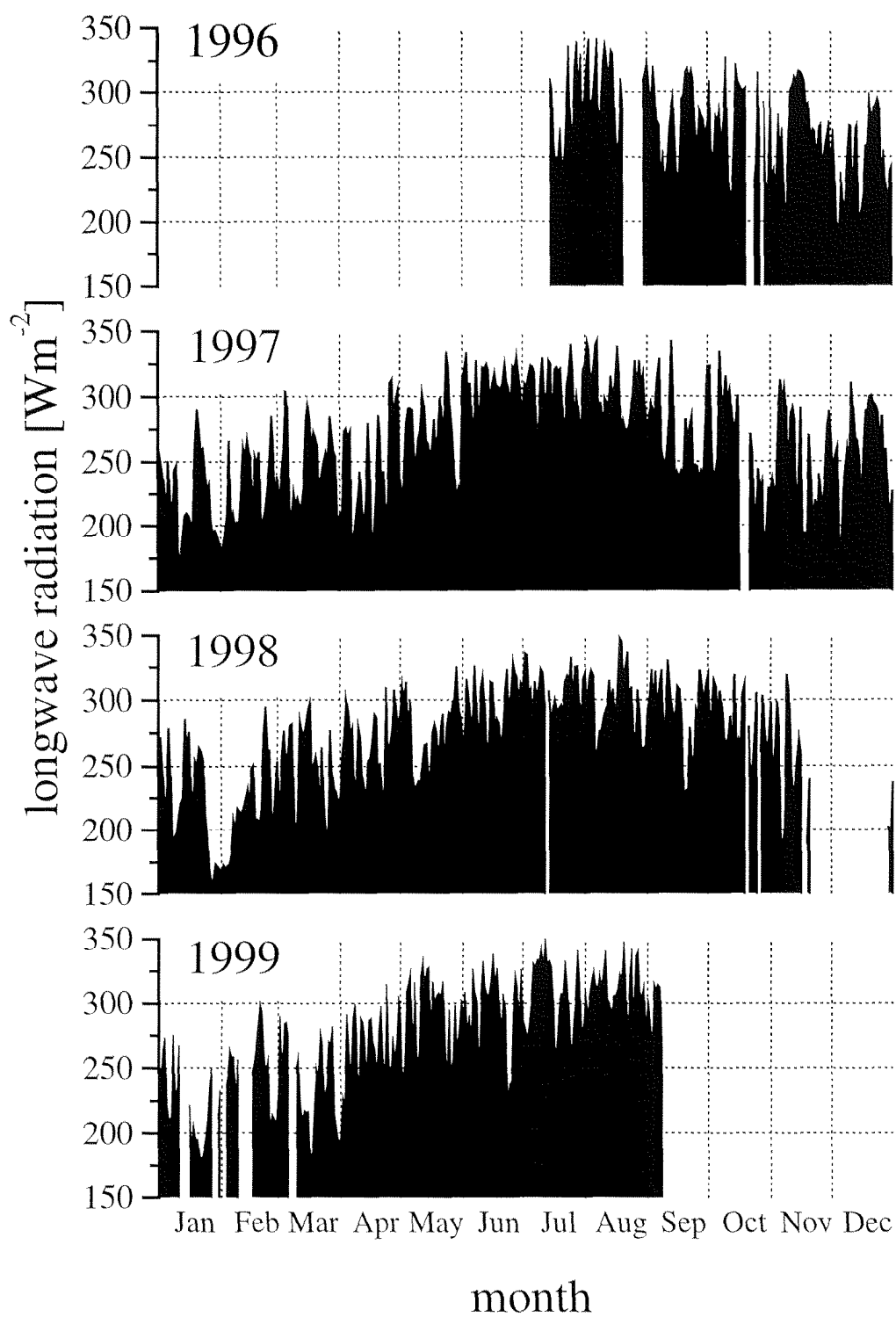


Figure A-5: Daily mean longwave radiation at the Jöri AWS from 15 July 1996 to 8 September 1999.

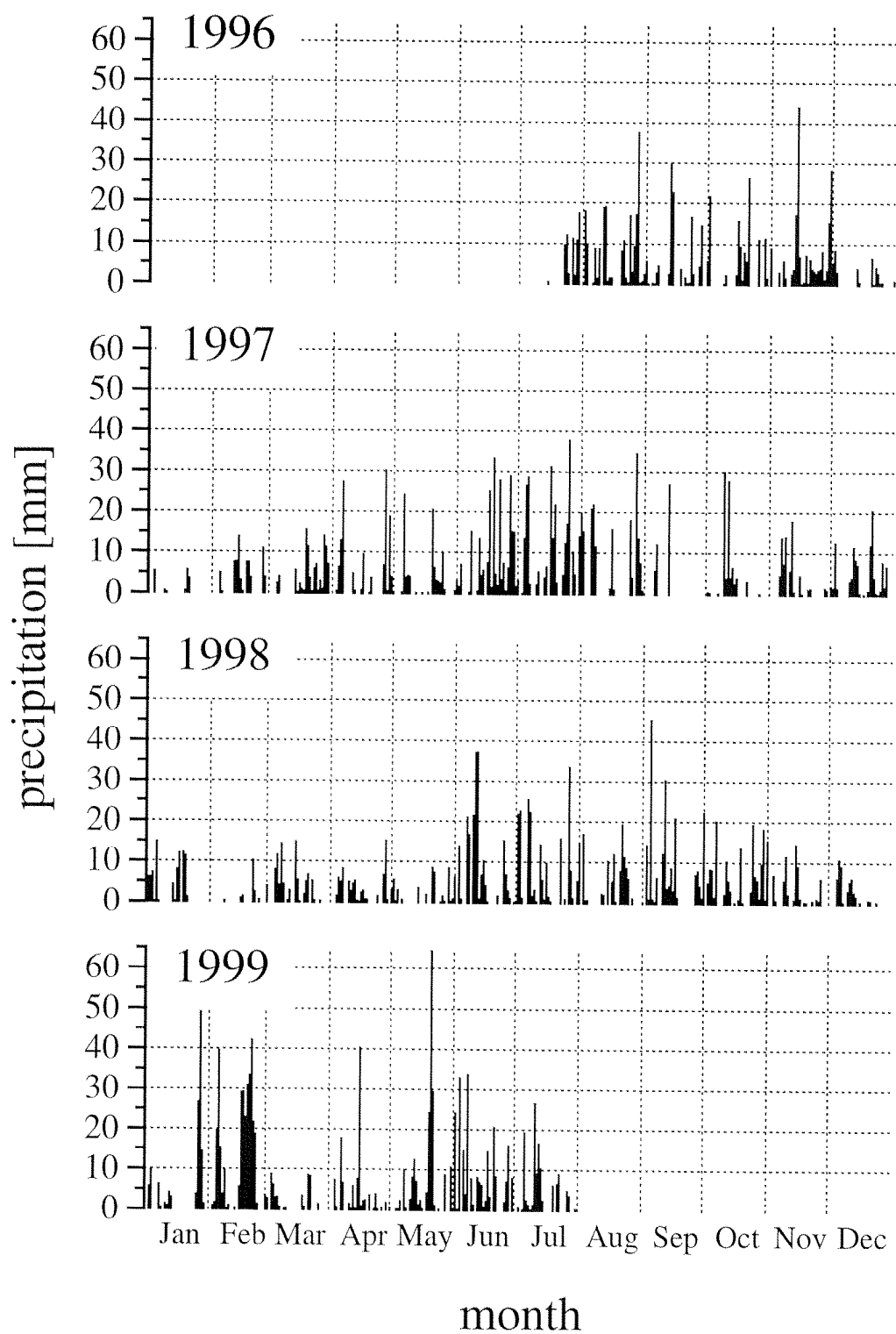


Figure A-6: Daily sum of precipitation at the Weissfluhjoch AWS from 15 July 1996 to 31 July 1999.

Abbreviations

| | |
|--------|-----------------------------------------------------------------|
| AWS: | Automatic weather station |
| CET: | Central European time |
| DEM: | Digital elevation model |
| ETH: | Swiss Federal Institute of Technology, Zürich |
| GPS: | Global positioning system |
| LSWT: | Lake surface water temperature |
| MBE: | Mean bias error |
| MOLAR: | Mountain lake research |
| NTU: | Nephelometric turbidity units |
| PAR: | Photosynthetically active radiation |
| RMSE: | Root mean square error |
| SLF: | Swiss Federal Institute for Snow and Avalanche Research |
| SMI: | Swiss Meteorological Institute |
| UNIZH: | University of Zürich |
| V/C: | Volume to catchment ratio |
| WRC: | World Radiation Center |
| WSL: | Swiss Federal Institute for Forest, Snow and Landscape Research |

Seite Leer /
Blank leaf

Bibliography

- Adams, E. E., D. J. Cosler, and K. R. Helfrich, 1990. Evaporation from heated water bodies - predicting combined forced plus free-convection. *Water Resources Research*, 26(3), 425-435.
- Ammann, W. (ed), 1997. Schnee und Lawinen in den Schweizer Alpen Winter 1995/96. Winterbericht des Eidg. Institutes für Schnee- und Lawinenforschung Weissfluhjoch/Davos, No. 60.
- Ashton, G. D., 1983. Lake ice decay. *Cold Regions Science and Technology*, 8(1), 83-86.
- Aubinet, M., 1994. Longwave sky radiation parameterisations. *Solar Energy*, 53(2), 147-154.
- Bengtsson, L., and T. Svensson, 1996. Thermal regime of ice-covered Swedish lakes. *Nordic Hydrology*, 27(1-2), 39-56.
- Bilello, M. A., 1968. Water temperatures in a shallow lake during ice formation, growth, and decay. *Water Resources Research*, 4(4), 749-760.
- Bonderer, J., 1997. Temperaturmodellierung im Luganersee-Nordbecken. Diploma thesis, ETH Zürich.
- Brady, D. K., W. L. Graves, and J. C. Geyer, 1969. Surface heat exchange at power plant cooling lakes. *Cooling Water Studies for Edison Electric Institute*, Report No. 5.
- Brown, D. G., and S. J. Walsh, 1992. Relationships between the morphometry of alpine and subalpine basins and the remotely sensed estimates of lake turbidity, Glacier National Park, Montana. *Physical Geography*, 13(3), 250-272.
- Brutsaert, W., 1975. On a derivable formula for longwave radiation from clear skies. *Water Resources Research*, 11, 742-744.
- Catalan, J., 1989. The winter cover of a high-mountain Mediterranean lake (Estany Redo, Pyrenees). *Water Resources Research*, 25(3), 519-527.
- Collins, D. N., 1988. Suspended sediment and solute delivery to meltwaters beneath an alpine glacier. *Mitteilungen der Versuchsanstalt für Wasserbau, Hydrologie und Glaziologie*, Nr. 94.
- Conway, H., A. Gades, and C. F. Raymond, 1996. Albedo of dirty snow during conditions of melt. *Water Resources Research*, 32(6), 1713-1718.
- Cuker, B. E. 1993. Suspended clays alter trophic interactions in the plankton. *Ecology*, 74(3): 944-953.

- Dozier, J., and J. E. Frew, 1990. Rapid calculation of terrain parameters for radiation modelling from digital elevation data. *IEEE Transactions of Geosciences and Remote Sensing*, 28(5), 963-969.
- Edinger, J. E., D. W. Duttweiler, and J. C. Geyer, 1968. The response of water temperatures to meteorological conditions. *Water Resources Research*, 4, 1137-1143.
- Effler, S. W., 1985. Attenuation versus transparency. *Journal of Environmental Engineering*, 111(4), 448-459.
- Fang, X., C. R. Ellis, and H. G. Stefan, 1996. Simulation and observation of ice formation (freeze over) in a lake. *Cold Regions Science and Technology*, 24(2), 129-145.
- Fang, X., and H. G. Stefan, 1996. Dynamics of heat exchange between sediment and water in a lake. *Water Resources Research*, 32(6), 1719-1727.
- Froehlich, C., R. Philipona, and Ch. Marty, 1998. Untersuchung des Oberflächenstrahlungshaushaltes in den Alpen im Vergleich zum schweizerischen Mittelland. Schlussbericht NFP31, VDF ETH Zürich.
- Fukushima, T., M. Aizaki, and S. Ebise. 1991. Dynamics of particulate matter near the mouth of influx river in Takahamairi Bay of Lake Kasumigaura, with special reference to nitrogen and phosphorus. *Japanese Journal of Limnology*, 52(1): 13-26.
- Gensler, G. A., 1978. Das Klima von Graubünden : ein Beitrag zur Regional-klimatologie der Schweiz. Universität Zürich.
- Gray, D. M., and D. H. Male, 1981. Handbook of snow : principles, processes, management & use. Pergamon Press, Toronto.
- Greuell, W., W.H. Knap, and P.C. Smeets, 1997. Elevational changes in meteorological variables along a midlatitude glacier during summer. *Journal of Geophysical Research*, 102, 25941-25954.
- Gu, R., and H. G. Stefan, 1990. Year-round temperature simulation of cold climate lakes. *Cold Regions Science and Technology*, 18, 147-160.
- Harbeck, G. E., 1962. A practical field technique for measuring reservoir evaporation utilizing mass-transfer theory. In: U.S. Geological Survey Professional Paper 272E. U.S. Government Printing Office. Washington, D.C.
- Harleman, D. R. F., 1986. Hydrothermal modelling of reservoirs in cold regions: Status and research needs. In: *Proceedings of Cold Regions Hydrology Symposium*, 39-49.

- Henderson-Sellers, B., 1986. Calculating the surface energy balance for lake and reservoir modelling: A review. *Reviews of Geophysics*, 24(3), 625-649.
- Heron, R., and M.- K. Woo, 1994. Decay of a high arctic lake-ice cover: observations and modeling. *Journal of Glaciology*, 40, 283-292.
- Hinder, B., M. Gabathuler, B. Steiner, K. Hanselmann, and H. R. Preisig, 1999. Seasonal dynamics and phytoplankton diversity in high mountain lakes (Jöri lakes, Swiss Alps). *Journal of Limnology*, in press.
- Hondzo, M., and H. G. Stefan, 1993. Lake water temperature simulation model. *Journal of Hydraulic Engineering*, 119(11), 1251-1273.
- Idso, S. B., and R. D. Jackson, 1969. Thermal radiation from the atmosphere. *Journal of Geophysical Research*, 74, 5397-5403.
- Jerlov, N. G., 1968. *Optical oceanography*. Elsevier oceanography series, vol. 5, Amsterdam.
- Keijman, J. Q., and R. W. R. Koopmans, 1973. A comparison of several methods of estimating the evaporation of Lake Flevo. In: *Proceedings of the Helsinki Symposium on the Hydrology of Lakes*. IAHS Publication No. 109, 225-232.
- Koenings, J. P., and J. A. Edmundson, 1991. Secchi disk and photometer estimates of light regimes in Alaskan lakes: Effects of yellow color and turbidity. *Limnology and Oceanography*, 36(1), 91-105.
- Kondratyev, K. Y., 1973. *Radiation characteristics of the atmosphere and the earth's surface*. Amerind Publishing Co., New Delhi.
- Koracin, D., and L. Enger, 1994. A numerical study of boundary-layer dynamics in a mountain valley. *Boundary-Layer Meteorology*, 69(3), 249-283.
- Konzelmann, T., R. S. W. Vandewal, W. Greuell, R. Bintanja, E. A. C. Henneken, and A. Abeouchi, 1994. Parameterization of global and longwave incoming radiation for the Greenland ice-sheet. *Global and Planetary Change*, 9(1-2), 143-164.
- Kreis, H. A., 1920. Die Jöriseen und ihre postglaziale Besiedlungsgeschichte. Eine faunistisch-biologische Studie. *Internationale Revue der gesamten Hydrobiologie und Hydrogeographie*, 9, 189-212, 241-288, 451-490.
- Kuhn, W., 1977. Berechnung der Temperatur und Verdunstung alpiner Seen auf klimatologisch-thermodynamischer Grundlage. Report Nr. 70, Swiss Meteorological Institute.
- Liston, G. E., and D. K. Hall, 1995. An energy balance model of lake ice evolution. *Journal of Glaciology*, 41(138), 373-382.

- Livingstone, D. M., and D. M. Imboden, 1989. Annual balance and equilibrium temperature of Lake Aegeri, Switzerland. *Aquatic Sciences*, 51(4), 351-369.
- Livingstone, D. M., 1997. Break-up dates of alpine lakes as proxy data for local and regional mean surface air temperatures. *Climatic change*, 37, 407-439.
- Livingstone, D. M., and A. F. Lotter, 1998. The relationship between air and water temperatures in lakes of the Swiss Plateau: A case study with paleolimnological implication. *Journal of paleolimnology*, 19(2), 181-198.
- Livingstone, D. M., A. F. Lotter, and I. R. Walker, 1999. The decrease in summer surface water temperature with altitude in Swiss Alpine lakes: A comparison with air temperature lapse rates. *Arctic and Alpine Research*, in press.
- Magnuson, J. J., B. J. Benson, and T. K. Kratz, 1990. Temporal coherence in the limnology of a suite of lakes in Wisconsin, U.S.A. *Freshwater Biology*, 23, 145-159.
- Maisch, M., 1992. Die Gletscher Graubündens. *Physische Geographie*, Universität Zürich.
- Marti, D. E., and D. M. Imboden, 1986. Thermische Energieflüsse an der Wasseroberfläche: Beispiel Sempachersee. *Aquatic Sciences*, 48(2), 196-229.
- Martinec, J., and A. Rango, 1986. Parameter values for snowmelt runoff modelling. *Journal of Hydrology*, 84, 197-219.
- Matthews, P. C., and S. I. Heaney, 1987. Solar heating and its influence on mixing in ice-covered lakes. *Freshwater Biology*, 18, 135-149.
- McMillan, W., 1973. Cooling from open water surfaces: Final report, Part 1: Lake Trawsfynydd cooling investigation. Scientific Services Department, CEGB Manchester.
- Oerlemans J., and W. H. Knap, 1998. A 1 year record of global radiation and albedo in the ablation zone of Morteratschgletscher, Switzerland. *Journal of Glaciology*, 44, 231-238.
- Olyphant, A., 1986. Longwave radiation in mountainous areas and its influence on the energy balance of alpine snowfields. *Water Resources Research*, 22(1), 62-66.
- Payne, R. E., 1972. Albedo of the sea surface. *Journal of the Atmospheric Sciences*, 29, 939-970.
- Plüss, C., 1997. The energy balance over an alpine snowcover. Point measurements and distribution. *Zürcher Geographische Schriften* Nr. 65, Zürich.
- Reitan, C. H., 1963. Surface dew point and water vapor aloft. *Journal of Applied Meteorology*, 2(6), 776-779.

- Roedel, W., 1994. Physik unserer Umwelt, Die Atmosphäre. 2. Auflage. Springer Verlag.
- Rogers, C. K., G. A. Lawrence, and P. F. Hamblin, 1996. Thermal impact of artificial circulation on an ice-covered midlatitude lake. *Canadian Journal of Civil Engineering*, 23(5), 1081-1091.
- Rohrer, M. B., and L. N. Braun, 1994. Long-term records of snow cover water equivalent in the Swiss Alps, 2. Simulation. *Nordic Hydrology*, 25(1/2), 65-78.
- Running, S. W., R. R. Nemani, and R. D. Hungerford, 1987. Extrapolation of synoptic meteorological data in mountainous terrain and its use for simulating forest evapotranspiration and photosynthesis. *Canadian Journal of Forest Research*, 17(5), 472-483.
- Saunders, I. R., and W. G. Bailey, 1997. Longwave radiation modeling in mountainous environments. *Physical Geography*, 18(1), 37-52.
- Sevruk, B., 1983. Correction of measured precipitation in the Alps using the water equivalent of new snow. *Nordic Hydrology*, 14(2), 49-58.
- Sevruk, B., 1997. Regional dependency of precipitation-altitude relationship in the Swiss alps. *Climatic Change*, 36, 355-369.
- Sevruk, B., 1998. The geography and topography effects on the areal pattern of precipitation in a small prealpine basin. *Water Science and Technology*, 37(11), 163-170.
- Skjelkvale, B. L., and R. F. Wright, 1998. Mountain lakes: Sensitivity to acid deposition and global climate change. *Ambio*, 27(4), 280-286.
- Sommaruga-Wögrath, S., K. A. Koinig, R. Schmidt, R. Sommaruga, R. Tessadri, and R. Psenner, 1997. Temperature effects on the acidity of remote alpine lakes. *Nature*, 387, 64-67.
- Stefan, H. G., J. J. Cardoni, F. R. Schiebe, and C. M. Cooper, 1983. Model of light penetration in a turbid lake. *Water Resources Research*, 19(1), 109-120.
- Stefan, H. G., M. Hondzo, X. Fang, J. G. Eaton, and J. H. McCormick, 1996. Simulated long term temperature and dissolved oxygen characteristics of lakes in the north central United States and associated fish habitat limits. *Limnology and Oceanography*, 41(5), 1124-1135.
- Stefan, H. G., and X. Fang, 1997. Simulated climate change effects on ice and snow covers on lakes in a temperate region. *Cold Regions Science and Technology*, 25, 137-152.

- Stüve, P., 1988. Die Schneeschmelze eines nordskandinavischen Einzugsgebietes ermittelt über räumlich-zeitliche Variation des Strahlungs- und Energiehaushalts. Institut für Physische Geographie der Freien Universität Berlin.
- Summa, V., 1998. Einfluss von suspendierten Partikeln auf den Stickstoffhaushalt von Mikroorganismen in einem Hochgebirgssee. Diploma Thesis, University of Zürich.
- Sweers, H. E., 1976. A nomogram to estimate the heat-exchange coefficient at the air-water interface as a function of wind speed and temperature; a critical survey of some literature. *Journal of Hydrology*, 30, 375-401.
- Swinbank, W. C., 1963. Longwave radiation from clear skies. *Quarterly Journal of the Royal Meteorological Society*, 89, 339-348.
- Theis, D., 1999. Einfluss von suspendierten Erosionspartikeln auf den Nährstoffhaushalt und die Mikrobiota in einem oligotrophen Hochgebirgssee. Diploma thesis, University of Zürich.
- Ullmann, S., 1998. Grundwasser in Moränenbastionen - Fallstudie und Modellierung. Diploma thesis University of Zürich, Institute of Geography.
- Vavrus, S. J., R. H. Wynne, and J. A. Foley, 1996. Measuring the sensitivity of southern Wisconsin lake ice to climate variations and lake depth using a numerical model. *Limnology and Oceanography*, 41(5), 822-831.
- Venäläinen, A., M. Heikinheimo, and T. Tourula, 1998. Latent heat flux from small sheltered lakes. *Boundary-Layer Meteorology*, 86(3), 355-377.
- Volker, A., 1951. Evaporation du Lac Ijssel. International Association of International Hydrology Science Assembly General, Bruxelles. Publication No. 34, 406-408.
- Wahrenberger, C., M. Rohrer, and H. Lang, 1997. Langjährige saisonale Wasserbilanzen des Landwassers und Dischmabaches. *Berichte und Skripten*, No. 60. Geographisches Institut, ETH Zürich.
- Warburton, J., 1990. An alpine proglacial fluvial sediment budget. *Geografiska Annaler*, 72A, 261-272.
- Wathne, B. M., S. T. Patrick, D. Montith, and H. Barth, 1995. AL:PE Project part 1. Acidification of mountain lakes: Paleolimnology and ecology. Ecosystems research report 9. European commission, EU 16129 EN.

Acknowledgements

Working as a mountain lake researcher in the middle of atmospheric scientists was not always easy. Nevertheless, I do not regret having been placed here 3 years ago. I would like to thank *Prof. A. Waldvogel* for providing me with the opportunity to work at the Institute for Atmospheric Sciences and for serving as my "Doktorvater", as well as for giving me the freedom to pursue the interesting aspects of mountain lake research.

I'd also like to thank *Dr. K. Hanselmann* for his support during difficult times in my thesis. His enthusiasm for research was contagious in a very positive sense. He also made sure that good research could be carried out in the rough mountain climate at the Jöri lakes and I am very grateful to have had the opportunity to work at such a beautiful place. Many others have envied me for that.

When it was difficult to focus on an interesting research subject, *David M. Livingstone* was there to inspire me with his knowledge about mountain lakes and limnology. He may not realize just how much his help led to the success of this thesis.

Without measurements, the research would have stalled. Our electronics expert *Donat Högl* was always there, when I needed his advice and he even hiked up to the lakes with me when weather and path conditions were absolutely unfavorable to install or take down instruments. Without the installations of our technician *Hanspeter Schmidhauser*, life at the lakes would have been much more difficult.

Many discussions with my fellow mountain lake researchers helped improve the understanding of the processes within the lakes and their catchment. I am most grateful to *Brigitte Hinder* for many of these discussions where she tried to improve my biological understanding of the lakes. Other researchers and helping hands at the Jöri site included *Isabel Baur*, *Vanessa Summa*, *Beatrice Steiner*, *Sandra Finnah*, *Jana Cejkova*, *Roman Schurter*, *Daniel Martinelli*, *Daniel Theis*, *Jakob Grünenfelder*, *Armand Vernez* and *Christian Hitz*.

I would also like to thank *Olivier Besson* of the University of Neuchâtel for providing me with the precise thermistor data from Lake III, without which the thesis would have gone in a completely different direction.

Many times when conditions to hike up to the lakes were unfavorable and none of the other researchers were available, friends and colleagues who were not involved in the project agreed to accompany me. I am very grateful for that service to *Andrea Weiss*, *Daniel Arn*, *Tadeusz Sas*, *Peter Isler*, *Markus Weidmann*, *The Dietrichs* and my family. My girlfriend *Natalie Milsom* had to endure several days and nights without me, when I was either at our research site or at a conference. She also accompanied me to

the Jöri lakes for a few days and I would like to thank her with all my heart for her moral support.

Christoph Marty (WRC), *Martin Zimmerli* (SLF) and *Johannes Böhm* (WSL) had the kindness of providing me with the data from the meteorological stations in the vicinity of the Jöri lakes.

Last, but not least, the whole staff and all the researchers at the *Institute for Atmospheric Sciences* helped to provide for a good working environment and were always there for interesting discussions.

This research was supported by the *EU Environment and Climate Program* (project MOLAR N0. ENV4-CT95-0007), financed by the *Ministry of Education and Science of Switzerland* (contract No. BBW 95.0518-2) and by the *Swiss National Science Foundation Grant* (CLEAR No. 5001-44614/1).

Curriculum Vitae

Matthias Gabathuler

born on January 23, 1971

Citizen of Wartau (SG)

EDUCATION

- 1977 - 1985 Primary and secondary school in Buchs (SG)
- 1985 - 1991 Kantonsschule Sargans (SG)
- 1988 - 1989 Exchange student at Lake Placid Highschool, NY, USA
- 1991 Matura Typus C
- 1991 - 1996 Studies in Environmental Sciences, ETH Zürich
- 1996 Diploma Thesis in Atmospheric Physics
Die Feinstruktur der Tropopause
- 1996 - 1999 Ph. D. student at the Institute of Atmospheric Sciences, ETH Zürich
under the guidance of Prof. A. Waldvogel and Dr. K. Hanselmann

WORK EXPERIENCE

- 1991 Programmer at MSI Dr. Wälti AG in Buchs (SG)
- 1995-1996 20 % employment at the Office for Environmental Protection of St.Gallen, air pollution department.
- 1996-1999 Assistant network administrator at the Institute of Atmospheric Sciences, ETH Zürich